



UNIVERSIDADE ESTADUAL DE CAMPINAS
Instituto de Física Gleb Wataghin

Mariano Esteves Chaves

BUSCA POR INTERAÇÕES DE CONTATO EM NEUTRINOS:
PRODUÇÃO E DETECÇÃO

SEARCH FOR CONTACT INTERACTIONS IN NEUTRINOS:
SOURCE AND DETECTION

Campinas
2022

Mariano Esteves Chaves

BUSCA POR INTERAÇÕES DE CONTATO EM NEUTRINOS: PRODUÇÃO E DETECÇÃO.

SEARCH FOR CONTACT INTERACTIONS IN NEUTRINOS: SOURCE AND DETECTION.

Tese apresentada ao Instituto de Física Gleb Wataghin da Universidade Estadual de Campinas como parte dos requisitos exigidos para a obtenção do título de Doutor em Ciências, na área de Física.

Thesis presented to the Institute of Physics Gleb Wataghin of the University of Campinas in partial fulfillment of the requirements for the degree of Doctor in Science in the area of Physics.

Orientador: Prof. Dr. Orlando Luís Goulart Peres

ESTE TRABALHO CORRESPONDE
À VERSÃO FINAL DA TESE DE-
FENDIDA PELO ALUNO MARIANO
ESTEVES CHAVES, E ORIENTADA
PELO PROF. DR. ORLANDO LUÍS
GOULART PERES

Campinas
2022

Ficha catalográfica
Universidade Estadual de Campinas
Biblioteca do Instituto de Física Gleb Wataghin
Lucimeire de Oliveira Silva da Rocha - CRB 8/9174

C398s Chaves, Mariano Esteves, 1993-
Search for contact interactions in neutrinos : source and detection /
Mariano Esteves Chaves. – Campinas, SP : [s.n.], 2022.

Orientador: Orlando Luis Goulart Peres.
Tese (doutorado) – Universidade Estadual de Campinas, Instituto de Física
Gleb Wataghin.

1. Neutrinos. 2. Partículas (Física nuclear). 3. Física além do modelo
padrão. 4. Teoria quântica de campos. I. Peres, Orlando Luis Goulart, 1969-. II.
Universidade Estadual de Campinas. Instituto de Física Gleb Wataghin. III.
Título.

Informações Complementares

Título em outro idioma: Busca por interações de contato em neutrinos : produção e detecção

Palavras-chave em inglês:

Neutrinos

Particles (Nuclear physics)

Physics beyond the standard model

Quantum field theory

Área de concentração: Física

Titulação: Doutor em Ciências

Banca examinadora:

Orlando Luis Goulart Peres [Orientador]

Carola Dobrigkeit Chinellato

Marcos Cesar de Oliveira

Célio Adrega de Moura Júnior

Ricardo Avelino Gomes

Data de defesa: 31-10-2022

Programa de Pós-Graduação: Física

Identificação e informações acadêmicas do(a) aluno(a)

- ORCID do autor: <https://orcid.org/0000-0001-7396-081X>

- Currículo Lattes do autor: <http://lattes.cnpq.br/7145030134888763>

MEMBROS DA COMISSÃO EXAMINADORA DA DISSERTAÇÃO DE DOUTORADO DO ALUNO MARIANO ESTEVES CHAVES - RA 211770 APRESENTADA E APROVADA AO INSTITUTO DE FÍSICA “GLEB WATAGHIN”, DA UNIVERSIDADE ESTADUAL DE CAMPINAS, EM 31/10/2022.

COMISSÃO JULGADORA:

- Prof. Dr. Orlando Luiz Goulart Peres – Presidente e orientadora (IFGW/UNICAMP)
- Profa. Dra. Carola Dobrigkeit Chinellato (IFGW/UNICAMP)
- Prof. Dr. Marcos Cesar de Oliveira (IFGW/UNICAMP)
- Dr. Célio Adrega de Moura Júnior (Universidade Federal do ABD, Centro de Ciências Naturais e Humanas)
- Dr. Ricardo Avelino Gomes (Universidade Federal de Goiás – Campus regional de Goiás)

OBS.: Ata da defesa com as respectivas assinaturas dos membros encontra-se no SIGA/Sistema de Fluxo de Dissertação/Tese e na Secretaria do Programa da Unidade.

CAMPINAS

2022

AO MEU PAI, VILMAR CHAVES.

Acknowledgements

Inicialmente, gostaria de agradecer a Deus, por me permitir viver toda a experiência que foi construir este trabalho. Agradeço, a todos que contribuíram para a construção desta tese, direta ou indiretamente. Agradeço ao professor Orlando, pela paciência e orientações, ao professor Pedro pelo auxílio durante as simulações de neutrinos solares e ao professor Thomas Schwetz pelo acolhimento numa terra tão distante como a Alemanha.

Também gostaria de agradecer a todos os doutorandos e pós-doutorandos que me ajudaram com dicas, com incentivos e discussões. Em especial, gostaria de enfatizar a Zahra, o Suprabh e o Yago que de alguma maneira influenciaram diretamente nos resultados deste trabalho.

Em especial agradeço minha família, por todo suporte dado durante o período em Campinas e na pandemia, seria impossível a conclusão deste trabalho sem eles.

Por fim mas não menos importante, agradeço a minha esposa Isabelle, pelo amor, carinho e pelos tão saborosos cafés da manhã.

This study was financed in part by the Coordenação de Aperfeiçoamento de Pessoal de Nível Superior - Brasil (CAPES) - Finance Code 001 and by "Ministry of Science, Technology and Innovation" and the "National Council for Scientific and Technological Development – CNPq".

Resumo

Neste trabalho, apresentamos uma análise fenomenológica de novas interações em experimentos com neutrinos. Dividimos este trabalho em dois resultados principais, o primeiro considerando novas interações de corrente carregada e o segundo para novas interações de corrente neutra.

Para novas interações carregadas, procuramos experimentos de oscilação de neutrinos no sabor do elétron. Neste trabalho utilizamos o formalismo da Teoria Quântica de Campos que não é comumente utilizado na fenomenologia dos neutrinos. Assim, experimentos com neutrinos de elétrons foram considerados, incluindo reatores e experimentos solares. Realizamos a análise estatística do ajuste de oscilação e dos parâmetros permitidos.

Para novas interações de corrente neutra usamos o experimento COHERENT e resultados de análise global de dados de oscilação. Nossos principais resultados foram focados na solução LMA-D, que foi excluída por 3σ neste trabalho. Também realizamos uma análise de sensibilidade para resultados experimentais futuros como em reatores e detecção de neutrinos na European Spallation Source.

Abstract

In this work, we present a phenomenological analysis of new interactions in neutrino experiments. We divide this work into two main results, the former considering new charged current interactions and the latter for new neutral current interactions.

For new charged current interactions we look to neutrino oscillation experiments in the electron flavor. In this work, we use the formalism of Quantum Field Theory which is not commonly used in neutrino phenomenology. Hence, electron neutrino disappearance experiments were considered, including reactors and solar experiments. We perform the statistical analysis of the oscillation fit and of the allowed parameters.

For new neutral current interactions we use the COHERENT experiment and the results of a global analysis of oscillation data. Our main results were focused on the LMA-D solution, which was (the LMA-D) excluded by 3σ in this work. We also perform a sensitivity analysis for future experimental results, as in reactors and neutrino detection in the European Spallation Source.

List of Figures

2.1	Feynman diagram for a neutrino oscillation process, from production to detection. Here, P means production, and D is detection. The time arrow is from the left to the right.	24
3.1	The four-vertex Feynman diagram for the anti-neutrino and neutrino detection. One can read the Feynman diagram from the left to the right. . .	42
3.2	Here we show the four-vertice Feynman diagrams for the neutrino and antineutrino production. In the left, there is the β^+ decay, in the center the β^- , and on the right side, the electron capture (E.C.). We assume a horizontal time-arrow from left to right for those diagrams.	47
3.3	Schematic view of the Daya Bay experiment.	53
3.4	The yellow circles represent the reactor's positions in the left schematic view of the RENO [1] experiments. On the right is the schematic view of the Double Chooz experiment [2].	54
3.5	We show our results for the confidence level curves at 3σ for Daya Bay (dashed red), DoubleChooz experiment (dotted blue), and RENO experiment (dashed-dotted green). Further, the confidence level curves for a joint analysis of all the three experiments at 1, 2, and 3σ in shades of red. . . .	55
3.6	Kamland reactors distribution on a map. Taken from http://www.insc.gov	56
3.7	Connection of parameter sensitivity to experimental set. Solid line represents strong sensitivity, the dashed line represents weak sensitivity. Colored lines mean that the parameter is active only if new physics is present. . . .	61
3.8	In this figure, we present the Monte Carlo simulated results of the $\Delta\chi^2$. We show the boxplot for each distribution. In green we present the limits when tensor interactions are present, in yellow for scalar interactions and in blue for standard neutrino oscillation.	62

3.9	In the first line, the panels are the 1D $\chi^2 - \chi_T^2$ functions where the minimum value we put the smallest among the minimum χ^2 of the three cases, in this case, was the tensor. In dashed green, we show the tensor interactions case, in plain yellow, the scalar and the standard neutrino oscillation in dash-dotted blue. In the panels below, we show a grid with six 2D panels for all combinations of parameters simulated. In green, we show the tensor, in yellow, the scalar, and in blue, the standard neutrino oscillation. The contours were set to 1, 2, and 3 σ	63
3.10	The same as in figure 3.9 but for $[\tilde{\epsilon}_X]_{e\mu}$	66
3.11	Events of Daya Bay experiment, in black we show the data points, in blue the standard oscillation and in red the tensor $e\mu$ interaction. In the left panel, we show the EH2/EH1 ratio and the EH3/EH1 ratios in the right panel. The small panel inside the left panel shows the total rate results compared with the standard model. Here, the x-axis is the neutrino energy $E = E_\nu$. We use the data as presented in [3]	66
3.12	The same as in fig 3.9 but for solar neutrinos and $[\tilde{\epsilon}_X]_{e\mu}$ interactions	67
3.13	The same as the first line of figure 3.9 but for the global analysis of the $[\tilde{\epsilon}_T]_{e\mu}$ parameter.	68
3.14	In this figure we show the $\Delta\chi^2$ as function of the CP-violation parameters, in the left (right) panel we show the $J_{e\tau}$ ($J_{e\mu}$) parameters of Eqs. (3.124) and (3.125).	69
3.15	Here we show a similar analysis to 3.8, but including JUNO for comparison. Here, GF means our global analyses (without JUNO), and JN is the only JUNO analysis.	71
4.1	Neutrino parameter space at the beginning of the 2000's. Figure from Ref. [4].	72
4.2	In this figure we show the contours at 95%, 99% and 99,73% form KamLAND (colored) and for Solar neutrinos (black lines), for Ref. [5].	73
4.3	Contours on 1σ , 2σ and 3σ (two dof) on the χ^2 of eq. (4.18) for the Chicago QF from ref. [6]. The SM weak charge for CsI is shown by the gray line $Q_{SM}^2 \approx 1352.5$	77
4.4	In the left: We show our prediction of Fig 6. of Ref. ?? using eq. (4.19) at 1σ , 2σ and 3σ (two dof) C.L.. In the right: using the eq. (4.19), we plot the 1σ , 2σ and 3σ (two dof) C.L. for the effective weak charge. The standard model weak charge in that case is $Q_{Ar}^2 \approx 114.64$	78

4.5	Here we show the 3σ regions for four different models depending on η . With the dashed orange curve, we show the COHERENT argon measurement. The blue straight curve shows the COHERENT CsI results, and the purple shaded region represents the combination of COHERENT CsI and Ar. From ref. [7].	79
4.6	For oscillation, we show the $\Delta\chi^2$ of the LMA-D solution minimized on $\epsilon_{\alpha\beta}^\eta$ and as a function of η (dotted black). For COHERENT, we show each target separated and in a joint analysis: oscillations+COHERENT(CsI) (blue), oscillations+COHERENT(Ar) (orange), and all data sets combined (purple). For the dashed curves, the off-diagonal $\epsilon_{\alpha\beta}^\eta$ are fixed at zero, and for the solid curves, we minimize over them. From ref. [7].	82
4.7	Our 90% C.L. curves for the eqs. (4.28) and (4.16) assuming different targets.	84
4.8	Expected sensitivity to exclude LMA-dark by a CE ν NS measurement at ESS using different target materials. For dashed curves the off-diagonal $\epsilon_{\alpha\beta}^\eta$ are fixed at zero, for solid curves we minimize with respect to them. From ref. [7].	84
4.9	Allowed regions in the plane of ϵ_{ee}^η and $\epsilon_{\mu\mu}^\eta$ at $\Delta\chi^2 = 11.83$ corresponding to 3σ for two dof, for different fixed values of η . The contour lines correspond to the regions from oscillation data, COHERENT(CsI), and COHERENT(Ar) separately. The purple filled region is obtained by combining all three data sets. The diagonal band corresponding to oscillation data does not pass through the SM point $\epsilon_{\mu\mu}^\eta = \epsilon_{ee}^\eta = 0$ because we have assumed the LMA-dark solution with $\theta_{12} > 45^\circ$. The light-red filled region shows the sensitivity of a future measurement at ESS using Si detector, assuming the SM. Off-diagonal $\epsilon_{\alpha\beta}^\eta$ are fixed at zero. From ref. [7].	85
4.10	$\Delta\chi^2$ between the LMA-dark and LMA-light best-fit points as function of the relative measurement error σ/Q_{SM}^2 for a CE ν NS experiment at a stopped pion source for different target materials, assuming that the best-fit point corresponds to no NSI. In scaling σ we keep the ratio σ_μ/σ constant, using the value given in tab. 4.1. The dashed-green curve shows the result for Ge for $\sigma_\mu \rightarrow \infty$. The stars indicate the assumptions for ESS sensitivities based on [8]. From ref. [7].	86

4.11	Same as fig. 4.9 but showing allowed regions at 3σ from a Ge target at a stopped pion source assuming a precision of $\sigma/Q_{\text{SM}}^2 = 0.028$, a factor 5 better than the ESS assumption from [8]. For the green-shaded region (green-solid contours) we assume $\sigma_\mu/\sigma = \infty$ (4.2). From ref. [7].	87
4.12	Limits on light mediators using the absence of a coherent neutrino nucleon scattering.	88
4.13	Global analysis with the limits on the LMA-D degeneracy.	89
4.14	Same as fig. 4.9 with sensitivity of the reactor experiments using Ge and Si overlaid assuming a 5% measurement of the weak charge Q_{SM} . From ref. [7].	90
4.15	Sensitivity to exclude the LMA-dark solution by a hypothetical $\text{CE}\nu\text{NS}$ measurement at a nuclear reactor using a Si (red curves) or a Ge (green curves) target. In both cases, we assume a 5% measurement of Q_{SM} . For dashed curves, off-diagonal $\epsilon_{\alpha\beta}^\eta$ are fixed to zero. For solid curves, we minimize concerning them. For $\eta \gtrsim -33^\circ$ the Si and Ge curves overlap. . .	91
4.16	Sensitivity to exclude the LMA-dark degeneracy by a hypothetical $\text{CE}\nu\text{NS}$ measurement at a nuclear reactor combined with ESS. The red-dashed curve corresponds to Si target at a reactor. For the solid curves we combine reactor(Si) with measurements at the ESS assuming Ar, Ge, Xe, and CsI targets, see sec. 4.3 for details.	92

List of Tables

3.1	Production and detection factors in Eq. (3.12) for reactors antineutrinos. Here E_e is the positron energy, m_e is the electron mass and $f(E_\nu)$ take into account the nuclear fuel and sub-products in the reactor model. For low-energy, the positron energy can be related to the antineutrino electron by the relation $E_e = E_\nu - \Delta_{if}$, where $\Delta_{if} = m_f - m_i$ is the mass difference between the final and initial nucleon.	52
3.2	The same as Table 3.1 but now for production and detection factors for solar neutrinos.	58
4.1	The number of protons Z , the neutron-to-proton ratio $Y = N/Z$, the corresponding blind spot η_{blind} , eq. (4.17), and the value of the SM weak charge, Q_{SM} , for different target materials. We use the average N corresponding to the natural isotope abundances, and for the molecules C_3F_8 and CsI , we take the average Z and N values. The last two columns show our assumptions about the measurement uncertainties obtainable at ESS. . . .	76

Contents

1	Introduction	16
2	The Neutrino Oscillation Theory	20
2.1	Quantum Mechanics	20
2.1.1	Basis vectors	20
2.1.2	Plane wave formalism	21
2.2	Quantum Field Theory	23
2.2.1	External Wave Packet Treatment	24
3	Non-standard neutrino interactions: production and detection (CC)	32
3.1	Effective Field Theory	33
3.1.1	Lee-Yang Effective Field Theory	34
3.2	New interactions and neutrino oscillations	35
3.2.1	The oscillation rate	37
3.2.2	Amplitude calculation	41
3.2.3	Solar neutrino oscillation	48
3.3	Case study: solar neutrinos and reactors	50
3.3.1	Statistics	50
3.3.2	Reactors	51
3.3.3	Solar neutrino experiments	58
3.4	Results and Conclusions	60
3.4.1	The $[\tilde{\epsilon}_X]_{e\tau}$	63
3.4.2	The $[\tilde{\epsilon}_X]_{e\mu}$	65
3.4.3	CP-violation	68
3.4.4	JUNO	70

4	Non-standard neutrino interactions: production and detection (NC)	72
4.1	CE ν NS	75
4.2	COHERENT	76
4.2.1	Global oscillation limits on non-standard neutrino interactions . . .	79
4.2.2	Results	81
4.3	ESS	82
4.3.1	Analysis	83
4.3.2	Results	83
4.4	Reactors	87
4.4.1	CONNIE Measurements	88
4.4.2	Sensitivity	89
5	Conclusions	93
	Bibliography	95

Chapter

1

Introduction

The development of Physics in the last century led to the Standard Model of Particle Physics [9], [10], [11] and [12]. The Standard Model is a theory of particles and their interactions in the Universe. The first building block begins with the discovery of tiny particles like the electron and the photon and goes to the Higgs boson discovery in the last decade [13].

At the beginning of the twentieth century, Max Planck and Einstein created the theory of quanta, which quantized light in packages of energy. His theory solves the ultraviolet divergence of the black body light spectrum. A few year later, Einstein used that idea to propose the photoelectric effect, and Compton proposed the Compton effect in which light could scatter with electrons like a particle. In the meantime, many contributions appeared involving the electron, the proton, and the neutron. The description of particles and their interactions were enough to describe the atom, that is, the matter we see.

At the beginning of the 1930s, in an attempt to explain the missing electron energy in the beta decay process, Pauli proposed the existence of a new particle, the neutrino. Later, Enrico Fermi described the interactions involving neutrinos in his theory of the beta decay. Fermi's theory was a four-point interaction between neutrinos, electrons, protons and neutrons. The neutrino should always appear in a beta decay process carrying away part of the energy of the particles. A conceptual problem at that time was that this particle was supposed to be massless and the intensity of the interaction to be low; hence, the process was very challenging to be detected. However, in 1956, the neutrino was detected in an underground reactor for the first time [14].

At that time, many other particles were already discovered, like the pion, the muon and antiparticles as the positron. In addition, many others were found with time, among them the second neutrino. The rising number of particles discovered led to the

creation of an organizing theory that explains all the particles and their interactions using symmetries between them. This theory was called the Standard Model.

The standard model was built on two essential symmetries, the $SU_C(3)$ and the $SU_I(2) \times U_Y(1)$. The former appears in the strong interaction Lagrangian, and the latter is the weak interaction Lagrangian. The strong interaction happens between color-charged particles, such as quarks and gluons. The quarks are building blocks of barions (as protons and neutrons) and mesons (as the pion and kaons). In turn, the gluons are massless particles that mediate this interaction.

The second symmetry is more critical for this thesis. It leads to the weak interaction between W and Z bosons, leptons (electron, muon, tau, and neutrinos) and quarks. The weak interaction can be classified as a neutral current or a charged current interaction, depending on whether the boson mediator is the charged W or the neutral Z boson. It is the generalization of the four-point theory of Fermi interactions.

The Standard Model (SM) formalism is the Quantum Field Theory, an approach based on fields instead of particles. The SM has a field Lagrangian, which contains all particles and interaction. The terms generated by the SM symmetries can be used to compute observable quantities as decay rates and cross-sections. The Quantum Field Theory (QFT) is a mathematical framework that mixes Quantum Mechanics and special relativity concepts, hence it mixes the description of small with high energy particles. In addition, the ordinary Quantum Mechanics can not be used to describe the photon because it has zero mass and travels at the velocity of light. Hence, QFT is a necessary theory for the correct description of the photon [15]. In this context, the quantization of the electromagnetic field was the first Quantum Field Theory and was developed in the first 30 years of the last century. The inception of Quantum Field Theory arose mixed with Quantum Mechanics, with Einstein's photoelectric effect theory and other contributions between 1910 and 1930. Later, many issues (ultraviolet and infrared divergence) appeared in the formalism that were solved by the renormalization concept.

The last building block to be discovery in the Standard Model was the Higgs boson. The Higgs boson appears in the SM after a process called symmetry breaking, used to generate renormalizable mass for all massive particles of the theory [11], [16] and [17]. The discovery of the Higgs boson was possible only in 2012 [18] and [13].

In the Standard Model, the neutrino is described as a massless particle. However, in 1998, the Super-Kamiokande collaboration confirmed the neutrino mass using atmospheric neutrino oscillations [19]. This is in contradiction with the Standard Model, in which no mechanism for neutrino mass is described. The neutrino oscillation was pro-

posed in 1958 by Bruno Pontecorvo [20] and has received the contributions of several authors up to now. The mathematical approach for neutrino oscillation begins with the θ puzzle and the proposal of flavor mixing by Gell-Man and Pais [21]. Later, Pais and Piccioni [22] suggested a coherent superposition of the mass eigenstates in the propagation. For neutrinos, the first hypothesis made by Pontecorvo was neutrino-antineutrino oscillation [20]. The flavor mixing was proposed in 1962 by Maki Nakagawa and Sakata [23], and in 1968 Pontecorvo, together with Gribov [24] proposed the neutrino flavor oscillations.

The Quantum Mechanics formalism of neutrino oscillation began to receive contributions around the 90s. One of the pioneer works in this context was that of Kayser [25], who showed that neutrino plane wave assumptions are in contradiction with some important physical concepts. Later on, Giunt and Kim showed that flavor states are ill-defined in Quantum Field Theory [26] and then proposed a Quantum Field Theory Wave Packet treatment of neutrino oscillations [27]. Discussions of the formalism of neutrino oscillations in Quantum Mechanics and Quantum Field Theory still exist today, and we can cite [28] as a recent review on this subject.

The neutrino oscillation formalism is based on the existence of three massive neutrinos. The massive neutrino field mix into flavor interaction fields through the Pontecorvo-Maki-Nakagawa-Sakata (PMNS) matrix. The PMNS matrix has four degrees of freedom, in the standard parametrization it can be fully described by θ_{12} , θ_{13} , θ_{23} and a complex phase δ_{CP} . In the final expression for neutrino oscillations in vacuum, two kinematic quantities also appear, $\Delta m_{3i}^2 = m_3^2 - m_i^2 (i = 1, 2)$ and $\Delta m_{21}^2 = m_2^2 - m_1^2$. Hence, neutrino oscillation brings the opportunity to achieve neutrino mass information from neutrino oscillations.

As a result, in the current scenario, we have a well-structured theory of neutrino oscillation whose parameters are measured with increasing precision each decade. However, only CP violation measurements and the ordering of neutrino masses remain, which should be measured in the next generation of neutrino experiments.

In this sense, the neutrino mass is a subject related to new physics since it is not present in the Standard Model. There are several extensions to the neutrino oscillation formula based on extensions of the Standard Model: new interactions in the production and detection, new interactions in the propagation, neutrino decay, neutrino decoherence, extra dimensions, and many others. Until the mystery of the origin of neutrino masses is not solved, the neutrino oscillation is seen with enthusiasm as an opportunity to detect new Physics.

One example, that is one of the subjects of this work, is the Large Mixing Angle

- Dark solution [29]. For several years, non-standard neutrino interactions were a subject of uncertainties for the neutrino oscillations when describing solar neutrino disappearance experiments. Solar experiments are used to measure with the most considerable precision the mixing angle θ_{12} . However, the possible presence of new interactions shadows the solution parameter space, leading to discussions that remain up today.

In this work, we investigate implications of new interactions in neutrino oscillations. In chapter 2, we introduce the neutrino oscillation formalism used in the following chapters. We show the derivation of neutrino oscillation in Quantum Mechanics and the Quantum Field Theory formalism that will be used in chapter 3. We divide the work into two main results: for charged current (CC) contact interactions in the production and detection, discussed in chapter 3. Then, in chapter 4, we present our findings related to new interactions in the neutrino propagation and the solution of the so-called Large Mixing Angle Dark Solution. In chapter 5, we review the main conclusions of this thesis.

Chapter 2

The Neutrino Oscillation Theory

This chapter will explore the theoretical and analytical development of the neutrino oscillation description. This was a subject of theoretical discussions over the last 30 years. We can highlight some reviews of the subject used to develop this chapter: [30], [27], [31], [28] and, more recently, [32]. At the first 20 years of neutrino oscillation proposal, the oscillation probability was based on a plane-wave quantum mechanics [24] and later, a wave packet treatment was also included [25]. At the beginning of the '90s, a quantum field theory emerged, discussing some issues when defining flavor eigenstates [26]. In terms of neutrino phenomenology, this is not well known, since all those approaches agree in the final expression of the oscillation probability.

In the 2000's, the Quantum Field Theory formalism of neutrino oscillation was already well established [31], [33]. In the 2010s, the connection between quantum mechanics and quantum field theory was developed and discussed [28], and also new physics was included in the formalism of quantum field theory [34].

In this chapter, we begin with the description of quantum mechanics plane wave and wave packets. We then introduce the quantum field theory formalism and its connection to quantum mechanics. We follow closely to [28].

2.1 Quantum Mechanics

2.1.1 Basis vectors

The basis of the quantum mechanics formalism of neutrino oscillation is to assume that there is a vector basis for the Hilbert space, \mathcal{H}_f , which is somehow related to the *flavor* observable. Every neutrino is created in one of the flavor base vectors that is characterized by the lepton generated together. However, for a neutrino to appear or

disappear, it must be assumed that flavor eigenstates are not free Hamiltonian eigenstates. The first postulate for the oscillation mechanism is:

Postulate 1: *There is a basis belonging to the Hilbert space, whose vectors are non-degenerate eigenstates of the operator \mathcal{O}_α , associated with the measure of weak interaction flavors: (e, μ, τ) .*

The second postulate is based on the fact that flavor eigenstates are not diagonal in a mass basis. We can formally express it as follows:

Postulate 2: *Let the free Hamiltonian of a neutrino α produced in a weak interaction be \hat{H} . Then we have:*

$$[\hat{H}, \mathcal{O}_\alpha] \neq 0. \quad (2.1)$$

With these two postulates, it is possible to build both the theory of plane waves and the theory of wave packets. To understand how the Hamiltonian eigenstates relate to the flavor base: let the set of all flavor eigenstates be $\{|\nu_\alpha\rangle\}$. Through these postulates, it is possible to show that there will always be a set of vectors, $\{|\nu_i\rangle\}$ with well-defined mass, which diagonalizes \hat{H} , such that:

$$|\nu_\alpha\rangle = \sum_i U_{\alpha i}^* |\nu_i\rangle, \quad (2.2)$$

where $U_{\alpha i}^*$ are components of the unit matrix \hat{U} that diagonalizes the Hamiltonian \hat{H} . It should be noted that postulate 1 is valid only if all eigenstates of the Hamiltonian are kinematically independent. For example, if at least one of the neutrinos is heavier enough to cause suppression of its production or detection, the mass state will no longer be part of the mixing. In this case, we need to redefine flavor states, which will be no longer orthogonal, and will depend on the energy regime in question. **This is one of the first indications of problems in the QM formalism.**

2.1.2 Plane wave formalism

The plane wave formalism is very important to obtain the standard form of the oscillation probability. To arrive at the plane wave treatment, suppose an initial state $|\nu_\alpha\rangle$. The probability of finding the state β at time t and distance x , can be found through the amplitude:

$$\mathcal{A}_{\alpha \rightarrow \beta}(t, \mathbf{r}) = \langle \nu_\beta | \exp(-i\hat{H}t + i\hat{\mathbf{P}} \cdot \mathbf{r}) | \nu_\alpha \rangle, \quad (2.3)$$

here $\hat{\mathbf{P}}$ is the momentum operator.

Hypothesis 1 (Plane wave): *The mass states $|\nu_i(0)\rangle$ are momentum eigenstates.*

Through hypothesis 1, when calculating the probability with the usual procedures of quantum mechanics, we find:

$$P(t, \mathbf{r}) = |\mathcal{A}_{\alpha \rightarrow \beta}(t, \mathbf{r})| = \sum_{ij} U_{\alpha i} U_{\beta i}^* U_{\alpha j}^* U_{\beta j} e^{i(\phi_i - \phi_j)} \quad (2.4)$$

with:

$$\phi_i = E_i t - \mathbf{p}_i \cdot \mathbf{r}. \quad (2.5)$$

Here, $E_i = \sqrt{p_i^2 + m_i^2}$ is the energy of the massive neutrino i , \mathbf{p}_i is its momentum and m_i is the neutrino mass. This is a widely used unrealistic hypothesis, the hypothesis of equal moments. It has the consequence of $e^{i\mathbf{p}\cdot\mathbf{r}}$ as a global phase, however it is not necessary to find the usual formula, as we will see. Since oscillation experiments are not time dependent, a number of works were carried out in an attempt to remove the time dependence of Equation (2.4).

In general, we can assume different detection times for massive neutrinos, that is $t = t_i + \delta t_i$.

Since the massive neutrino is *on-shell*, it has energy E_i related to momentum p_i and it is possible to expand the energy E_i around an average momentum, p , which is not very different between the different eigenstates of mass. Furthermore, we will also assume that there is an average mass, m , such that $\delta m_i^2 = m_i^2 - m^2$. With those assumptions, it is possible to rewrite the phase as:

$$\phi_i = \sqrt{p_i^2 + m_i^2} t_i - p_j x = \left(E + \frac{1}{2E} \delta m_i^2 + \frac{p}{E} \delta p_i \right) t_i - p x - \delta p x + E \delta t_i. \quad (2.6)$$

For simplicity, we assume in Eq. (2.6) the momentum in the x direction. At that momentum, using the relationship $p/E = v$ and applying the so-called *classical propagation condition* $vt - x = 0$ and the *prescription of equal times* $\delta t_i = t_i - t = 0$, we find:

$$\phi_i - \phi_j \approx \frac{\Delta m_{ij}^2 x}{2E}, \quad (2.7)$$

in which

$$\Delta m_{ij}^2 = m_i^2 - m_j^2. \quad (2.8)$$

It should be noted that the deduction made is valid only if the second order term $(\delta m_i^2)^2$ is negligible. For non-*quasi-degenerate* masses, the usual formula is no longer valid.

Conceptual problems arise when we look more carefully at the real situation:

- **Classical propagation condition:** As plane waves are delocalized in space-time, this condition cannot be justified without a more sophisticated treatment, for example, with wave packets[31].
- **Prescription of equal times:** Imposing equal times in the laboratory, also means imposing equal proper times. It is inconsistent with relativity given neutrinos have different velocities.
- It is a fact that if the moments have zero uncertainty, the uncertainty in the initial position of the neutrino would be infinite, so that it would be impossible to have a well-defined oscillation length.

Some of those issues can be overcome in the quantum field theory wave packet formalism. The subtleties of the wave packet formalism are covered in the quantum field theory, hence, we will discuss them in the context of QFT.

2.2 Quantum Field Theory

In particle physics, we are mainly interested in the measurement of cross-sections. Cross-section measurements reveal the conservation laws and symmetries of the theory. One of the primary assumptions in cross-section calculations is that the interactions are pointlike; that is, they occur in a definite small position in space and time. The cross-section calculations for particle physics come mainly from *Quantum Field Theory*.

However, when we talk about neutrino oscillations, the process occurs not in a short position in space and time but on scales that can vary from kilometers to hundreds of kilometers. Hence, if one wants to understand oscillations in the background of Quantum Field Theory, it is necessary to consider that pointlike production and detection are unique processes separated through space and time, see fig. 2.1.

A seminal article on neutrinos in QFT in 1993 showed that Fock space can not well-define flavor states [26]. Hence, it is only possible to perform kinematic calculations in Quantum Field Theory considering the neutrino mass states.

Moreover, in order to avoid problems of localization in space and time, all the particles involved in the process of production and detection should be considered as wave packets [27]. This is the **external wave packet treatment**, the core principle of the following calculations. In this approach, the neutrino is not seen as an initial or final state but as an intermediate virtual particle. The asymptotic states are, in reality, the particles

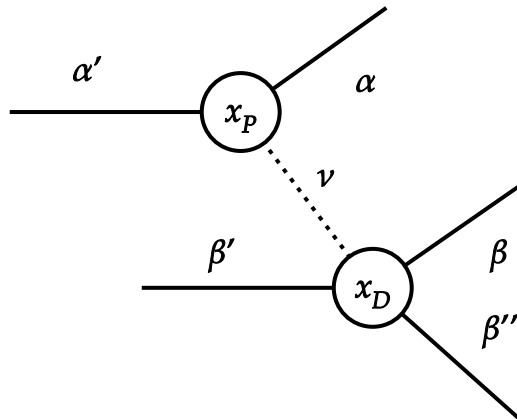


Figure 2.1: Feynman diagram for a neutrino oscillation process, from production to detection. Here, P means production, and D is detection. The time arrow is from the left to the right.

involved in neutrino detection; those can be mesons, protons, nucleons, and any particle involved in a process that can produce or detect neutrinos.

2.2.1 External Wave Packet Treatment

In the external wave packet treatment, the neutrino is produced near to a region \vec{x}_P at a time t_P and detected near to \vec{x}_D at time t_P . We label the production particles as α and its momentum at production p_α and at detection β and p_β , we will omit the spin information. The Feynman diagram for the oscillation process is shown in figure 2.1. The amplitude for this process is given by:

$$i\mathcal{A}(\alpha', \beta' \rightarrow \alpha, \beta, \beta'') = {}_{\text{out}}\langle \beta'', \beta, \alpha | \alpha', \beta' \rangle_{\text{in}}. \quad (2.9)$$

If the neutrino is produced and detected through charged current, we will always characterize the neutrino by the production of two leptons, α in the neutrino production and β in the neutrino detection. So, as we are interested in the flavored neutrino state, we will denote the amplitude by $\mathcal{A}(\alpha', \beta' \rightarrow \alpha, \beta, \beta'') = \mathcal{A}(\alpha', \beta' \rightarrow l_\alpha^-, l_\beta^-, \beta'')$.

We will consider that all the states are *disentangled*, thus allowing us to write the state as $|A, B\rangle = |A\rangle |B\rangle$ and work with each individual particle state. Hence, the wave packet states will be represented by a sum over the momentum states:

$$|\psi\rangle = \int [d\vec{p}] \times \psi(\vec{p}, \vec{P}, \vec{x}_0, t_0) \times |\vec{p}\rangle, \quad (2.10)$$

where t_0 is the initial time, \vec{x}_0 is the initial position, \vec{P} is the momentum where the wave

packet is distributed around and

$$[d\vec{p}] = \frac{d^3\vec{p}}{(2\pi)^3} \frac{1}{\sqrt{2E_p}}. \quad (2.11)$$

In addition, it is also possible to write the wave packet as a momentum distribution translated over space and time

$$\psi(\vec{p}, \vec{P}, \vec{x}_0, t_0) = \psi(\vec{p}, \vec{P}) e^{iEt_0 - i\vec{k}\cdot\vec{x}_0}. \quad (2.12)$$

Since all the initial and final states are defined, we can now calculate the amplitude. The states in eq. (2.9) are interaction eigenstates and for now, all the states we use are free asymptotic states. In this way, the amplitude will be given by [35]:

$$i\mathcal{A}(\alpha', \beta' \rightarrow \nu_\alpha, \nu_\beta, \beta'') = \langle \beta'' | \langle \beta | \langle \alpha | \left\{ T \left[\exp \left(-i \int d^4x \mathcal{L}_I \right) \right] - \mathbb{I} \right\} | \alpha' \rangle | \beta' \rangle, \quad (2.13)$$

where \mathcal{L}_I is the interaction Lagrangian, which includes all the possible interactions that involve the production (detection) particles. To calculate the amplitude, we use perturbation theory (Feynman rules in position space), obtaining

$$\begin{aligned} i\mathcal{A}(\alpha', \beta' \rightarrow \nu_\alpha, \nu_\beta, \beta'') &= \left[\prod_{\gamma=(\alpha^*, \alpha')} \int [d\vec{p}_\gamma] \psi_\gamma(\vec{p}_\gamma, \vec{P}_\gamma) \times e^{iE_\gamma t_P - i\vec{p}_\gamma \vec{x}_P} \right] \\ &\times \left[\prod_{\gamma'=(\beta^*, \beta', \beta''^*)} \int [d\vec{p}_{\gamma'}] \psi_{\gamma'}(\vec{p}_{\gamma'}, \vec{D}_{\gamma'}) \times e^{iE_{\gamma'} t_D - i\vec{p}_{\gamma'} \vec{x}_D} \right] \\ &\times \langle \vec{p}_{\beta''} | \langle \vec{p}_\beta | \langle \vec{p}_\alpha | \left\{ T \left[-\frac{1}{2} \int d^4x \mathcal{L}_P(x) \int d^4y \mathcal{L}_D(y) \right] \right\} | \vec{p}_{\alpha'} \rangle | \vec{p}_{\beta'} \rangle. \end{aligned} \quad (2.14)$$

Here $\mathcal{L}_P(x)$ and $\mathcal{L}_D(y)$ are the Lagrangian for the interactions at production and detection. The wave functions of stats that have (*) are conjugated. The third line of equation (2.14) is the plane wave amplitude, which we will denote it by \mathcal{A}^{pw} . In our approximation, we are in an effective low-energy approximation. So, the Lagrangian for production and detection do not depends on the bosons' W^\pm and Z^0 masses:

$$\mathcal{L}_P(x) = -\frac{G_F}{\sqrt{2}} \sum_i U_{\alpha i} j_{P_\mu}^\dagger \bar{l}_\alpha(x) (1 - \gamma^5) \gamma^\mu \nu_i(x) + \text{c.h.} \quad (2.15)$$

$$\mathcal{L}_D(y) = -\frac{G_F}{\sqrt{2}} \sum_i U_{\beta i}^* j_{D_\mu} \bar{\nu}_i(y) (1 - \gamma^5) \gamma^\mu l_\beta(y) + \text{c.h.} \quad (2.16)$$

For simplicity, let us take a concrete example. Let us assume, $\alpha \rightarrow l_\alpha^-, \beta \rightarrow l_\beta^-, \alpha' \rightarrow \pi^-, \beta' \rightarrow A_I$ and $\beta'' \rightarrow A_F$:

$$\begin{aligned}
|\pi^-\rangle &= \int [d\vec{p}] \psi_\pi(\vec{p}, \vec{P}) e^{-ipx_P} |\pi^-(\vec{p})\rangle, \\
|l_\alpha^-\rangle &= \int [d\vec{q}] \psi_\alpha(\vec{q}, \vec{Q}) e^{-iqx_P} |l_\alpha^-(\vec{q})\rangle, \\
|A_I\rangle &= \int [d\vec{k}] \psi_{A_I}(\vec{k}, \vec{K}) e^{-ikx_D} |A_I(\vec{k})\rangle, \\
|l_\beta^-\rangle &= \int [d\vec{q}'] \psi_\beta(\vec{q}', \vec{Q}') e^{-iq'x_D} |l_\beta^-(\vec{q}')\rangle, \\
|A_F\rangle &= \int [d\vec{k}'] \psi_{A_F}(\vec{k}', \vec{K}') e^{-ik'x_D} |A_F(\vec{k}')\rangle.
\end{aligned} \tag{2.17}$$

We will treat the initial and final states as asymptotic states. With this hypothesis, the amplitude of the process can be calculated through the matrix S :

$$i\mathcal{A}(\pi^-, A_I \rightarrow l_\alpha^-, l_\beta^-, A_F) = \langle A_F, l_\alpha^-, l_\beta^- | \left\{ T \left[\exp \left(-i \int d^4x \mathcal{L}_I \right) \right] - \mathbb{I} \right\} | \pi^-, A_I \rangle. \tag{2.18}$$

\mathcal{L}_I is the interaction Lagrangian and includes interactions that produce and detect neutrinos. Another fundamental hypothesis is to assume that there is no entanglement between the states of the production and detection particles. With this, we obtain:

$$|A_F, l_\alpha^-, l_\beta^-\rangle = |A_F\rangle |l_\beta^-\rangle |l_\alpha^-\rangle, \tag{2.19}$$

$$|\pi^-, A_I\rangle = |A_I\rangle |\pi^-\rangle. \tag{2.20}$$

Given these conditions, it is possible to calculate the amplitude (2.18) through perturbation theory. The calculation becomes simple if we calculate the tree diagram in position space, figure 2.1. Assuming the existence of only one mediating neutrino, we are taking to the amplitude below:

$$\begin{aligned}
\mathcal{A}_j &= \int \int \int \int [d\vec{k}] [d\vec{q}] [d\vec{k}'] [d\vec{q}'] \psi_{P_I}(\vec{q}, \vec{Q}) \psi_{D_I}(\vec{q}', \vec{Q}') \psi_{P_F}^*(\vec{k}, \vec{K}) \psi_{D_F}^*(\vec{k}', \vec{K}') M_P(q, k) M_D(q', k') \\
&\quad \times \int d^4x \int d^4x' \int \frac{d^4p}{(2\pi)^4} e^{-i(q-k)x_P} e^{-i(q'-k')x_D} e^{-ip(x'-x)} e^{-i(q-k)x} e^{-i(q'-k')x'} \frac{(\not{p} + m_j)}{p^2 - m_j^2 + i\epsilon},
\end{aligned} \tag{2.21}$$

where $\mathcal{A}(\pi^-, A_I \rightarrow l_\alpha^-, l_\beta^-, A_F) = \sum_j \mathcal{A}_{\nu_j}$. From the previous equation, we can see that there is a sum over all the momenta of all the particles involved, and also over the position of production and detection of the neutrino. Since x and x' are free variables, we can change variables:

$$\begin{aligned}
x + x_P &\rightarrow x \\
x' + x_D &\rightarrow x',
\end{aligned} \tag{2.22}$$

separating the detection and production terms in a more friendly form:

$$\mathcal{A}_j = \int \frac{d^4 p}{(2\pi)^4} \phi_P(\vec{K}, \vec{Q}, p) G_\nu(x_P, x_D, p) \phi_D(\vec{K}', \vec{Q}', p) \quad (2.23)$$

in which

$$\phi_P(\vec{K}, \vec{Q}, p) = \int \int [d\vec{k}][d\vec{q}] M_P(q, k) \psi_{P_I}(\vec{q}, \vec{Q}) \psi_{P_F}^*(\vec{k}, \vec{K}) \int dx e^{-ix(q-k-p)}, \quad (2.24)$$

$$\phi_D(\vec{K}', \vec{Q}', p) = \int \int [d\vec{k}'][d\vec{q}'] M_D(q', k') \psi_{D_I}(\vec{q}', \vec{Q}') \psi_{D_F}^*(\vec{k}', \vec{K}') \int dx' e^{-ix'(q'-k'+p)}, \quad (2.25)$$

and the propagator

$$G_\nu(x_P, x_D, p) = \frac{(\not{p} + m_\nu)}{p^2 - m_\nu^2 + i\epsilon} e^{ip(x_P - x_D)}. \quad (2.26)$$

The amplitude (2.23) has a simple interpretation. Here, ϕ_P is the amplitude for the production of a neutrino. It depends only on the interaction in the production and the wave packets of the particles involved. The same interpretation holds for the ϕ_D detection. The Green's function for the G_ν neutrino is responsible for connecting production with detection. Therefore, conditions for production and detection are contained in $\phi_{P,D}$ while conditions for propagation are contained in the G_ν .

If we have more than one neutrino involved in the process, we can sum over the amplitudes of all neutrinos, thus includes production, detection and propagation:

$$\mathcal{A}(\pi^-, A_I \rightarrow l_\alpha^-, l_\beta^-, A_F) = \sum_i \mathcal{A}_{\nu_i}. \quad (2.27)$$

For convenience, it is possible to rewrite the amplitudes as follows:

$$M_P^{(i,\alpha)}(p_i, p_f) \rightarrow U_{\alpha i} M_P^{(i)}(p_i, p_f), \quad (2.28)$$

$$M_D^{(i,\alpha)}(p_i, p_f) \rightarrow U_{\alpha i}^* M_D^{(i)}(p_i, p_f), \quad (2.29)$$

assuming that

$$M_P^{(i)}(p_i, p_f) \approx M_P(p_i, p_f), \quad (2.30)$$

$$M_D^{(i)}(p_i, p_f) \approx M_D(p_i, p_f). \quad (2.31)$$

We mean that the production and detection amplitudes are not sensitive to the neutrino mass, $m_i \ll M$, where M is the mass of the particles involved in the process.

Hence, for the whole process, if a lepton α appears at the production, and a lepton β at the detection, we can sum over all the neutrinos, obtaining:

$$\mathcal{A}(\pi^-, A_I \rightarrow l_\alpha^-, l_\beta^-, A_F) = \sum_i U_{\alpha i}^* U_{\beta i} \int \frac{d^4 p}{(2\pi)^4} \phi_P(\vec{K}, \vec{Q}, p) G_i(x_P, x_D, p) \phi_D(\vec{K}', \vec{Q}', p). \quad (2.32)$$

Continuing with the calculation of this amplitude, we can separate the momentum integral from the energy integral:

$$\mathcal{A}(\pi^-, A_I \rightarrow l_\alpha^-, l_\beta^-, A_F) = \sum_i U_{\alpha i}^* U_{\beta i} \int dE_i \int \frac{d^3 p_i}{(2\pi)^4} \phi_P(\vec{K}, \vec{Q}, p_i) G_i(x_P, x_D, p_i) \phi_D(\vec{K}', \vec{Q}', p_i). \quad (2.33)$$

The integral at the momentum can be performed using Grimus-Stockinger's theorem [36]:

For large L , positive A and a smooth function $\psi(\vec{p})$,

$$\int d^3 p \frac{\phi(\vec{p}) e^{i\vec{p}\cdot\vec{L}}}{A - (\vec{p})^2 + i\epsilon} = -\frac{2\pi^2}{L} \phi\left(\sqrt{A} \frac{\vec{L}}{L}\right) e^{i\sqrt{A}L} + \mathcal{O}(L^{-3/2}). \quad (2.34)$$

Matching $A = E_i^2 - m_i^2 = p_i^2$, the amplitude will be:

$$\mathcal{A}(\pi^-, A_I \rightarrow l_\alpha^-, l_\beta^-, A_F) = -\sum_i U_{\alpha i}^* U_{\beta i} \int dE_i e^{iE_i T} \frac{1}{8\pi^2 L} \phi_P(\vec{K}, \vec{Q}, p_i \hat{L}) \phi_D(\vec{K}', \vec{Q}', p_i \hat{L}) e^{ip_i L}, \quad (2.35)$$

where L is $|\vec{x}_P - \vec{x}_D|$ and \hat{L} is the normalized direction of $(\vec{x}_P - \vec{x}_D)$. From now on, let us abbreviate $\mathcal{A}(\pi^-, A_I \rightarrow l_\alpha^-, l_\beta^-, A_F) \rightarrow \mathcal{A}_{\alpha\beta}(L, T)$. With the simplification of the amplitudes, it becomes simpler to calculate the probability

$$P_{\alpha\beta}^{\text{osc}}(L, T) = |\mathcal{A}(L, T)|^2 = \frac{1}{(8\pi^2 L)^2} \sum_{ij} U_{\alpha i}^* U_{\beta i} U_{\alpha j} U_{\beta j}^* \int dE_i \int dE_j (\text{some factors}) e^{i(E_i - E_j)T}. \quad (2.36)$$

It should be noted that the quantity $P_{\alpha\beta}^{\text{osc}}(L, T)$ gives us the probability of producing a lepton l_α and detecting of a lepton l_β separated for a distance L and a time T . However, in what follows, we will be interested in averaging the probability over time, so:

$$\overline{P}_{\alpha\beta}^{\text{osc}}(L) = \frac{1}{T} \int dT P_{\alpha\beta}^{\text{osc}}(L, T) = \frac{1}{(8\pi^2)4\pi L^2} \sum_{ij} U_{\alpha i}^* U_{\beta i} U_{\alpha j} U_{\beta j}^* \int dE_i \phi_P^i \phi_P^{*j} \phi_D^i \phi_D^{*j} e^{i(p_i - p_j)L}, \quad (2.37)$$

where we use the delta function:

$$\int dT e^{i(E_i - E_j)T} = 2\pi\delta(E_i - E_j). \quad (2.38)$$

Defining the Probabilities

In an oscillation experiment, one of the main quantities observed is the total detection rate. In a given experiment, it is defined by:

$$\frac{N_\beta}{N_\alpha} = \Gamma_{\alpha\beta}^{\text{tot}} = \int \frac{d\Gamma_{\alpha\beta}^{\text{tot}}}{dE} dE. \quad (2.39)$$

The detection rate is the ratio of the number of α leptons produced to the number of β leptons detected. We multiply the energy production rate by the flow suppression factor $1/4\pi L^2$ and the detection cross-section when calculating the total detection rate. For the case of neutrino experiments, there is a quantity called the probability of oscillation that depends on L and E , so we should write:

$$\frac{d\Gamma_{\alpha\beta}^{\text{tot}}}{dE} = \frac{1}{4\pi L^2} \frac{d\Gamma_\alpha^{\text{prod}}}{dE} P(\nu_\alpha \rightarrow \nu_\beta)(L, E) \sigma_\beta(E). \quad (2.40)$$

Following the equation (2.40), the quantity called probability of oscillation, can be found through:

$$P(\nu_\alpha \rightarrow \nu_\beta)(L, E) = \frac{4\pi L^2 \frac{d\Gamma_{\alpha\beta}^{\text{tot}}}{dE}}{\frac{d\Gamma_\alpha^{\text{prod}}}{dE} \sigma_\beta(E)}, \quad (2.41)$$

which can be interpreted as the probability that a neutrino produced with flavor α will be detected with flavor β .

From now on, we will calculate the quantities shown on the right side of the equation (2.41). Starting with the total rate of the process, we will use the result of [37], where the total rate is calculated and given by

$$\Gamma_{\alpha\beta}^{\text{tot}}(L) = N_P N_D \frac{\overline{P}_{\alpha\beta}^{\text{osc}}}{T_0^2}. \quad (2.42)$$

Here, T_0 is a large time when compared to the usual time scales for production and detection, N_P is the number of neutrinos produced, N_D is the number of neutrinos detected, and $\overline{P}_{\alpha\beta}^{\text{osc}}$ is given by eq. (2.37):

$$\overline{P}_{\alpha\beta}^{\text{osc}}(L) = \sum_{ij} \frac{1}{(8\pi^2)4\pi L^2} \sum_{ij} U_{\alpha i}^* U_{\beta i} U_{\alpha j} U_{\beta j}^* \int dE_i \phi_P^i \phi_P^{*j} \phi_D^i \phi_D^{*j} e^{i(p_i - p_j)L}. \quad (2.43)$$

We are interested in the rate per energy. Taking the derivative of eq. (2.42) with respect to the energy, we can use:

$$\overline{P}_{\alpha\beta}^{\text{osc}}(L) = \int dE \frac{\overline{P}_{\alpha\beta}^{\text{osc}}(L)}{dE}, \quad (2.44)$$

to find

$$\frac{d\Gamma_{\alpha\beta}^{\text{tot}}(L)}{dE} = \frac{N_P N_D}{(8\pi^2)4\pi L^2 T_0^2} \sum_{ij} U_{\alpha i}^* U_{\beta i} U_{\alpha j} U_{\beta j}^* \phi_P^i \phi_P^{*j} \phi_D^i \phi_D^{*j} e^{i(p_i - p_j)L}. \quad (2.45)$$

Now, we only have to calculate the production rate and detection cross section to find the oscillation probability through the equation (2.41). The probability that an α lepton will be produced is:

$$P_{\alpha}^{\text{prod}} = \langle \pi^- | \hat{S} | \nu_{\alpha}, l_{\alpha} \rangle = \sum_i |U_{\alpha i}|^2 \int d^3 p_i \left| \phi_P(\vec{K}, \vec{Q}, p_i) \right|^2 = \sum_i \frac{|U_{\alpha i}|^2}{2\pi^2} \int \left| \phi_P(\vec{K}, \vec{Q}, p_i) \right|^2 E_i dE. \quad (2.46)$$

The production rate will be the time ratio multiplied by the number of producing particles:

$$\Gamma_{\alpha}^{\text{prod}} = N_0 \frac{P_{\alpha}^{\text{prod}}}{T_0} \Rightarrow \frac{d\Gamma_{\alpha}^{\text{prod}}}{dE} = \frac{N_0}{T_0} \sum_i \frac{|U_{\alpha i}|^2}{2\pi^2} \left| \phi_P(E, p_i) \right|^2 E_i. \quad (2.47)$$

For detection, we must assume that the neutrino has a well-defined energy and momentum, so that detection probability will be:

$$P_{\beta}^{\text{det}}(E) = \sum_i |U_{\beta i}|^2 \left| \phi_D(E, p_i) \right|^2 \frac{1}{V}. \quad (2.48)$$

Here the factor $1/V$ appeared when we suppose that the neutrino is produced with a well-defined momentum: it is the normalization of the plane wave. Analogously to the production case, we need to find the detection rate $\Gamma_{\beta}^{\text{det}}$ that relates to the cross section through:

$$\sigma_{\beta}(E) = \frac{\Gamma_{\beta}^{\text{det}}}{n_k v_k} = \Gamma_{\beta}^{\text{det}} V \frac{E}{p_k}. \quad (2.49)$$

Here n_k is the number of particles per volume (in our normalization it is $1/V$) and $v_k = \frac{E}{p_k}$. So the cross section will be:

$$\sigma_{\beta}(E) = \frac{N_D}{T_0} \sum_i |U_{\beta i}|^2 \left| \phi_D(E, p_i) \right|^2 \frac{E}{p_k}. \quad (2.50)$$

Substituting the equations (2.45), (2.47) and (2.50) into (2.41), we find the probability of oscillation:

$$P(\nu_{\alpha} \rightarrow \nu_{\beta})(L, E) = \frac{\sum_{ij} U_{\alpha i}^* U_{\beta i} U_{\alpha j} U_{\beta j}^* \phi_P(E, p_i \hat{l}) \phi_P^*(E, p_j \hat{l}) \phi_D(E, p_i \hat{l}) \phi_D^*(E, p_j \hat{l}) e^{i(p_i - p_j)L}}{\sum_i |U_{\alpha i}|^2 \left| \phi_P(E, p_i \hat{l}) \right|^2 p_i \sum_j |U_{\beta j}|^2 \left| \phi_D(E, p_j \hat{l}) \right|^2 p_j^{-1}}. \quad (2.51)$$

At the current stage, the oscillation probability differs a little from the usual formula, which is

$$P(\nu_\alpha \rightarrow \nu_\beta)(L, E) = \sum_{ij} U_{\alpha i}^* U_{\beta i} U_{\alpha j} U_{\beta j}^* \exp\left(-i \frac{\Delta m_{ij}^2 L}{2p}\right), \quad (2.52)$$

where $\Delta m_{ij}^2 = m_i^2 - m_j^2$ is the squared mass difference between the neutrinos and p the momentum of the neutrinos. On the other hand, we can recover the standard case if we assume two conditions:

- The wave packets are such that:

$$|p_i - p_j| \ll \sigma_{pP}, \sigma_{pD}, \quad (2.53)$$

where σ_{pP} and σ_{pD} are the uncertainties in the momentum distributions at the production and detection respectively. With this assumption, the peak of the functions ϕ_D, ϕ_P can be approximated by $p_i \rightarrow p$.

- The neutrino masses are *quasi-degenerate*, that is:

$$|p_i - p_j| \ll p_i, p_j. \quad (2.54)$$

With this hypothesis, we can replace the momenta p_i in the numerator and denominator by p and still perform the approximation:

$$p_i - p_j \approx \frac{m_j^2}{2p}. \quad (2.55)$$

Applying the conditions (2.53) and (2.54) in equation (2.51), we recover the standard case presented in eq. (2.52).

Chapter	3
---------	---

Non-standard neutrino interactions: production and detection (CC)

If Physics Beyond the Standard Model exists, non-standard interactions can be present in the neutrino production and detection. When present in the production and detection, interactions are assumed to be "charged current" types. That is, the interaction mediator has a non-zero charge. The study of new interactions in high-energy physics can mainly follow two directions:

- Model building: here, the theory is built on symmetries step by step. It is the most consistent way to build a theory (the Standard Model is built in that way). However, it is challenging and complex to construct without generating conflicts with observation;
- Effective Field Theories (EFT's): we integrate out all high-energy gauge bosons, and relics of the high-energy theory appears at low energy.

In this chapter, we study the consequences of non-standard interactions in the production and detection. We use solar and reactor neutrino experiments. First, we discuss the scenario of a general structure of new interactions (scalar, tensor, pseudo-scalar, left-handed, and right-handed). In this work, we will focus only on scalar and tensor interactions in the final analysis. All the interactions considered here are charged-current types, and present on beta and inverse-beta decays. We give more details in the following sections.

In section 3.1, we give a brief introduction to the Lagrangian of new interactions from an effective field theory. In section 3.2, we give a theoretical overview including amplitude calculations oscillations in the presence of new interactions, formulas, and discussions about the oscillation regime. In section 3.3, we give details about the analysis

and statistical quantities used to test the model. Finally, in section 3.4, we present the results and conclusions.

3.1 Effective Field Theory

As we already discussed, when studying new interactions in particle physics, one can follow through the model building approach. That is, construct the model under symmetries of nature. However, despite a general and complete scenario, due to the increase of the number of parameters to describe the full theory, this procedure is complex and can be very challenging.

The Effective Field Theory is an alternative method if the energy scale of the new interactions is above the experimental data. It is not necessary to look at the details of the theory (it is above the energy scale of interest). All possible Gauge bosons were "integrated out." The EFT is the approach we choose to follow in this work.

In more detail, an Effective Field Theory (EFT) arises when the experimental energy scale, Λ , is beneath the mass of the particles of the theory. For example, in the Fermi theory of weak interactions, the effective Lagrangian is a four-vertex interaction, the Fermi coupling constant hides all the electro-weak gauge bosons and $SU(2) \times U(1)$ couplings:

$$G_F = \frac{\sqrt{2}}{8} \frac{g^2}{M_W^2}. \quad (3.1)$$

As a further example, the Standard Model can be an Effective Field Theory for energies related to the LHC scale, 1 TeV. In this situation, if it is possible to consider the existence of new physics beyond the LHC scale, we can define the Standard Model Effective Field Theory (SMEFT) [38, 39]. The SMEFT includes the Standard Model Lagrangian and Effective Interactions coming from other energy scales:

$$\mathcal{L} = \mathcal{L}_{SM} + \sum_{j \geq 5} \frac{1}{\Lambda^{j-4}} \sum_i \frac{C_i^{(j)}}{\sqrt{2}G_F} \mathcal{O}_i^{(j)} \quad (3.2)$$

where $C_i^{(j)}$ gives the strength of the interaction, they are called dimensionless Wilson Coefficients, and $\mathcal{O}_i^{(j)}$ are dimension-j operators for different Standard Model particles. The index i runs over a set of Standard Model Particles and Lorentz Invariant interactions: left-handed, right-handed, tensor, scalar, and pseudo-scalar. The SMEFT is very useful when searching for the effects of new interactions at low energy.

For our case of study, we can integrate out the particles above the electroweak interaction scale¹, $\Lambda \sim 100$ GeV. At this point, the structure of the non-standard interac-

¹ Z, W^\pm , quark top, Higgs.

tions is the same as in the SMEFT. On the other hand, the Standard Model Lagrangian in the weak sector reduces to four-vertice interactions. An EFT on this scale is called Weak Effective Field Theory (WEFT). Our purpose is to reach **reactor and solar energies**, so that we can go further down in the energy scales, that is, below the proton mass scale $\Lambda \sim 1$ GeV.

In some specific cases², there is a match between the WEFT and the SMEFT. For such cases, if we constrain the non-standard interaction parameters, we will be constraining the Wilson Coefficients [39].

3.1.1 Lee-Yang Effective Field Theory

We focus our interest here on neutrino production at reactors and in the sun. In this case, two points should be distinguished:

- We are in the ~ 10 MeV energy scales, where protons and neutrons are more important than quarks;
- Our interest is the electroweak sector, that is, interactions between quarks and leptons;
- We will only consider dimension-6 operators. Due to the small neutrino mass, we neglect dimension-5 operators. Dimensions higher than six are suppressed by Λ^{n-6} cut-off.

Concerning the first point, we use the Lee-Yang Effective Field Theory (LYEFT). The LYEFT is a non-relativistic effective interaction theory between protons and neutrons in the electroweak sector. The LYEFT is appropriated at the energies smaller than the proton mass, 1 GeV.

In this thesis, we study reactor and solar neutrinos for which the energies are around 10 MeV. The Standard Model interaction Lagrangian for this theory is [40]:

$$\mathcal{L}_{LY} = -\frac{V_{ud}}{\sqrt{2}G_F} \sum_{\alpha=(e,\mu,\tau)} [\bar{p}\gamma^\mu(g_V - \gamma_5 g_A)n] [\bar{l}_\alpha\gamma_\mu P_L\nu_\alpha] + \text{h.c.} \quad (3.3)$$

Here, V_{ud} is the $u-d$ Cabibbo–Kobayashi–Maskawa (CKM) quark matrix component, g_V and g_A are experimental values related to the Fermi (vector) and Gamow-Teller (axial) transitions. The second and third points constrain us to including dimension-6 interactions

²e.g., no particles between both energy scales.

between quarks and leptons. In the non-relativistic energy scale, the non-standard new interactions (NSI) follow the Lagrangian

$$\begin{aligned} \mathcal{L}_{\text{NSI}} = & -\frac{V_{ud}}{\sqrt{2}G_F} \sum_{\alpha,\beta} \{ g_V[\epsilon_L + \epsilon_R]_{\alpha\beta} (\bar{p}\gamma^\mu n)(\bar{l}_\alpha\gamma_\mu P_L\nu_\alpha) - g_A[\epsilon_L - \epsilon_R]_{\alpha\beta} (\bar{p}\gamma^\mu\gamma_5 n)(\bar{l}_\alpha\gamma^\mu P_L\nu_\alpha) \\ & + g_S[\epsilon_S]_{\alpha\beta} (\bar{p}n)(\bar{l}_\alpha P_L\nu_\alpha) - [g_T]_{\alpha\beta} (\bar{p}\sigma^{\mu\nu}n)(\bar{l}_\alpha\sigma_{\mu\nu}P_L\nu_\beta) + \text{h.c.} \}, \end{aligned} \quad (3.4)$$

where, $\sigma^{\mu\nu} = \{\gamma^\mu, \gamma^\nu\}$ and γ_μ are the Dirac matrices. The $[\epsilon_X]_{\alpha\beta}$ are the couplings related to the Wilson coefficients that are always proportional to the square of the Higgs Vacuum Expectation Value (VEV), v , and to the inverse of the new physics energy scale, Λ , i.e., $[\epsilon_X]_{\alpha\beta} \propto \frac{v^2}{\Lambda^2}$. From the models of nuclear quark distributions and experimental measurements [41], we know that: $g_A = 1.2728 \pm 0.0017$, $g_S = 1.02 \pm 0.11$, $g_P = 349 \pm 9$ and $g_T = 0.987 \pm 0.055$. Here, the g_A, g_V, g_T and g_S were extracted from Refs. [42, 43, 44]. In this work, we are mainly interested in beta, and inverse beta decays at reactors and in the sun. In this case, ϵ_P can be neglected at low energies [45]. The effects of $[\epsilon_{[L,R]}]_{ee}$ are not considered here since we suppose experiments cannot distinguish them in the measurements of V_{ud} and g_A at the Lagrangian level:

$$V_{ud}[\mathbb{1} + \epsilon_L + \epsilon_R]_{ee}, \quad g_A \frac{[\mathbb{1} + \epsilon_L - \epsilon_R]_{ee}}{[\mathbb{1} + \epsilon_L + \epsilon_R]_{ee}}. \quad (3.5)$$

We also neglect non-diagonal ϵ_R , as it goes with $\mathcal{O}(\Lambda^{-4})$, which is above the m_W scale.

3.2 New interactions and neutrino oscillations

The neutrino production comes together with a lepton with a given flavor. For example, the beta decay process in reactors produces an antineutrino, converts a neutron into a proton, and releases an electron. Because of the electron, the antineutrino produced is called electron antineutrino. However, today we know this process is more complex than that, and the simple phrase "electron neutrino" requires clarification. The whole process of neutrino oscillation and neutrino flavor state were discussed in details in Chapter 2.

In this section, we discuss the process of neutrino production and detection in the presence of oscillations. This discussion is already present in the literature following Refs. [41, 34], which we will follow closely.

The calculation for producing a neutrino with mass i begins with the Lagrangian given in Eqs. (3.4) and (3.3). For each four-point term in those equations, we

can write an amplitude that later should be summed coherently:

$$\mathcal{M}_{\alpha k}^P = U_{\alpha i}^* \mathcal{M}_{\text{SM}}^P + \sum_{X=L,R,S,T} [\epsilon_X U]_{\alpha i}^* \mathcal{M}_X^P. \quad (3.6)$$

Here the amplitude comes together with the flavor of the associated lepton α , X is the type of interaction, and we have already seen the PMNS matrix. We can do the same for the detection process, where instead of the letter P (production), we will use the letter D (for detection). In section 3.2.2 we give more details about the calculation of the amplitudes for reactors and the sun.

In the Quantum Field Theory approach to the neutrino oscillation, the total rate is process-dependent (2.43), that is, it is dependent on the amplitudes for production and detection. Consequently, it can also depend on the interaction Lagrangian and the rates with Beyond The Standard Model (BSM) physics for a neutrino produced in a ν_α state detected as a ν_β state. This was given by Eq. (2.45) (neglecting wave packet contributions) and calculated for the first time on [45]:

$$R_{\alpha\beta} \propto \sum_{k,l} e^{-iL\phi_{kl}} \int d\Pi_P d\Pi_D \mathcal{M}_{\alpha k}^P \overline{\mathcal{M}}_{\alpha l}^P \mathcal{M}_{\beta k}^D \overline{\mathcal{M}}_{\beta l}^D. \quad (3.7)$$

Here,

$$\phi_{kl} \equiv \Delta m_{kl}^2 / 2E_\nu, \quad (3.8)$$

where $\Delta m_{kl}^2 \equiv m_k^2 - m_l^2$ is the squared mass difference between the mass eigenstates k and l , and E_ν is the neutrino energy. The $\Pi_D(\Pi_P)$ sums over the detection (production) phase space. In Eq. (3.7) the BSM fluxes and cross-sections are included through the interaction amplitudes. In the Standard Model case, we factor the fluxes and cross-section, making the oscillation probability process-independent. For the BSM case, we will also factorize the Standard Model fluxes and cross-sections:

$$R_{\alpha\beta}^{\text{SM}} \propto \sum_{k,l} \int d\Pi_P d\Pi_D (\mathcal{M}_{\alpha k}^P)^{\text{SM}} (\overline{\mathcal{M}}_{\alpha l}^P)^{\text{SM}} (\mathcal{M}_{\beta k}^D)^{\text{SM}} (\overline{\mathcal{M}}_{\beta l}^D)^{\text{SM}} \delta_{\alpha\beta} = \phi_\alpha^{\text{SM}} \sigma_\beta^{\text{SM}} \delta_{\alpha\beta} \quad (3.9)$$

where $(\mathcal{M}_{\alpha k}^{P,D})^{\text{SM}}$ are the amplitudes for production of a ν_α neutrino and detection of a ν_β neutrino in the Standard Model, ϕ_α^{SM} is the ν_α neutrino flux, and σ_β^{SM} is the detection cross-section for ν_β neutrino. Notice that there is no dependence on the distance between the source and the neutrino detection. Applying Eq. (3.9) on Eq. (3.7), we will have:

$$\frac{R_{\alpha\beta}}{\phi_\alpha^{\text{SM}} \sigma_\beta^{\text{SM}}} = \sum_{k,l} e^{-i\phi_{kl}L} [V_\alpha^{kl}(p_X)] \times [V_\beta^{kl}(d_X^*)]^*, \quad (3.10)$$

where

$$V_\alpha^{kl}(p_X) = U_{\alpha k}^* U_{\alpha l} + p_{XL}(\epsilon_X U)_{\alpha k}^* U_{\alpha l} + p_{XL}^* U_{\alpha k}^*(\epsilon_X U)_{\alpha l} + p_{XX}(\epsilon_X U)_{\alpha k}^*(\epsilon_X U)_{\alpha l}. \quad (3.11)$$

The $p_{XY}(d_{XY})$ is the ratio in the production (detection) between the squared amplitude terms $\mathcal{M}_{\alpha k}^X$ and $\mathcal{M}_{\alpha k}^Y$ divided by the Standard Model squared amplitude (the definitions of p 's and d 's include the integration over the phase space):

$$p_{XY} \equiv \frac{\int d\Pi_P A_X^P \bar{A}_Y^P}{\int d\Pi_P |A_{\text{SM}}^P|^2}, \quad d_{XY} \equiv \frac{\int d\Pi_D A_X^D \bar{A}_Y^D}{\int d\Pi_D |A_{\text{SM}}^D|^2}. \quad (3.12)$$

In the expression for antineutrinos, one should replace in Eq. (3.10):

$$U \rightarrow U^* \quad \text{and} \quad [\epsilon_X]_{\alpha\beta} \rightarrow [\epsilon_X]_{\alpha\beta}^*. \quad (3.13)$$

First, we should use Eq. (3.12) to calculate the p 's (and d 's), and then, perform the calculations of the oscillations scale, Eq. (3.10). The former will be calculated in Sec. 3.2.2 and the latter in the Sec. 3.2.1.

3.2.1 The oscillation rate

In this section, we will develop the expressions of the oscillation rate analytically. We will separate it among orders of magnitude of ϵ_X and scale of oscillation. Let us begin our understanding listing some properties of Eq. (3.10) and (3.11):

1. The oscillation rates are not oscillation probabilities, but the ratios between the oscillation rates with BSM and the oscillation rates in the SM. Hence, they can be larger than 1;
2. The BSM parameters come always multiplying the PMNS matrix, $\epsilon_X U$;
3. If $\epsilon \rightarrow 0$, we recover the Standard oscillation probability for three neutrinos.

We can use property 2 to reduce the number of parameters of our analysis. That is, we can write the PMNS matrix in terms of mixing angles and redefine the BSM parameters:

$$\epsilon_X U = \epsilon_X U(\theta_{23}, \delta) R(\theta_{13}) R(\theta_{12}) = \tilde{\epsilon}_X R(\theta_{13}) R(\theta_{12}). \quad (3.14)$$

Here we are using an alternative parametrization in the PMNS matrix, where the δ CP violation phase is included in the 23 rotation. In this parametrization of the PMNS matrix, we have:

$$U(\theta_{23}, \delta) = \begin{pmatrix} 1 & 0 & 0 \\ 0 & c_{23} & s_{23} e^{i\delta} \\ 0 & -s_{23} e^{-i\delta} & c_{23} \end{pmatrix}, \quad R_{13} = \begin{pmatrix} c_{13} & 0 & s_{13} \\ 0 & 1 & 0 \\ -s_{13} & 0 & c_{13} \end{pmatrix}, \quad R_{12} = \begin{pmatrix} c_{12} & s_{12} & 0 \\ -s_{12} & c_{12} & 0 \\ 0 & 0 & 1 \end{pmatrix}, \quad (3.15)$$

and $c_{ij} \equiv \cos \theta_{ij}$, $s_{ij} \equiv \sin \theta_{ij}$ for $i, j = 1, 2, 3$. The new effective BSM parameters are

$$[\tilde{\epsilon}_X] \equiv [\epsilon_X]U(\theta_{23}, \delta), \quad (3.16)$$

the same as defined in [41] and [46, 47]:

$$\begin{aligned} [\tilde{\epsilon}_X]_{e\mu} &= c_{23}[\epsilon_X]_{e\mu} - s_{23}[\epsilon_X]_{e\tau}e^{-i\delta}, \\ [\tilde{\epsilon}_X]_{e\tau} &= s_{23}[\epsilon_X]_{e\mu}e^{i\delta} + c_{23}[\epsilon_X]_{e\tau}. \end{aligned}$$

As we can see, we can write the ratio of BSM rates over the SM rates as function of only $\tilde{\epsilon}$. Then, all the dependence of θ_{23} and δ CP-violation is hidden inside the BSM parameters. In this way, our analysis will be independent of the mixing angles θ_{23} and the δ CP-violation phase.

In this analysis, we assume one type of BSM physics for each case: if scalar interactions are present, tensor interactions are not. In addition, we do not assume $[\tilde{\epsilon}_X]_{e\mu}$ and $[\tilde{\epsilon}_X]_{e\tau}$ present at the same time.

From now on, we assume electron disappearance and write Eq (3.10) as

$$\frac{R_{ee}}{\phi_e^{\text{SM}}\sigma_e^{\text{SM}}} = N^{\text{non-osc}} - \sum_{k>l} N_{kl}^{\text{osc}} \sin^2\left(\frac{\phi_{kl}L}{2}\right) + \sum_{k>l} N_{kl}^{\text{CP}} \sin(\phi_{kl}L). \quad (3.17)$$

The $N^{\text{non-osc}}$ is the non-oscillation rate and gives the ratio between the Beyond the Standard Model Physics (BSM) and Standard Model physics if there is no oscillation. For example, in the standard neutrino oscillation, it equals 1. The N_{kl}^{osc} is the amplitude of oscillation for the non-CP violation term, and the novelty is the appearance of the amplitude for the CP-violating term N_{kl}^{CP} . In the Standard Oscillation, for electron disappearance, the CP violation amplitude is zero.

We further assume that the $[\epsilon_X]_{ee}$ for $X = T, S$ receives strong constraints from beta decay and $[\epsilon_L]_{ee}$ is degenerated in the g_V and V_{ud} measurements as shown in [45]. Hence, from now on, we always consider $[\epsilon_X]_{e\alpha}$ with $\alpha \neq e$.

The non-oscillation rate is not dependent on the oscillation scale, ϕ_{kl} , hence it is:

$$N^{\text{non-osc}} = 1 + 2|[\tilde{\epsilon}_X]_{e\alpha}|^2 d_{XL}p_{XL} + |[\tilde{\epsilon}_X]_{e\alpha}|^4 d_{XX}p_{XX} + \mathcal{O}([\epsilon_X]_{ee}), \quad \alpha \neq e. \quad (3.18)$$

One can notice that the $[\tilde{\epsilon}_X]_{e\alpha}$ does not appear at linear order, having only second-order or higher effects. In addition, the neglected diagonal terms $[\epsilon_X]_{ee}$ are:

$$\begin{aligned} \mathcal{O}([\epsilon_X]_{ee}) &= +2[\tilde{\epsilon}_X]_{ee}(d_{XL} + p_{XL}) + ([\tilde{\epsilon}_X]_{ee})^2(d_{XX} + p_{XX} + 4d_X p_X) \\ &\quad + 2([\tilde{\epsilon}_X]_{ee})^3(d_{XX}p_X + p_{XX}d_X) + ([\tilde{\epsilon}_X]_{ee})^4 d_{XX}p_{XX}. \end{aligned} \quad (3.19)$$

Regarding the oscillation scales, we will separate the formulas in atmospheric and solar scales. The former appears when $E_\nu/L \sim 2.5 \times 10^{-3} \text{eV}^2$, and for reactor energies $\sim 4 \text{ MeV}$ it happens around $L \sim 1 \text{ km}$ where this implies $\phi_{31} \sim \phi_{32}$ and $\phi_{21} \sim 0$. In the past, such approximation was called one mass scale dominance approximation. The ϕ_{kl} was defined in Eq. (3.8) and we from that, it follows that $\Delta m_{32}^2 = \Delta m_{31}^2 + \Delta m_{21}^2 \approx \Delta m_{31}^2$ and neglect Δm_{21}^2 . In the case when only $[\tilde{\epsilon}_X]_{e\mu}$ is present:

$$N_{\text{atm}}^{\text{osc}} = N_{31}^{\text{osc}} + N_{32}^{\text{osc}} = s_{2\theta_{13}}^2 \left(1 + \frac{c_{13}^2}{s_{13}^2} |[\tilde{\epsilon}_X]_{e\mu}|^2 d_{\text{XL}} p_{\text{XL}} \right), \quad (3.20)$$

$$N_{\text{atm}}^{\text{CP}} = N_{31}^{\text{CP}} + N_{32}^{\text{CP}} = 0. \quad (3.21)$$

Here, $s_{13} = \sin(\theta_{13})$, $s_{2\theta_{13}} = \sin(2\theta_{13})$ and the same for $\cos \rightarrow c$. If only $[\tilde{\epsilon}_X]_{e\tau}$ is present:

$$\begin{aligned} N_{\text{atm}}^{\text{osc}} = & s_{2\theta_{13}}^2 \left(1 + \frac{c_{2\theta_{13}}}{s_{2\theta_{13}}} \text{Re}\{[\tilde{\epsilon}_X]_{e\tau}\} (d_{\text{XL}} + p_{\text{XL}}) - 4 (\text{Re}\{[\tilde{\epsilon}_X]_{e\tau}\})^2 d_{\text{XL}} p_{\text{XL}} \right) + 4 |[\tilde{\epsilon}_X]_{e\tau}|^2 d_{\text{XL}} p_{\text{XL}} \\ & - s_{2\theta_{13}}^2 |[\tilde{\epsilon}_X]_{e\tau}|^2 (d_{\text{XX}} + p_{\text{XX}} + c_{2\theta_{13}}^2 \text{Re}\{[\tilde{\epsilon}_X]_{e\tau}\} (d_{\text{XX}} p_{\text{XL}} + p_{\text{XX}} d_{\text{XL}}) - |[\tilde{\epsilon}_X]_{e\tau}|^2 d_{\text{XX}} p_{\text{XX}}) \end{aligned} \quad (3.22)$$

$$N_{\text{atm}}^{\text{CP}} = + \text{Im}\{[\tilde{\epsilon}_X]_{e\tau}\} s_{2\theta_{13}} \left((d_{\text{XL}} - p_{\text{XL}}) + |[\tilde{\epsilon}_X]_{e\tau}|^2 s_{2\theta_{13}} (d_{\text{XX}} p_{\text{XL}} - d_{\text{XL}} p_{\text{XX}}) \right) \quad (3.23)$$

From Eqs. (3.20), (3.22) and (3.23), the $[\tilde{\epsilon}_X]_{e\mu}$ appears only in second order with no CP-violation effects while $[\tilde{\epsilon}_X]_{e\tau}$ appears at linear order and presents CP-violation effects. Hence, it is expected that experiments more sensitive to the atmospheric scale have a higher sensitivity to the $[\tilde{\epsilon}_X]_{e\tau}$ in comparison with the $[\tilde{\epsilon}_X]_{e\mu}$ parameter.

Concerning to the CP violation, no sensitivity is expected for CP-violation coming from $[\tilde{\epsilon}_X]_{e\mu}$ in atmospheric scale experiments, only for the $[\tilde{\epsilon}_X]_{e\tau}$ parameters. However, in this section, we will see that some experiments can be sensitive to the CP-violation of $[\tilde{\epsilon}_X]_{e\mu}$ coming from the solar scale.

In the solar scale, the active mass difference is $\Delta m_{21}^2 \approx 7 \times 10^{-5} \text{eV}^2$. Reactor experiments (with energies of around 4 MeV) with distances around 100 km can be sensitive to the solar mass scale. The amplitudes, in that case, for $[\tilde{\epsilon}_X]_{e\mu}$

$$\begin{aligned} N_{\text{Sun}}^{\text{osc}} = & c_{13}^4 s_{2\theta_{12}}^2 - \text{Re}\{[\tilde{\epsilon}_X]_{e\mu}\} c_{13}^3 s_{4\theta_{12}} (d_{\text{XL}} + p_{\text{XL}}) \\ & + (|[\tilde{\epsilon}_X]_{e\mu}|^2 + \text{Re}\{[\tilde{\epsilon}_X]_{e\mu}\}^2 s_{2\theta_{12}}^2) 4c_{13}^2 d_{\text{XL}} p_{\text{XL}} - |[\tilde{\epsilon}_X]_{e\mu}|^2 s_{2\theta_{12}}^2 (d_{\text{XX}} + p_{\text{XX}}) \\ & - |[\tilde{\epsilon}_X]_{e\mu}|^2 \text{Re}\{[\tilde{\epsilon}_X]_{e\mu}\} c_{13} s_{4\theta_{12}}^2 (d_{\text{XX}} p_{\text{XL}} + p_{\text{XX}} d_{\text{XL}}) + |[\tilde{\epsilon}_X]_{e\mu}|^4 s_{2\theta_{12}}^2 d_{\text{XX}} p_{\text{XX}} \end{aligned} \quad (3.24)$$

$$N_{\text{Sun}}^{\text{CP}} = + [c_{13}^2 (d_{\text{XL}} - p_{\text{XL}}) + |[\tilde{\epsilon}_X]_{e\mu}|^2 (d_{\text{XX}} p_{\text{XL}} - d_{\text{XL}} p_{\text{XX}})] \text{Im}\{[\tilde{\epsilon}_X]_{e\mu}\} c_{13} s_{2\theta_{12}} \quad (3.25)$$

and for $[\tilde{\epsilon}_X]_{e\tau}$

$$\begin{aligned}
N_{\text{Sun}}^{\text{osc}} = & c_{13}^4 s_{2\theta_{12}}^2 - 2s_{13}c_{13}^3 \text{Re}\{[\tilde{\epsilon}_X]_{e\tau}\}(d_{\text{XL}} + p_{\text{XL}})s_{2\theta_{12}}^2 \\
& + s_{2\theta_{13}}^2 s_{2\theta_{12}}^2 \text{Re}\{[\tilde{\epsilon}_X]_{e\tau}\}^2 d_{\text{XL}} p_{\text{XL}} + \frac{1}{4} |[\tilde{\epsilon}_X]_{e\tau}|^2 s_{2\theta_{12}}^2 4s_{13}^2 c_{13}^2 (d_{\text{XX}} + p_{\text{XX}}) \\
& - c_{13} s_{13}^3 |[\tilde{\epsilon}_X]_{e\tau}|^2 s_{4\theta_{12}}^2 \text{Re}\{[\tilde{\epsilon}_X]_{e\tau}\} (d_{\text{XX}} p_{\text{XL}} + p_{\text{XX}} d_{\text{XL}}) \\
& + s_{13}^4 |[\tilde{\epsilon}_X]_{e\tau}|^4 d_{\text{XX}} p_{\text{XX}} s_{2\theta_{12}}^2
\end{aligned} \tag{3.26}$$

$$N_{\text{Sun}}^{\text{CP}} = 0. \tag{3.27}$$

Both parameters appear in linear order, however $[\tilde{\epsilon}_X]_{e\tau}$ can be suppressed by a small θ_{13} (it always comes multiplied by s_{13}). In solar scale, the opposite happens: the CP-violation terms exist only for the $[\tilde{\epsilon}_X]_{e\mu}$ parameter. As we have already mentioned, experiments constructed on the atmospheric mass-scales assumption can also be sensitive to Eq. (3.25). It comes from the fact that the amplitudes N_{kl}^{CP} are multiplied by $\sin(\phi_{kl})$ and not by $\sin^2(\phi_{kl}/2)$. Hence, the CP-violating term can reach the same size as the standard oscillation term from Δm_{31}^2 , which happens when

$$\text{Im}\{[\tilde{\epsilon}_X]_{e\mu}\} s_{2\theta_{12}} \sin(\Delta_{21}) \sim s_{2\theta_{13}}^2 \sin^2(\Delta_{31}). \tag{3.28}$$

As we will see, this results has some implications for our study.

In addition, if one wants to split the atmospheric mass scale to the study of the mass hierarchy, we present our formulas when $\Delta m_{32}^2 = \Delta m_{31}^2 + \Delta m_{21}^2 \approx \Delta m_{31}^2$ is not true anymore. The N_{3i}^{osc} are different for $i = 1, 2$. In the $[\tilde{\epsilon}_X]_{e\tau}$ case, they are proportional to the coefficients, $N_{\text{atm}}^{\text{osc}}$ and $N_{\text{CP}}^{\text{osc}}$ as

$$N_{32}^{\text{osc}} = N_{\text{atm}}^{\text{osc}} s_{12}^2, \quad N_{31}^{\text{osc}} = N_{\text{atm}}^{\text{osc}} c_{12}^2, \tag{3.29}$$

$$N_{32}^{\text{CP}} = N_{\text{atm}}^{\text{CP}} s_{12}^2, \quad N_{31}^{\text{CP}} = N_{\text{atm}}^{\text{CP}} c_{12}^2. \tag{3.30}$$

In contrast, for the $[\tilde{\epsilon}_X]_{e\mu}$ parameter, we have more complex changes:

$$N_{32}^{\text{osc}} = s_{2\theta_{13}}^2 s_{12}^2 + \text{Re}\{[\tilde{\epsilon}_X]_{e\mu}\} (p_{\text{XL}} + d_{\text{XL}}) s_{2\theta_{12}} c_{13} s_{13}^2 + 4 |[\tilde{\epsilon}_X]_{e\mu}|^2 d_{\text{XL}} p_{\text{XL}} s_{13} c_{12}^2 \tag{3.31}$$

$$N_{32}^{\text{CP}} = -\text{Im}\{[\tilde{\epsilon}_X]_{e\mu}\} (p_{\text{XL}} - d_{\text{XL}}) s_{2\theta_{12}} c_{13} s_{13}^4, \tag{3.32}$$

$$N_{31}^{\text{osc}} = s_{2\theta_{13}}^2 c_{12}^2 - \text{Re}\{[\tilde{\epsilon}_X]_{e\mu}\} (p_{\text{XL}} + d_{\text{XL}}) s_{2\theta_{12}} c_{13} s_{13}^2 + 4 |[\tilde{\epsilon}_X]_{e\mu}|^2 d_{\text{XL}} p_{\text{XL}} s_{13} s_{12}^2 \tag{3.33}$$

$$N_{31}^{\text{CP}} = +\text{Im}\{[\tilde{\epsilon}_X]_{e\mu}\} (p_{\text{XL}} - d_{\text{XL}}) s_{2\theta_{12}} c_{13} s_{13}^4. \tag{3.34}$$

Now that we have an overview of the analytical aspect of the oscillation rate, we can proceed to the amplitude calculations.

3.2.2 Amplitude calculation

Now that we have a better understanding of the oscillations formulas in each scale, it is time to look at the process of neutrino production and detection. We will focus on neutrino beta decay and inverse beta decay. Here, we restrict our work to scalar and tensor interactions. The Lagrangian is given by Eq. (3.3), where we separate the Standard Model Lagrangian \mathcal{L}_{SM} , the scalar interaction, \mathcal{L}_S and the tensor interaction, \mathcal{L}_T :

$$\mathcal{L}_{SM} = -\frac{G_F V_{ud}}{\sqrt{2}} [(g_V \bar{p} \gamma^\mu n - g_A \bar{p} \gamma^\mu \gamma_5 n) (\bar{l}_\alpha \gamma_\mu P_L \nu_\alpha)] + h.c., \quad (3.35)$$

$$\mathcal{L}_S = +\frac{G_F V_{ud}}{\sqrt{2}} g_S [\epsilon_S]_{\alpha\beta} (\bar{p} n) (\bar{l}_\alpha P_L \nu_\beta) + h.c., \quad (3.36)$$

$$\mathcal{L}_T = -\frac{G_F V_{ud}}{2\sqrt{2}} g_T [\epsilon_T]_{\alpha\beta} (\bar{p} \sigma^{\mu\nu} P_L n) (\bar{l}_\alpha \sigma_{\mu\nu} P_L \nu_\beta) + h.c. \quad (3.37)$$

There are two main types of standard weak interactions at low energies: the Fermi interaction and the Gamow-Teller one. The Fermi interaction is mainly related to the vector component of the weak Lagrangian, while the Gamow-Teller one is related to the axial part. In beta-decay at reactors, most of the decays are of Gamow-Teller type; hence, the vector part of the interactions can be neglected for the production in reactors.

At low energies, the hadronic current in the Lagrangian (up to second-order derivatives) reduces to the structure of Gamow-Teller or Fermi interactions. Moreover, as can be seen from Ref. [41], the pure scalar interactions reduce to Fermi transitions while the Tensor ones reduce to Gamow-Teller.

Our goal is to calculate the oscillation ratios, Eq. (3.17), which implies calculating all possible combinations of amplitude products:

$$\mathcal{M}_{XY} = \int \sum_{\text{spin}} A_X A_Y^* d\Pi. \quad (3.38)$$

It corresponds to the numerators and denominators of Eq. (3.12). At the end of the day, the production and detection factors can be found in Eq. (3.12). We begin our calculation by focusing on the detection process. In the end, we go to the production process.

Neutrino and antineutrino detection

As we have already seen, neutrino detection can appear in two types: charged current and neutral current signal. In our case, only the charged current is affected by new interactions. Hence, we are interested in two of the Feynman diagrams in Figure 3.1:

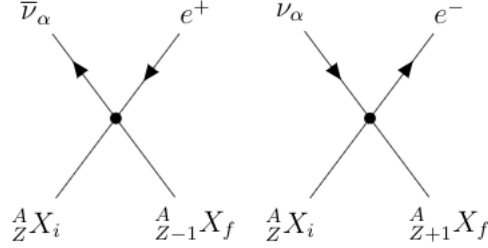


Figure 3.1: The four-vertex Feynman diagram for the anti-neutrino and neutrino detection. One can read the Feynman diagram from the left to the right.

All the interactions depend on nuclear effects, which can play an important role depending on the process. First, we will look at the neutrino detection through the charged current. The amplitudes are:

$$\mathcal{A}_{X=S,T} = -i \langle \nu_e, X_i | \mathcal{L}_X | e^- X_f \rangle. \quad (3.39)$$

In the case of antineutrinos one should change $\nu_e \rightarrow \bar{\nu}_e$ and $e^- \rightarrow e^+$. Then, using the Feynman rules, one can find

$$\mathcal{A}_X = -i \frac{G_F V_{ud}}{\sqrt{2}} [\epsilon_X]_{\alpha\beta} [\bar{u}_{e^-}(p_e) \Gamma_X^l u_\nu(p_\nu) \times g_X \bar{u}_p(p_p) \Gamma_X^h u_n(p_n)]. \quad (3.40)$$

The same expression is valid for the Standard Model, but one should use the identity matrix instead of using $[\epsilon_X]$. We can now, substitute Eq. (3.40) in Eq. (3.38):

$$\begin{aligned} \mathcal{M}_{XY} = \int d\Pi \frac{G_F^2 V_{ud}^2}{2} [\epsilon_X]_{\alpha\beta} [\epsilon_Y]_{\alpha\beta} \sum_{spin} [\bar{u}_{e^-}(p_e) \Gamma_X^l u_\nu(p_\nu)] [g_X \bar{u}_p(p_p) \Gamma_X^h u_n(p_n)] \\ [\bar{u}_{e^-}(p_e) \Gamma_Y^l u_\nu(p_\nu)]^* [g_X \bar{u}_p(p_p) \Gamma_Y^h u_n(p_n)]^*. \end{aligned} \quad (3.41)$$

Here, α and β represent the neutrino flavors. Using Casimir's trick, and one can find

$$\begin{aligned} \mathcal{M}_{XY} \propto \int d\Pi \frac{G_F^2 V_{ud}^2}{2} [\epsilon_X]_{\alpha\beta} [\epsilon_Y]_{\alpha\beta} g_X g_Y \text{Tr} \left[\Gamma_X^l \not{p}_\nu \bar{\Gamma}_Y^l (\not{p}_e + m_e) \right] \times \\ \text{Tr} \left[\Gamma_X^h (\not{p}_p + m_p) \bar{\Gamma}_Y^h (\not{p}_n + m_n) \right]. \end{aligned} \quad (3.42)$$

Here, we should calculate the traces for each combination between the interactions: scalar, tensor, vector, and axial. Let us begin with the combination of the scalar with the others³:

$$\begin{aligned}
(\text{vector x scalar}) &= \frac{1}{2} \text{Tr} \left[\gamma_\alpha (1 - \gamma_5) \not{p}_\nu (1 + \gamma_5) (\not{p}_e + m_e) \right] \text{Tr} \left[\gamma^\alpha (\not{p}_p + m_p) (\not{p}_n + m_n) \right] \\
&= \frac{1}{2} \text{Tr} \left[\gamma_\alpha (1 - \gamma_5) \not{p}_\nu (1 + \gamma_5) (\not{p}_e + m_e) \right] 4 [p_n^\alpha m_p + p_p^\alpha m_n] \\
&= [2(p_\nu)_\alpha m_e] 4 [p_n^\alpha m_p + p_p^\alpha m_n] = 16m_e [(p_\nu \cdot p_n) m_p + (p_\nu \cdot p_p) m_n],
\end{aligned} \tag{3.43}$$

$$\begin{aligned}
(\text{axial x scalar}) &= \frac{1}{2} \text{Tr} \left[\gamma^\mu (1 - \gamma_5) \not{p}_\nu (1 + \gamma_5) (\not{p}_e + m_e) \right] \text{Tr} \left[\gamma_\mu \gamma_5 (\not{p}_p + m_p) (\not{p}_n + m_n) \right] \\
&= \frac{1}{2} \text{Tr} \left[\gamma^\mu (1 - \gamma_5) \not{p}_\nu (1 + \gamma_5) (\not{p}_e + m_e) \right] \times 0 \\
&= 0.
\end{aligned} \tag{3.44}$$

$$\begin{aligned}
(\text{scalar x scalar}) &= \frac{1}{2} \text{Tr} \left[(1 - \gamma_5) \not{p}_\nu (1 + \gamma_5) (\not{p}_e + m_e) \right] \text{Tr} \left[(\not{p}_p + m_p) (\not{p}_n + m_n) \right] \\
&= \frac{1}{2} \text{Tr} \left[(1 - \gamma_5) \not{p}_\nu (1 + \gamma_5) (\not{p}_e + m_e) \right] \times 4 [p_p \cdot p_n + m_p m_n] \\
&= 16(p_\nu \cdot p_e)(p_p \cdot p_n + m_p m_n).
\end{aligned} \tag{3.45}$$

We check that our calculations agree with the calculations performed in the Software Mathematica. Hence, from now on, we will use the Mathematica output results. Bellow, we show the remaining traces between vector, axial and tensor combinations.

$$\begin{aligned}
(\text{vector x vector}) &= \frac{1}{2} \text{Tr} \left[\gamma_\alpha (1 - \gamma_5) \not{p}_\nu \gamma_\beta (1 + \gamma_5) (\not{p}_e + m_e) \right] \text{Tr} \left[\gamma^\alpha (\not{p}_p + m_p) \gamma^\beta (\not{p}_n + m_n) \right] \\
&= 32 [-m_n m_p (p_\nu \cdot p_e) + (p_n \cdot p_e)(p_\nu \cdot p_p) - (p_\nu \cdot p_n)(p_p \cdot p_e)],
\end{aligned} \tag{3.46}$$

$$\begin{aligned}
(\text{axial x axial}) &= \frac{1}{2} \text{Tr} \left[\gamma_\alpha \gamma_5 (1 - \gamma_5) \not{p}_\nu \gamma_\beta \gamma_5 (1 + \gamma_5) (\not{p}_e + m_e) \right] \text{Tr} \left[\gamma^\alpha \gamma_5 (\not{p}_p + m_p) \gamma^\beta \gamma_5 (\not{p}_n + m_n) \right] \\
&= 32 [+m_n m_p (p_\nu \cdot p_e) + (p_n \cdot p_e)(p_\nu \cdot p_p) - (p_\nu \cdot p_n)(p_p \cdot p_e)],
\end{aligned} \tag{3.47}$$

$$\begin{aligned}
(\text{vector x axial}) &= \frac{1}{2} \text{Tr} \left[\gamma_\alpha (1 - \gamma_5) \not{p}_\nu \gamma_\beta \gamma_5 (1 + \gamma_5) (\not{p}_e + m_e) \right] \text{Tr} \left[\gamma^\alpha (\not{p}_p + m_p) \gamma^\beta \gamma_5 (\not{p}_n + m_n) \right] \\
&= 64 [(p_n \cdot p_e)(p_\nu \cdot p_p) - (p_\nu \cdot p_n)(p_p \cdot p_e)].
\end{aligned} \tag{3.48}$$

³We will not calculate the trace between scalar and tensor interaction since they are not used in this work.

$$\begin{aligned}
(\text{tensor x vector}) &= \frac{1}{2} \text{Tr} \left[\sigma_{\alpha\delta} (1 - \gamma_5) \not{p}_\nu \gamma_\beta (1 + \gamma_5) (\not{p}_e + m_e) \right] \text{Tr} \left[\sigma^{\alpha\delta} (\not{p}_p + m_p) \gamma^\beta (\not{p}_n + m_n) \right] \\
&= 48 \times 4 \times m_e [(p_\nu \cdot p_p) m_n - (p_\nu \cdot p_n) m_p],
\end{aligned} \tag{3.49}$$

$$\begin{aligned}
(\text{tensor x axial}) &= \frac{1}{2} \text{Tr} \left[\sigma_{\alpha\delta} (1 - \gamma_5) \not{p}_\nu \gamma_\beta \gamma_5 (1 + \gamma_5) (\not{p}_e + m_e) \right] \text{Tr} \left[\sigma^{\alpha\delta} (\not{p}_p + m_p) \gamma^\beta \gamma_5 (\not{p}_n + m_n) \right] \\
&= 48 \times 4 \times m_e [(p_\nu \cdot p_p) m_n + (p_\nu \cdot p_n) m_p],
\end{aligned} \tag{3.50}$$

$$\begin{aligned}
(\text{tensor x tensor}) &= \frac{1}{2} \text{Tr} \left[\sigma_{\alpha\beta} (1 - \gamma_5) \not{p}_\nu \sigma_{\delta\eta} (1 + \gamma_5) (\not{p}_e + m_e) \right] \text{Tr} \left[\sigma^{\alpha\beta} (\not{p}_p + m_p) \sigma^{\delta\eta} (\not{p}_n + m_n) \right] \\
&= 16 [2(p_n \cdot p_e)(p_\nu \cdot p_p) + 2(p_\nu \cdot p_n)(p_p \cdot p_e) - (p_p \cdot p_n)(p_\nu \cdot p_e)].
\end{aligned} \tag{3.51}$$

Now, we should calculate the integral in the phase space. For the detection case, one should have:

$$\begin{aligned}
\mathcal{M}_{XY} &= A_X A_Y^* d\Pi = (\dots) d\Pi \propto (\dots) \delta^4(p_\nu + p_n - p_p - p_e) \frac{d^3 \vec{p}_p}{E_p} \frac{d^3 \vec{p}_e}{E_e} \\
&= (\dots) \delta(E_\nu + E_n - E_p - E_e) \delta^3(\vec{p}_\nu + \vec{p}_n - \vec{p}_p - \vec{p}_e) \frac{d^3 \vec{p}_p}{E_p} \frac{d^3 \vec{p}_e}{E_e},
\end{aligned} \tag{3.52}$$

If we assume the nucleons at rest (or negligible recoil contribution of the final nucleon) and neglect neutrino masses, it is possible to reduce Eq. (3.52) to

$$\begin{aligned}
\mathcal{M}_{XY} &= (\dots) d\Pi \propto (\dots) \delta(E_\nu + m_n - m_p - E_e) \delta^3(\vec{p}_\nu - \vec{p}_e - \vec{p}_p) \frac{d^3 \vec{p}_p}{m_p E_e} \\
&= (\dots) \delta(E_\nu + m_n - m_p - E_e) p_e \frac{d \cos \theta d\phi dE_e}{m_p E_e} = (\dots) 2\pi p_e \frac{d \cos \theta}{m_p E_e}.
\end{aligned} \tag{3.53}$$

From equation (3.53) we got the constraints: $\vec{p}_\nu - \vec{p}_e = \vec{p}_p$ and $E_e = E_\nu + \Delta$ where $\Delta = m_n - m_p$. In the case of nuclei, the Δ can be substituted by $\Delta_{if} = m_f - m_i$, where m_f and m_i are the masses of the initial and final states of the nuclei. Now, we can apply Eq. (3.53) to our amplitudes, for the standard mode traces, we will have

$$\begin{aligned}
\mathcal{M}_{LL}^{SM} &\propto g_V^2 (\text{vector x vector}) + g_A^2 (\text{axial x axial}) + g_V g_A [(\text{vector x axial}) + (\text{axial x vector})] \\
&= 64 \{ (g_A + g_V) [m_n m_p (g_A - g_V) (p_\nu \cdot p_e) + (g_A + g_V) (p_n \cdot p_e) (p_\nu \cdot p_p)] \\
&\quad + (g_A - g_V)^2 (p_\nu \cdot p_n) (p_p \cdot p_e) \}.
\end{aligned} \tag{3.54}$$

Under our kinematic assumptions, we have:

$$\begin{aligned}
p_\nu \cdot p_n &\approx E_\nu m_n, \\
p_\nu \cdot p_p &\approx E_\nu m_p, \\
p_\nu \cdot p_e &\approx E_\nu E_e - p_e p_\nu \cos \theta, \\
p_e \cdot p_n &\approx E_e m_n, \\
p_e \cdot p_p &\approx E_e m_p, \\
p_p \cdot p_n &\approx m_p m_n.
\end{aligned} \tag{3.55}$$

Hence, the standard model amplitude become:

$$\mathcal{M}_{LL}^{SM} \propto 64 m_n m_p E_\nu E_e [g_A^2 (3 - v_e \cos \theta) + g_V^2 (1 + v_e \cos \theta)], \tag{3.56}$$

where

$$v_e = \frac{p_e}{E_e}. \tag{3.57}$$

Now we can apply the angular contribution coming from the phase-space integration, and the amplitude is integrated over $\cos \theta$ from -1 to 1 , leading to

$$\int_{-1}^1 \mathcal{M}_{LL}^{SM} d(\cos \theta) \propto 64 E_\nu E_e m_n m_p (3g_A^2 + g_V^2). \tag{3.58}$$

For the scalar scenarios, we have

$$\begin{aligned}
\mathcal{M}_{SL} &\propto + 32 g_S g_V E_\nu m_p m_n m_e, \\
\int_{-1}^1 \mathcal{M}_{SL} d(\cos \theta) &\propto + 64 g_S g_V E_\nu m_p m_n m_e,
\end{aligned} \tag{3.59}$$

$$\begin{aligned}
\mathcal{M}_{SS} &\propto + 32 g_S^2 E_\nu E_e (1 - v_e \cos \theta) m_p m_n, \\
\int_{-1}^1 \mathcal{M}_{SS} d(\cos \theta) &\propto + 64 g_S g_V E_\nu E_e m_p m_n.
\end{aligned} \tag{3.60}$$

For tensor interactions, we will have

$$\begin{aligned}
\mathcal{M}_{TL} &\propto + 96 g_T g_V E_\nu m_p m_n m_e, \\
\int_{-1}^1 \mathcal{M}_{TL} d(\cos \theta) &\propto + 192 g_T g_V E_\nu m_p m_n m_e,
\end{aligned} \tag{3.61}$$

$$\begin{aligned}
\mathcal{M}_{TT} &\propto + 32 g_T^2 E_\nu E_e (3 + v_e \cos \theta) m_p m_n, \\
\int_{-1}^1 \mathcal{M}_{TT} d(\cos \theta) &\propto + 192 g_T^2 E_\nu E_e m_p m_n.
\end{aligned} \tag{3.62}$$

From kinematic considerations, the interference between the tensor and axial contributions is zero. Furthermore, substituting equations (3.58), (3.59), (3.60), (3.61) and (3.62) in eq. (3.12), we should have the following terms for Fermi plus Gamow-Teller interactions:

$$\begin{aligned} d_{\text{SL}} &= \frac{g_S g_V}{g_V^2 + 3g_A^2} \frac{m_e}{E_e}, & d_{\text{SS}} &= \frac{g_S^2}{g_V^2 + 3g_A^2}, \\ d_{\text{TL}} &= \frac{3g_A g_T}{g_V^2 + 3g_A^2} \frac{m_e}{E_e}, & d_{\text{TT}} &= \frac{3g_T^2}{g_V^2 + 3g_A^2}, \end{aligned} \quad (3.63)$$

where $m_e = 0.511$ MeV is the electron mass. At low-energy, the electron energy spectrum is related to the neutrino electron spectrum by the relation

$$E_e = E_\nu - \Delta_{if}, \quad (3.64)$$

where $\Delta_{if} = m_f - m_i$ is the mass difference between the final and initial nuclei.

Neutrino and antineutrino production

In the electron neutrino nuclear production, we have a similar calculation and three types of neutrino production:

$$\mathcal{M}_X^{\beta^+} = -i \langle X_i | \mathcal{L}_X | e^+, X_f, \nu_e \rangle, \quad (3.65)$$

$$\mathcal{M}_X^{\beta^-} = -i \langle X_i | \mathcal{L}_X | e^-, X_f, \bar{\nu}_e \rangle, \quad (3.66)$$

$$\mathcal{M}_X^{E.C.} = -i \langle X_i, e^- | \mathcal{L}_X | X_f, \nu_e \rangle. \quad (3.67)$$

respectively, the β^+ , the β^- and the electron capture (E.C.). Those interactions can be represented by the following diagrams

In the case of production, the main difference is the integral in the phase space, which is the same for all interactions. So, the amplitudes will be

$$\mathcal{M}_X^{\beta^+} = -i \frac{G_F V_{ud}}{\sqrt{2}} [\epsilon_X]_{\alpha\beta} [\bar{\nu}_{e^+}(p_e) \Gamma_X^l u_\nu(p_\nu) \times g_X \bar{u}_n(p_n) \Gamma_X^h u_p(p_p)], \quad (3.68)$$

$$\mathcal{M}_X^{\beta^-} = -i \frac{G_F V_{ud}}{\sqrt{2}} [\epsilon_X]_{\alpha\beta} [\bar{u}_{e^-}(p_e) \Gamma_X^l u_\nu(p_\nu) \times g_X \bar{u}_p(p_p) \Gamma_X^h u_n(p_n)], \quad (3.69)$$

$$\mathcal{M}_X^{E.C.} = -i \frac{G_F V_{ud}}{\sqrt{2}} [\epsilon_X]_{\alpha\beta} [\bar{u}_\nu(p_\nu) \Gamma_X^l u_{e^-}(p_e) \times g_X \bar{u}_n(p_n) \Gamma_X^h u_p(p_p)]. \quad (3.70)$$

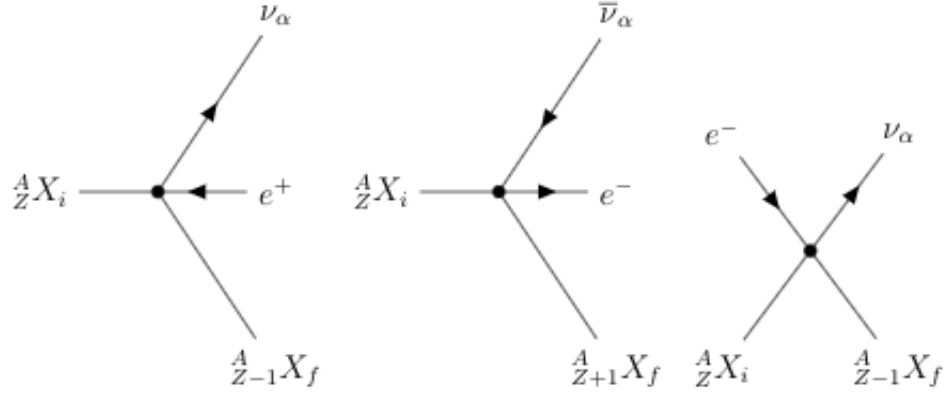


Figure 3.2: Here we show the four-vertex Feynman diagrams for the neutrino and antineutrino production. In the left, there is the β^+ decay, in the center the β^- , and on the right side, the electron capture (E.C.). We assume a horizontal time-arrow from left to right for those diagrams.

Performing the same calculation as for detection (for beta decays), we will find very similar expressions for the traces. For β^- , the traces are the same as for neutrino detection because of eq. (3.40) is equals to eq. (3.69). The kinematics is the same as in eq. (3.55), so we should find similar expressions for β^- in the case of Fermi plus Gamow-Teller interactions:

$$\begin{aligned}
 p_{\text{SL}}^{\beta^-} &= \frac{g_S g_V}{g_V^2 + 3g_A^2} \frac{m_e}{E_e}, & p_{\text{SS}}^{\beta^-} &= \frac{g_S^2}{g_V^2 + 3g_A^2}, \\
 p_{\text{TL}}^{\beta^-} &= \frac{3g_A g_T}{g_V^2 + 3g_A^2} \frac{m_e}{E_e}, & p_{\text{TT}}^{\beta^-} &= \frac{3g_T^2}{g_V^2 + 3g_A^2}.
 \end{aligned}
 \tag{3.71}$$

For β^+ , the expression should be the same as for antineutrino detection, therefore, similar to [41]

$$\begin{aligned}
 p_{\text{SL}}^{\beta^+} &= -\frac{g_S g_V}{g_V^2 + 3g_A^2} \frac{m_e}{E_e}, & p_{\text{SS}}^{\beta^+} &= \frac{g_S^2}{g_V^2 + 3g_A^2}, \\
 p_{\text{TL}}^{\beta^+} &= \frac{3g_A g_T}{g_V^2 + 3g_A^2} \frac{m_e}{E_e}, & p_{\text{TT}}^{\beta^+} &= \frac{3g_T^2}{g_V^2 + 3g_A^2}.
 \end{aligned}
 \tag{3.72}$$

As already mentioned, there are two types of weak interactions at low energies: the Fermi and the Gamow-Teller. Moreover, at low energy, the pure scalar one reduces to Fermi transitions and the tensor one to Gamow-Teller transitions. Hence, if we have a process where one should consider only Gamow-Teller transitions (as in the reactor or solar neutrino production), one should find:

$$\begin{aligned}
p_{\text{SL}}^{\beta\pm} &= 0, & p_{\text{SS}}^{\beta\pm} &= \frac{g_S^2}{3g_A^2}, \\
p_{\text{TL}}^{\beta\pm} &= \frac{g_T}{g_A} \frac{m_e}{E_e}, & p_{\text{TT}}^{\beta\pm} &= \frac{g_T^2}{g_A^2}.
\end{aligned}
\tag{3.73}$$

3.2.3 Solar neutrino oscillation

The description of neutrinos coming from the sun is not the same as for neutrinos in the vacuum as discussed in Sec. 3.2.1. In the sun, the neutrino is produced subjected to matter effects, an effective potential created by the coherent forward neutrino scattering in the matter. The matter potential is given by:

$$V_e(x) = \sqrt{2}G_F N_e(x). \tag{3.74}$$

Here $N_e(x)$ is the number density of electrons at the position x , and the potential appears only at the electron neutrino component of the evolution. Due to the nature of the profile of matter density in the sun, for usual oscillations we have that all transitions are adiabatic, and, the mass eigenstate do not change along the path [48]. In addition, the initial neutrino state is the state in the matter, given by a rotation of the mixing angles in the matter (for two neutrinos):

$$\cos 2\tilde{\theta}_{12} = \frac{\Delta m_{21}^2 \cos 2\theta_{12} - V_{CC}}{\Delta m_M^2} \quad \text{e} \quad \sin 2\tilde{\theta}_{12} = \frac{\Delta m_{21}^2 \sin 2\theta_{12}}{\Delta m_M^2}, \tag{3.75}$$

where

$$\Delta m_M^2 = \sqrt{\Delta m_{21}^2 \sin^2 2\theta_{12} + (V_{CC} - \Delta m_{21}^2 \cos 2\theta_{12})}. \tag{3.76}$$

The solar neutrinos do not have the same oscillation pattern as in vacuum (the oscillation exists but is averaged out), and it arrives in the detector as an incoherent admixture of mass eigenstates. Hence, Eq. (3.10) becomes:

$$\frac{R_{\alpha\beta}}{\phi_\alpha^{\text{SM}}\sigma_\beta^{\text{SM}}} = \sum_{kl} \delta_{kl} \left[\tilde{V}_\alpha^{kl}(p_X) \right] \times \left[V_\beta^{kl}(d_X) \right]^*, \tag{3.77}$$

where we use the same expression in Eq. (3.11), making the replacement of $V \rightarrow \tilde{V}$ (vacuum to matter) when neutrinos are in the matter. This expression can be written as:

$$\begin{aligned}
\frac{R_{\alpha\beta}}{\phi_\alpha^{\text{SM}}\sigma_\beta^{\text{SM}}} &= \sum_k (|\tilde{U}_{\alpha k}|^2 + 2 \text{Re} \{ p_{\text{XL}}(\epsilon_X \tilde{U})_{\alpha k}^* \tilde{U}_{\alpha k} \} + |p_{\text{XX}}(\epsilon_X \tilde{U})_{\alpha k}|^2) \\
&\quad \times (|U_{\beta k}|^2 + 2 \text{Re} \{ d_{\text{XL}}(\epsilon_X U)_{\beta k}^* U_{\beta k} \} + |d_{\text{XX}}(\epsilon_X U)_{\beta k}|^2)
\end{aligned}
\tag{3.78}$$

As can be seen, Eq. (3.78) has no CP violation term, despite the sensitivity to the CP violation phase of the $\text{Re}\{\cdot\cdot\cdot\}$ terms. If one neglects NSI, it is possible to recover the standard expressions for solar neutrinos.

The sun produces mainly electron neutrinos, and we can write the electron flux and see how does it depends on the mass states:

$$\Phi(\nu_k) = \phi^{SM}(\nu_e) \left(P_{ek}^{SM} + 2 \text{Re}\{p_{XL}(\epsilon_X \tilde{U})_{\alpha k}^* \tilde{U}_{\alpha k}\} + |p_{XX}(\epsilon_X \tilde{U})_{\alpha k}|^2 \right) \quad (3.79)$$

and, similarly, we can write an effective cross-section of detecting a β -flavoured neutrino on the detector from a mass state k :

$$\sigma_{\beta}(\nu_k) = \sigma_{\beta}^{SM} \left(P_{k\beta}^{SM} + 2 \text{Re}\{d_{XL}(\epsilon_X U)_{\beta k}^* U_{\beta k}\} + |d_{XX}(\epsilon_X U)_{\beta k}|^2 \right). \quad (3.80)$$

We can calculate the rates based on the 3ν scenario explicitly showing the mixing angles with these expressions in hand. Based on our calculations, for solar production of mass states and considering the $[\tilde{\epsilon}_X]_{e\mu}$, we have:

$$\begin{aligned} P_{e1} &\rightarrow P_{e1}^{SM} - 2 \text{Re}\{[\tilde{\epsilon}_X]_{e\mu}\} p_{XL} \tilde{s}_{12} \tilde{c}_{12} c_{13} + |[\tilde{\epsilon}_X]_{e\mu}|^2 p_{XX} \tilde{s}_{12}^2, \\ P_{e2} &\rightarrow P_{e2}^{SM} + 2 \text{Re}\{[\tilde{\epsilon}_X]_{e\mu}\} p_{XL} \tilde{s}_{12} \tilde{c}_{12} c_{13} + |[\tilde{\epsilon}_X]_{e\mu}|^2 p_{XX} \tilde{c}_{12}^2, \\ P_{e3} &= P_{e3}^{SM}. \end{aligned} \quad (3.81)$$

For $[\tilde{\epsilon}_X]_{e\tau}$, we have:

$$\begin{aligned} P_{e1} &\rightarrow P_{e1}^{SM} - 2 \text{Re}\{[\tilde{\epsilon}_X]_{e\tau}\} p_{XL} \tilde{c}_{12}^2 s_{13} c_{13} + |[\tilde{\epsilon}_X]_{e\tau}|^2 p_{XX} \tilde{c}_{12}^2 s_{13}^2, \\ P_{e2} &\rightarrow P_{e2}^{SM} - 2 \text{Re}\{[\tilde{\epsilon}_X]_{e\tau}\} p_{XL} \tilde{s}_{12}^2 s_{13} c_{13} + |[\tilde{\epsilon}_X]_{e\tau}|^2 p_{XX} \tilde{s}_{12}^2 s_{13}^2, \\ P_{e3} &= P_{e3}^{SM} + 2 \text{Re}\{[\tilde{\epsilon}_X]_{e\tau}\} p_{XL} c_{13} + |[\tilde{\epsilon}_X]_{e\tau}|^2 p_{XX} \tilde{c}_{13}^2. \end{aligned} \quad (3.82)$$

For the detection we obtain similar expressions but changing $d \rightarrow p$ and $\tilde{U} \rightarrow U$.

For $[\tilde{\epsilon}_X]_{e\tau}$ parameters the changes on the probabilities that appear in the two first families are suppressed by the small value of θ_{13} , as can be seen in Eq. (3.82). As the first two families are the most important for solar neutrinos, we expect that solar experiments do not have considerable sensitivity to the $\tilde{\epsilon}_{e\tau}$ parameter. Indeed, we explicitly checked that the constraints on $[\tilde{\epsilon}_X]_{e\tau}$ from solar neutrino data are much weaker than those coming from reactor neutrino experiments. As for the $[\tilde{\epsilon}_X]_{e\tau}$ parameter, it appears only in the first two families but is not suppressed by any parameter.

As an additional effect, if the neutrinos arrive at the detector during the night, the coherence between mass eigenstates is reestablished, and flavor oscillation can be probed. Finally, we developed expressions to include NSI on neutrino regeneration on Earth and explicitly checked that its effect on the constraints is marginal.

3.3 Case study: solar neutrinos and reactors

This section introduces the details of the simulation of solar and reactor neutrinos under the scope of the theory developed in the last section. As will be seen, only scalar and non-standard tensor solar interactions will be considered. The neutrinos will be produced at the source in the presence of the new interactions from the Lagrangian in Eq. (3.3), will travel a given distance, and will be detected at the experiment with an electron signal (also with the presence of new interactions). Before going into the details about the simulation, we will discuss some statistics used in this work.

3.3.1 Statistics

Neutrinos are particles that rarely interact with other particles, e.g., the mean free path of the neutrino in the solar matter is around 100 light-years. Because neutrinos have a small probability of interaction, and the number of trials of scattering neutrinos is large (proportional to the number of neutrinos times the number of a nucleons), the total neutrino events in a detector should obey a Poisson distribution:

$$P(n; \lambda) = \frac{e^{-\lambda} \lambda^n}{n!}, \quad (3.83)$$

where λ is the mean value of neutrino interactions in a given period, and n is the number of interactions. The λ comes from the neutrino rates (3.10). In an experiment, the number of events is separated into energy bins. Hence the total probability obtained from the \vec{n} events in the detector and distributed over all energy bins is:

$$P(\vec{n}, \vec{\lambda}) = \prod_i P(n_i; \lambda_i). \quad (3.84)$$

From Eq.(3.84), we can create a test statistics that compare the model with its largest probability, that is, when $\lambda_i = n_i$:

$$\chi^2 = -2 \ln \left(\frac{P(\vec{n}, \vec{\lambda})}{P(\vec{n}, \vec{n})} \right) = 2 \sum_i \left(n_i \ln \frac{n_i}{\lambda_i} + \lambda_i - n_i \right), \quad (3.85)$$

where the χ^2 function follows a χ^2 distribution with $N - m$ degrees of freedom [49] (N is the total number of points and m is the number of parameters). As we will be interested in $n_i > 5$, even a normal distribution can be assumed instead of $P(\vec{n}, \lambda)$. In that case, one can use

$$\chi^2 = \sum_i \frac{(n_i - \lambda_i)^2}{\sigma_i^2} \quad (3.86)$$

where Eq. (3.86) obeys a χ^2 distribution with $N - m$ degrees of freedom [50] and σ_i^2 is the standard deviation in the energy bin (which can be estimated from the data). The minimum values of equations (3.85) and (3.86) are equivalent to maximize Eq. (3.84) and can be used to estimate the p -value to measure the goodness-of-fit. In addition, Eqs. (3.85) and (3.86) can also be used to measure the uncertainty of the parameters at a certain C.L.. If one uses:

$$\Delta\chi^2 = \chi^2 - \min(\chi^2), \quad (3.87)$$

it follows a χ^2 distribution with m degrees of freedom, where m is the number of free parameters.

For completeness, we also introduce the *parameter goodness-of-fit*, that also will be used in this work:

$$\chi_{PG}^2 = \sum_j \Delta\chi_j^2, \quad (3.88)$$

where j refers to a given data set (e.g, an experiment) χ_{PG}^2 follows a χ^2 distribution with $m_j - m$ where m_j is the number of parameters in each data-set j and m is the total number of parameters [51].

3.3.2 Reactors

In this section we will introduce the experimental setup and simulations of the reactor experiments KamLand [52], Reno [53], Daya Bay[54], and Double Chooz[2].

Reactor antineutrinos are produced by the fission of nuclear fuel and fragments. The four main components of nuclear fuel are ^{235}U , ^{238}U , ^{239}Pu , and ^{241}Pu . The antineutrino flux from reactors is well known in the literature and peaks around 4 MeV. In the past, the reactor flux was a source of several discussions about sterile neutrinos. Nowadays, it is calculated with good precision and does agree with data [55] with no indication of sterile neutrinos.

The anti- neutrinos produced in reactors can be detected by inverse beta decay, generating a positron event. We calculate the Eqs. (3.12) for reactors based on Eqs. (3.63) (for detection) and (3.73) (for Gamow-Teller production). In the production, the energy dependency should be averaged for processes dependent on the nucleon energy:

$$\langle p_{TL} \rangle = -\frac{g_T}{g_A} m_e \frac{\langle E_e \rangle}{\langle E_e p_e \rangle} = -\frac{g_T}{g_A} \frac{m_e}{f_T(E_\nu)}, \quad (3.89)$$

where p_e is the final lepton energy, which comes from the phase space contribution. The $f_T(E_\nu)$ is defined to include the averaged lepton energy over the nucleon decay modes. It

can be found in the continuum approximation

$$f_T(E_\nu) = \frac{\sum_1^n \omega_i E_e(\Delta_i) p_e(\Delta_i)}{\sum_1^n \omega_i E_e(\Delta_i)} \approx 3.7773 - 0.3805 \frac{E_\nu}{\text{MeV}} + 0.0189 \frac{E_\nu^2}{[\text{MeV}]^2} - 0.0003 \frac{E_\nu^3}{[\text{MeV}]^3}. \quad (3.90)$$

Here, w_i is the weight of the process, and we fit the $f_T(E_\nu)$ using the reactor flux [55] in the continuum approximation to find the values shown above. The factors for reactors are presented in table 3.1.

Table 3.1: Production and detection factors in Eq. (3.12) for reactors antineutrinos. Here E_e is the positron energy, m_e is the electron mass and $f(E_\nu)$ take into account the nuclear fuel and sub-products in the reactor model. For low-energy, the positron energy can be related to the antineutrino electron by the relation $E_e = E_\nu - \Delta_{if}$, where $\Delta_{if} = m_f - m_i$ is the mass difference between the final and initial nucleon.

	scalar	tensor		scalar	tensor
p_{XL}	0	$-\frac{g_T}{g_A} \frac{m_e}{f(E_\nu)}$	p_{XX}	$\frac{g_S^2}{3g_A^2}$	$\frac{g_T^2}{g_A^2}$
d_{XL}	$\frac{g_S g_V}{g_V^2 + 3g_A^2} \frac{m_e}{E_e}$	$\frac{3g_A g_T}{g_V^2 + 3g_A^2} \frac{m_e}{E_e}$	d_{XX}	$\frac{g_S^2}{g_V^2 + 3g_A^2}$	$\frac{3g_T^2}{g_V^2 + 3g_A^2}$

Depending on the distance between the reactor and the detector, the experiment can be sensitive to several squared mass differences. We will divide our study of reactors based on that.

In reactor neutrino experiments as Reno, Daya Bay, and Double Chooz, the Δm_{3i}^2 ($i = 1, 2$) and θ_{13} are the oscillation parameters that have measurable impacts. Because of their average distance of around 1 km, they are called medium baseline experiments (MBL). On the other hand, in reactor experiments as Kamland, the Δm_{21}^2 and θ_{12} are the parameters that matter, it has a length of around 200 km, and it is called a long-baseline experiments (LBL).

Medium Baseline Reactors

Here we describe our simulations of Daya Bay, RENO, and Double Chooz. In our simulation, we used the Globes Fit 1.0 [3], a GLOBES 3.0 based software [56, 57]. We used our modified version of GLOBES Fit 1.0 that includes new interactions. Daya Bay, Double Chooz, and RENO analyses are independent for spectral and total rate in GLOBES fit. As we will see, we take both into account to calculate our χ^2 .

The Daya Bay experiment [54] is made of eight identical antineutrino detectors (AD) distributed over three experimental halls (EH) and six reactors. There are two cores



Figure 3.3: Schematic view of the Daya Bay experiment.

~ 316 m apart from EH1, four cores ~ 505 m from the EH2, and all the six cores ~ 1663 m from the EH3. In the EH1 and EH2, there are two ADs each, and in the EH3, there are four ADs. The precise distances between each reactor and AD as well as the reactor power can be found in tables XIII and XIV of [3] or in [54]. The top view of the Daya Bay experiment is shown in figure 3.3. The Daya Bay data can be divided into three phases:

- In phase 1, there were six ADs working, from AD1 to AD6. They took data during 217 days.
- In phase 2, all the eight ADs were working, and they took data during 1013 days.
- In phase 3, AD1 was removed and they took data during 217 days.

In order to simulate Daya Bay, we should use eq. (3.10) for Daya Bay and calculate the ratio in each detector:

$$R_d^{\text{simul}} = \frac{\sum_{rs} t_d^s P_r^s R_\nu^{\text{simul}}(E_\nu, L_{rd}) / L_{rd}^2}{\sum_{rs} t_d^s P_r^s / L_{rd}^2}, \quad (3.91)$$

where r sums over each reactor and s sums over each phase, t_d^s is the duration of the phase s , and the P_r^s is the power of reactor r in phase s . The L_{rd} is the distances between the reactors and the ADs. As in ref. [3], we assumed a 3-meter spherical target for the ADs and performed a Monte Carlo simulation for these distances. With that configuration, we could reproduce the Daya Bay measurements over the standard oscillation parameters Δm_{ATM}^2 and $\sin^2 \theta_{13}$ as shown in Fig. 3.5. Furthermore, we also reproduced the results

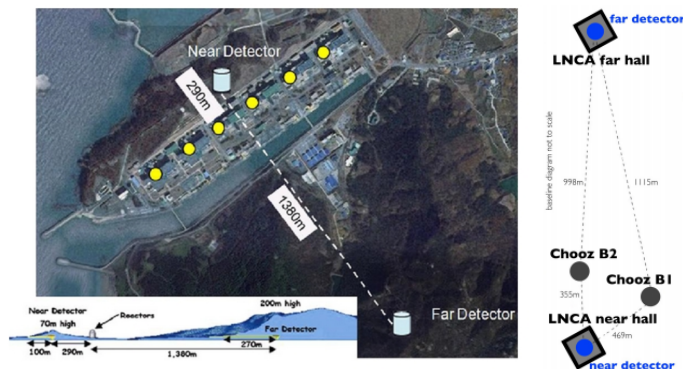


Figure 3.4: The yellow circles represent the reactor's positions in the left schematic view of the RENO [1] experiments. On the right is the schematic view of the Double Chooz experiment [2].

of ref. [3] for the sterile neutrino analysis. More details about the Daya Bay simulation can be found in ref. [3].

The RENO experiment [53, 2] consists of two detectors that detect neutrinos produced in six reactor cores, as can be seen in figure 3.4. The two main distances associated with RENO are 290 m and 1380 m. On the other hand, the Double Chooz experiment is made of two reactors and two detectors in two experimental halls, as can be seen in figure 3.4 extracted from [2]. The Double Chooz experiment is characterized by two effective mean distances, 300 m and 1000 m. Further details can be found in ref. [3]. We assume the detectors are spheres with 3 m of radius. The distances and power of each reactor in each running period can be found in tables XVIII, XIX, and XXIII of ref. [3]. With this information, we can use our modified version of GlobesFit 1.0 and simulate RENO and Double Chooz. From our simulation, we could reproduce the results of ref. [3] that we present in figure 3.5. It is possible to see that the experiment that restricted more the parameters is Daya Bay due to its large statistics.

The GlobesFit assumes averaged baselines for the neutrino oscillation. In Eqs. A.12-A.13 of Ref. [3] it can be seen how to compute the average over the baseline, $F(q)$ function for $\sin^2(qL)$:

$$F(q) = \langle L^2 \rangle \sum_i \frac{w_i \sin^2(qL_i)}{L_i^2}, \quad (3.92)$$

where, w_i is the weight for the average, which is assumed as the power of the plant or a combination with the period of usage (as in Daya Bay). The $\langle L^2 \rangle$ is the weighted average sum. We reproduced their calculations and found the same results. With that, we could also include the average for $\sin(qL)$ (the CP violation term), see eq. (3.17). For the Medium Baseline reactor (MBR) case, we adopt the following χ^2 distribution:

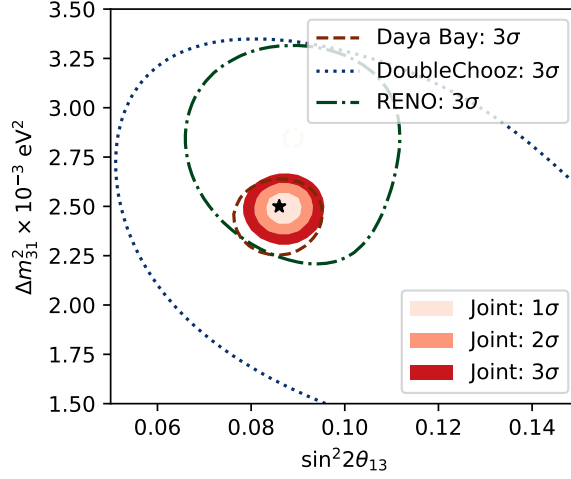


Figure 3.5: We show our results for the confidence level curves at 3σ for Daya Bay (dashed red), DoubleChooz experiment (dotted blue), and RENO experiment (dashed-dotted green). Further, the confidence level curves for a joint analysis of all the three experiments at 1, 2, and 3σ in shades of red.

$$\chi_{\text{MBR}}^2 = \sum_{\text{exp}=\{\text{DB,DC,RENO}\}} (\chi_{\text{exp}}^{\text{shape}})^2 + (\chi_{\text{exp}}^{\text{rate}})^2 + \frac{(1 - \alpha)^2}{\sigma_a^2}, \quad (3.93)$$

where

$$(\chi^2)_{\text{DB}}^{\text{shape}} = \sum_{k=\{\text{EH2,EH3}\}} \sum_{i,j}^{N_{\text{DB}}} (d_i^k - n_i^k)(V_{\text{DB}}^{-1})_{ij}(d_j^k - n_j^k), \quad (3.94)$$

where, d_i^k is the released data in the energy bin i (over $N_{\text{DB}} = 52$ energy bins) for the ratio between the event number in the experimental hall $k = 1, 2, 3$ (EH k) with EH1, n_i^k is the corresponding simulated value. Here, V_{DB} is the covariance matrix for the Daya Bay shape analysis. Finally,

$$(\chi^2)_{\text{DB}}^{\text{rate}} = \sum_{i,j}^{N_{\text{DB}}} (d_{0,i}^k - (1 - \alpha)n_{0,i}^k)(W_{\text{DB}}^{-1})_{ij}(d_{0,j}^k - (1 - \alpha)n_{0,j}^k), \quad (3.95)$$

where the variables have similar meanings as in the shape analysis case, with the difference that $d_{0,i}(n_{0,i})$ (i runs over $N_{\text{DB}} = 8$ bins for different running periods) is the ratio between the total number of events at AD1, AD2, AD8 and AD3 divided by the standard neutrino oscillation prediction case. The parameter α is related to the normalization error, $\sigma_a = 0.025$, that we assume to be fuel independent. For Double Chooz (DC) ($N_{\text{DC}} = 26$ data points in the shape analysis and four data points in the rate) and RENO ($N_{\text{RENO}} = 25$ data points in the shape analysis and eight data points in the rate), we consider the near and far detectors ratio. The χ^2 is the same as in Eqs. (3.94) and (3.95) but d_i^k is

the far/near ratio and $d_{0,i}^k$ are the ratios in the near detector with the standard model prediction.

Long Baseline Experiments

The KamLAND experiment consists of a 1 kton of highly purified liquid scintillator detector in Japan that collects signals of inverse beta decay of neutrinos coming from different reactors in Japan. As the average distance from the reactors and the KamLAND detector is of the order of 180 km, and the neutrino energies are around 3 MeV, the experiment is sensitive to the solar neutrino squared mass difference Δm_{21}^2 . The Kamland reactor distances can be seen in figure 3.6.

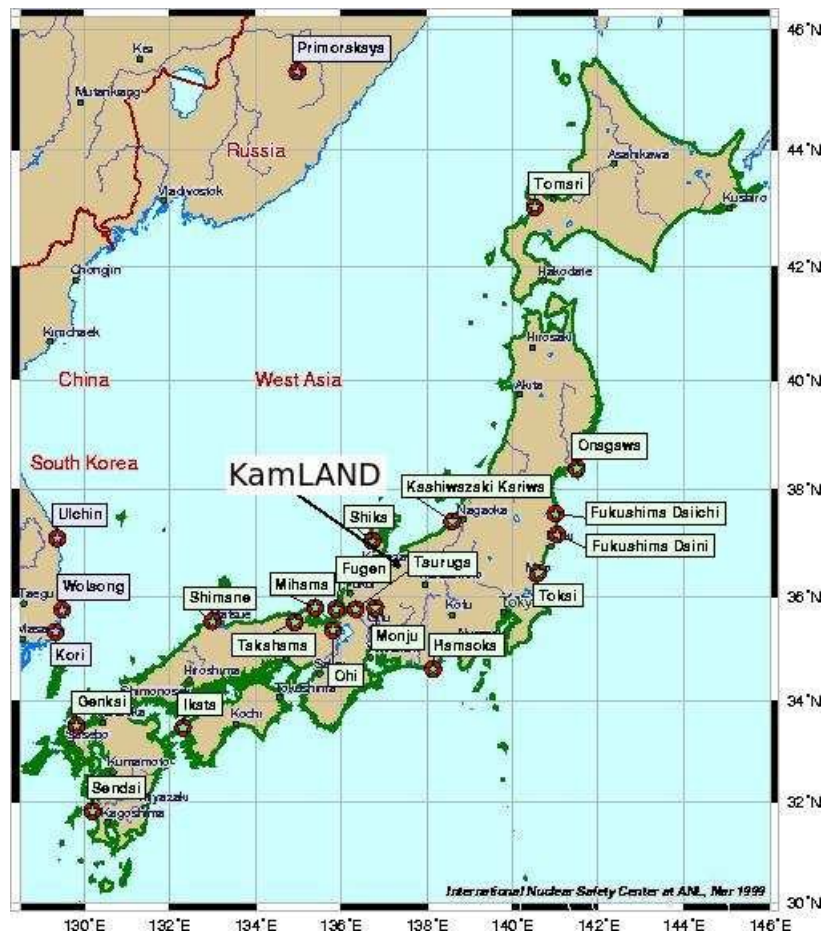


Figure 3.6: Kamland reactors distribution on a map. Taken from <http://www.insc.gov>

The KamLAND detector measures the event rates of antineutrino signals from 2002 to 2007. The experiments had a total exposure of 2.44×10^{32} proton-yr and the energy resolution of $\sim 6.8\%/\sqrt{E_\nu/\text{MeV}}$.

To simulate the KamLAND event rates, we used a reactor predicted flux from

ref. [58, 59] and calculated the total flux in the detector

$$\frac{d\Phi(E_\nu)}{dE_\nu} = \frac{\sum_j F_j \frac{d\phi_\nu^{(j)}(E_\nu)}{dE_\nu}}{4\pi \sum_i W_i L_i^2}, \quad (3.96)$$

where F_j are the fuel fractions of the reactor given by the KamLand collaboration (0.567 : 0.078 : 0.298 : 0.057) for (^{235}U : ^{238}U : ^{239}Pu : ^{241}Pu). The neutrino flux comes from [55] and the baseline L_i and power W_i for each reactor comes from [60]. The efficiencies are given by ϵ_i and extracted from [52]. The antineutrino cross-section comes from [61] and the neutrino reconstruction function was taken from Ref. [62] using a $6.4\% \sqrt{E_\nu/\text{MeV}}$ error given by [52].

Using the total flux at the detector made it possible to calculate the event rates:

$$n_i \propto \epsilon_i \int_{E_i^{\min}}^{E_j^{\max}} dE_e \int_{E_{\text{th}}}^{\infty} dE_\nu \left(\sum_j W_j \left(\frac{R_{\bar{\nu}_e \bar{\nu}_e}}{\phi_e^{\text{SM}} \sigma_e^{\text{SM}}} \right)_{(E_\nu, L_j)} \right) \frac{d\Phi(E_\nu)}{dE_\nu} \frac{d\sigma(E_\nu, E_e)}{dE_e} R(E_\nu, E_e), \quad (3.97)$$

where ϵ_i is the post-smearing efficiency for each energy beam, $\sigma_{det}(E)$ is the inverse beta-decay cross-section, $P(\bar{\nu}_e \rightarrow \bar{\nu}_e)$ is the neutrino oscillation probability and $R(E, E')$ is a Gaussian energy resolution function

$$R(E, E') = \frac{1}{\sigma(E)\sqrt{2\pi}} e^{-\frac{(E-E')^2}{2\sigma^2(E)}}, \quad (3.98)$$

where $\sigma(E)$ function for inverse beta decay is defined in GLOBES 3.1 manual, page 104. The data and the predicted background were collected from ref. [52]. Using eq. (3.10), we could reproduce the confidence level curves⁴ for the standard oscillation parameters in figure 4 of ref. [52].

For the statistical analysis of KamLand (KL), we calculate the following χ^2 :

$$\chi_{\text{KL}}^2 = \sum_i \frac{\left(d_i - n_i(a_1, a_2) - b_i(a_3, a_4) \right)^2}{d_i} + \sum_i \frac{a_i^2}{\sigma_i^2} \quad (3.99)$$

where d_i is the data extracted by summing the number of events of the three KamLand phases of Ref. [52], b_i is the background also extracted from Ref. [52], and σ_i are the systematic errors. We used $\sigma_1 = 0.05$ (signal normalization error), $\sigma_2 = 0.02$ (signal energy error), $\sigma_3 = 0.08$ (background normalization error) and $\sigma_4 = 0.02$ (background

⁴We used the ordinary χ^2 test.

energy error). Also, the number of events given the calibration and normalization errors will be the same as in the Ref. [57]:

$$n_i(a, b) = (1 + b)(1 + a) [(n_{i+1} - n_i)(\delta(b) - i) + n_i]. \quad (3.100)$$

Here, $\delta(b) = b(i + t_0 + 0.5) + i$ where $t_0 = N_{\text{bins}} E_{\text{min}} / (E_{\text{max}} - E_{\text{min}})$. For each χ_{KL}^2 , we minimize over the nuisance parameters a_i .

3.3.3 Solar neutrino experiments

In addition to reactor experiments, solar neutrino experiments are essential to measuring neutrino oscillation parameters, the θ_{12} and Δm_{21}^2 . In our context, solar experiments can give light to new constraints in our new physics analysis. For example, non-standard neutrino interactions can appear in the beta process in the sun and in inverse beta detection of the neutrino coming from the sun. The processes for neutrino production in the sun are:

$$(pp) \quad p + p \rightarrow d + e^+ + \nu_e, \quad (3.101)$$

$$(pep) \quad p + e^- + p \rightarrow d + \nu_e, \quad (3.102)$$

$$(hep) \quad {}^3\text{He} + p \rightarrow {}^4\text{He} + e^+ \nu_e, \quad (3.103)$$

$$({}^7\text{Be}) \quad e^- + {}^7\text{Be} \rightarrow {}^7\text{Li} + \nu_e, \quad (3.104)$$

$$({}^8\text{B}) \quad {}^8\text{B} \rightarrow {}^8\text{Be} + e^+ + \nu_e, \quad (3.105)$$

$$({}^{13}\text{N}) \quad {}^{13}\text{N} \rightarrow {}^{13}\text{C} + e^+ + \nu_e, \quad (3.106)$$

$$({}^{15}\text{O}) \quad {}^{15}\text{O} \rightarrow {}^{15}\text{N} + e^+ + \nu_e, \quad (3.107)$$

$$({}^{17}\text{F}) \quad {}^{17}\text{F} \rightarrow {}^{17}\text{O} + e^+ + \nu_e, \quad (3.108)$$

in which (3.105), (3.106), (3.107) and (3.108) are β decays. For solar neutrinos, we consider that non-standard interactions are present in beta decay processes which are mainly of Gamow-Teller type. The interaction factors are presented in table 3.2.

	scalar	tensor		scalar	tensor
p_{XL}	0	$+\frac{g_T}{g_A} \frac{m_e}{E_e}$	p_{XX}	$\frac{g_S^2}{3g_A^2}$	$\frac{g_T^2}{g_A^2}$
d_{XL}	$-\frac{g_S g_V}{g_V^2 + 3g_A^2} \frac{m_e}{E_e}$	$\frac{3g_A g_T}{g_V^2 + 3g_A^2} \frac{m_e}{E_e}$	d_{XX}	$\frac{g_S^2}{g_V^2 + 3g_A^2}$	$\frac{3g_T^2}{g_V^2 + 3g_A^2}$

Table 3.2: The same as Table 3.1 but now for production and detection factors for solar neutrinos.

The flux for each of these processes depends on the distance from the center of the core and on the neutrino energy. We obtain the fluxes from Ref. [63]. We consider the following experiments in our analysis:

- the full spectral data from Super-Kamiokande phases I, III and IV [64, 65, 66];
- the combined analysis of all three SNO phases [67];
- Borexino results [68];
- combined Gallex+GNO [69];
- SAGE [70] data;
- Homestake results [71].

For each of these experiments we calculate the number of events for the ratio considered:

$$n_{ij}^{\text{exp}} = \int_{E_i^{\text{min}}}^{E_i^{\text{max}}} dE_e \int_{E_{\text{rmin}}}^{\infty} dE_\nu \int_0^{R_{\text{sun}}} dL \frac{d\phi_j(L, E_\nu)}{dE_\nu} \left(\frac{R_{\nu_e\nu_e}}{\phi^{\text{SM}}\sigma^{\text{SM}}} \right) \frac{d\sigma(E_\nu, E_e)}{dE_e} dE_\nu, \quad (3.109)$$

where n_i^{exp} is the number of events for the bin i from the flux j for each experiment exp. The $\phi_j(L, E_\nu)$ is the flux for a given production process, σ_{exp} is the cross-section for the experiment i . In our ratios, the factors dependence $E_e = E_\nu - \Delta_{if}$, where $\Delta_{if} = m_f - m_i$ is the mass difference between the final and initial nucleon was implemented using:

$$\begin{aligned} {}^{71}\text{Ga} \rightarrow {}^{71}\text{Ge} : \quad E_e &= E_\nu + 0.2785 \text{ MeV}, \\ {}^{37}\text{Cl} \rightarrow {}^{37}\text{Ar} : \quad E_e &= E_\nu - 0.303 \text{ MeV}. \end{aligned} \quad (3.110)$$

The number of events was calculated for each energy bin. For statistics, we used Eq. (3.86) with the difference that the correlation between neutrino experiments was included to take into account the flux uncertainties from astrophysical parameters, see Ref. [72]. Each flux component has its astrophysical uncertainty. They affect mainly Gallex/GNO, SAGE, and Homestake (GSH). We sum all the components and define the covariance matrix between these experiments as:

$$(V_{\text{GSH}})_{kl} = (\sigma_{\text{sys}}^2)_k \delta_{kl} + (\sigma_{\text{stat}}^2)_k \delta_{kl} + \sum_{ij} n_{il} n_j^{\text{exp}} (\sigma_{\text{astro}})_i * (\sigma_{\text{astro}})_j (\rho_{\text{astro}})_{ij} \quad (3.111)$$

where k and l run over experiments and i, j run over the flux component. The χ_{GSH}^2 function for Gallex/GNO, Sage, and Homestake will be

$$\chi_{\text{GSH}}^2 = \sum_{kl} (n_k^{\text{exp}} - d_k^{\text{exp}}) (V_{\text{GSH}}^{-1})_{kl} (n_l^{\text{exp}} - d_l^{\text{exp}}). \quad (3.112)$$

For the Borexino experiment, there is a correlation between the energy bins, driven by systematic errors:

$$(V_B)_{ij} = [(\sigma_{\text{sys}})_i(\sigma_{\text{sys}})_j + \sigma_{\text{fid}}^2] n_i^{\text{borexino}} n_j^{\text{borexino}} + (\sigma_{\text{stat}}^2)_i \delta_{ij} \quad (3.113)$$

where $(\sigma_{\text{sys}})_i$ is the systematic error of the i th bin, $\sigma_{\text{fid}} = 0.038$ is the error in the fiducial volume and $(\sigma_{\text{stat}})_i = n_i + b_i + 1$ is the statistical error including the background. The χ_B^2 function for Borexino will be:

$$\chi_B^2 = \sum_{ij} (n_i + b_i - d_i)(V_B^{-1})_{kl}(n_j + b_j - d_j). \quad (3.114)$$

where n_i are the events given by Eq. (3.109) summed over all flux components, b_i is the background and d_i are the data points. For Super-Kamiokande the calculation is very similar to the Borexino case, with the difference that the fiducial uncertainty is already included in the systematic error:

$$\chi_{\text{SK}}^2 = \sum_{\text{all phases}} \chi_{\text{phase}}^2. \quad (3.115)$$

In the same way, for the SNO experiment χ_{SNO}^2 is calculated including the systematics and statistical errors, and the final result for solar experiments will be given by:

$$\chi_{\text{sun}}^2 = \min_{\text{boron flux}} (\chi_{\text{GSH}}^2 + \chi_B^2 + \chi_{\text{SK}}^2 + \chi_{\text{SNO}}^2) \quad (3.116)$$

where we let a free boron flux parameter for all experiments, and we marginalize over it to find the χ_{sun}^2 .

3.4 Results and Conclusions

This section presents the results of the simulations given on sec. 3.3. We separate our analysis in four groups by flavor and type of interaction, and the section will follow: $[\tilde{\epsilon}_S]_{e\tau}$, $[\tilde{\epsilon}_T]_{e\tau}$, $[\tilde{\epsilon}_S]_{e\mu}$, and $[\tilde{\epsilon}_T]_{e\mu}$. We study each case separately and compare the result at the end. We simulate each experimental set (MBL reactors, LBL reactors, and solar experiments) as given in section 3.3. We vary over all the combinations of parameters in a grid search way. The Fig. 3.7 shows which parameters were set free and were considered in each simulation. If a parameter can be sensitive in a set of experiments, it will be linked by a solid line. If the sensitivity is weak, it receives a dashed line link. Colored lines mean that the sensitivity only exists if there is new physics.

We perform a grid calculation of the predicted number of events for each experimental set and then calculate the correspondent χ^2 function. For each experimental

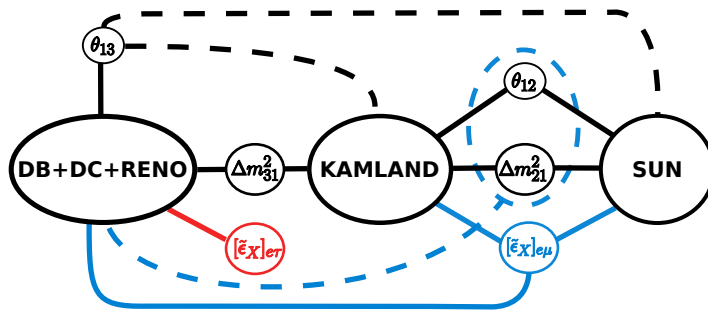


Figure 3.7: Connection of parameter sensitivity to experimental set. Solid line represents strong sensitivity, the dashed line represents weak sensitivity. Colored lines mean that the parameter is active only if new physics is present.

case, the resultant χ^2 was stored in a large table and then interpolated to create a table that sums the χ^2 of all the experiments.

Regarding the type of interaction, the difference between scalar and tensor interactions comes from calculating the p 's and d 's. For most of the p 's (and d 's), the ratio between scalar and tensor interactions is $3g_T/g_S \approx 1/3$, meaning that scalar interactions are mostly $1/3$ in size of the tensor interactions. For example, it can be seen from the two rightmost panels of Fig. 3.8, where the tensor interactions in green is approximately are $1/3$ in size compared to scalar interaction in yellow.

For comparison, before presenting the results for non-standard interactions, let us see what to expect in the case of the standard model. In the standard model, the MBL reactors are experiments with the baseline of hundreds of meters and 5 MeV neutrino energies. As a consequence, it is sensitive to the Δm_{31}^2 and θ_{13} parameters. The θ_{13} was first measured and had its precision associated with the MBL experiments (mainly Daya Bay). The minimum χ^2 found for MBL in the standard neutrino oscillation was 87 with $114 - 2$ dof, as $\chi^2/\text{dof} < 1$, the simulated scenario agrees with the data. For the Kamland experiment, the minimum χ^2 obtained was 15 with $17 - 2$ dof, also in agreement with the data. The Kamland experiment was sensitive to Δm_{21}^2 and θ_{12} . In the same direction of the Kamland experiment are the solar neutrinos, where we found a minimum χ^2 of 134 and $149 - 2$ dof. Solar experiments are sensitive to Δm_{21}^2 and θ_{12} . Both Kamland and solar neutrinos can be sensitive to θ_{13} . However, they can not see a non-zero effect of its value. In addition, those experiments are complementary to each other Kamland is more sensitive to Δm_{21}^2 , and solar experiments are more sensitive to θ_{12} .

In the global analysis of the standard model, where we sum the χ^2 of all the experiments, the minimum value was 247.7 with $280 - 4$ dof. In addition, the parameter goodness-of-fit leads to a p -value of 15%, with no significance to exclude the neutrino

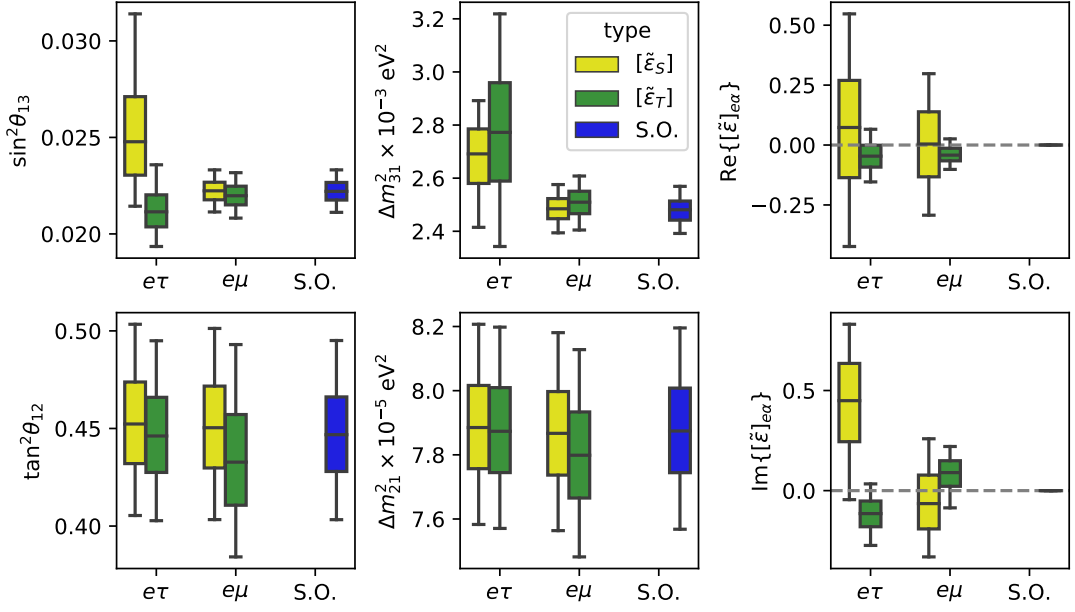


Figure 3.8: In this figure, we present the Monte Carlo simulated results of the $\Delta\chi^2$. We show the boxplot for each distribution. In green we present the limits when tensor interactions are present, in yellow for scalar interactions and in blue for standard neutrino oscillation.

oscillation hypothesis. The resultant limits on the parameters from our analysis for standard oscillations can be seen in figure 3.8 in blue. The whiskers were set at the 5% and 95% percentiles, approximately the 90% C.L. region. To generate figure 3.8, we perform a Monte Carlo sampling. The result is in total agreement with our grid results.

Before going into the details of each case, we present a summary of the statistics:

- Scalar $[\tilde{\epsilon}_S]_{e\tau}$: we found a $(\chi^2_{\text{Global}})_{\text{min}} - ((\chi^2_{\text{Global}})_{\text{SO}})_{\text{min}} = 2.99$ that corresponds to a 1.73σ with preference for non-zero NSI. The parameter goodness-of-fit has the p -values of 29%;
- Scalar $[\tilde{\epsilon}_S]_{e\mu}$: we found $(\chi^2_{\text{Global}})_{\text{min}} - ((\chi^2_{\text{Global}})_{\text{SO}})_{\text{min}} = 2.40$ with a 1.55σ preference for non-zero NSI and the p -values of 38%;
- Tensor $[\tilde{\epsilon}_T]_{e\tau}$: we found $(\chi^2_{\text{Global}})_{\text{min}} - ((\chi^2_{\text{Global}})_{\text{SO}})_{\text{min}} = 1.99$ with a 1.41σ preference for non-zero NSI and the p -value of 26%;
- Tensor $[\tilde{\epsilon}_T]_{e\mu}$: we found $(\chi^2_{\text{Global}})_{\text{min}} - ((\chi^2_{\text{Global}})_{\text{SO}})_{\text{min}} = 2.89$ with a 1.70σ preference for non-zero NSI and the p -values of 29%.

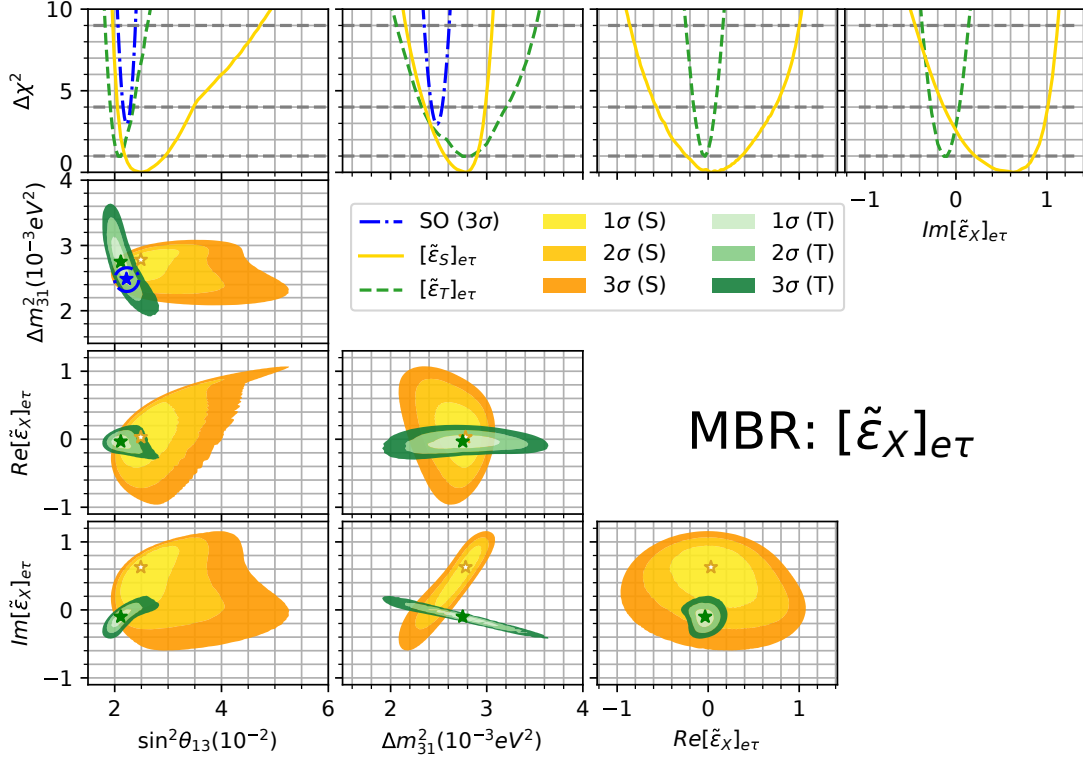


Figure 3.9: In the first line, the panels are the 1D $\chi^2 - \chi_T^2$ functions where the minimum value we put the smallest among the minimum χ^2 of the three cases, in this case, was the tensor. In dashed green, we show the tensor interactions case, in plain yellow, the scalar and the standard neutrino oscillation in dash-dotted blue. In the panels below, we show a grid with six 2D panels for all combinations of parameters simulated. In green, we show the tensor, in yellow, the scalar, and in blue, the standard neutrino oscillation. The contours were set to 1, 2, and 3 σ .

3.4.1 The $[\tilde{\epsilon}_X]_{e\tau}$

In our analysis, the $[\tilde{\epsilon}_X]_{e\tau}$ have strong effects in MBR experiments, see Fig. 3.9. This figure remains unchanged if we include Kamland and solar experiments, also representing the global analysis. In MRB experiments, we perform a grid calculation of the χ^2 considering the $\sin^2 \theta_{13}$, Δm_{31}^2 , $\text{Re}\{[\tilde{\epsilon}_S]_{e\tau}\}$ and $\text{Im}\{[\tilde{\epsilon}_S]_{e\tau}\}$.

The 2D and 1D contours of the χ^2 are shown in figure 3.9, where in the first line we show the 1D curve of the $\Delta\chi^2 = \chi^2 - \min\chi_S^2$ marginalized over all the other parameters ($\min\chi_S^2$ is the minimum value of the χ^2 for scalar interactions). In blue is the result for the standard neutrino oscillation, in yellow are those for scalar interactions and in green are those for tensor interactions. In the panels below, we show a facet grid with the 2D contours of $\Delta\chi^2 = \chi^2 - \min\chi_X^2$ marginalized on the not shown parameters ($\min\chi_X^2$ is the correspondent minimum χ^2).

In figure 9, we can see that the main effect of $[\tilde{\epsilon}_S]_{e\tau}$ on MBR experiments is to increase the value of the allowed θ_{13} . This is an effect that is mainly due to $\text{Re}\{[\tilde{\epsilon}_S]_{e\tau}\}$.

In addition, there is a correlation between the $\text{Im}\{[\tilde{\epsilon}_S]_{e\tau}\}$ and Δm_{31}^2 , where the non-zero $\text{Im}\{[\tilde{\epsilon}_S]_{e\tau}\}$ allows new regions of Δm_{31}^2 . For tensor interactions, the value of θ_{13} is not subjected to large changes as in the scalar case. On the other hand, the Δm_{31}^2 is negatively correlated with the $\text{Im}\{[\tilde{\epsilon}_T]_{e\tau}\}$. We enter in more details in the discussion below:

- For scalar $[\tilde{\epsilon}_S]_{e\tau}$ interactions, the standard neutrino oscillation is disfavored at 1.7σ . In the $\Delta m_{31}^2 \times \text{Re}[\tilde{\epsilon}_S]_{e\tau}$ panel of figure 3.9, we notice a positive correlation between Δm_{31}^2 and the imaginary part of $[\tilde{\epsilon}_S]_{e\tau}$. This correlation drives the improvement in the fit leading to a large $\Delta m_{31}^2 = 2.78 \times 10^{-3} \text{ eV}^2$ and a non-zero $\text{Im}[\tilde{\epsilon}_S]_{e\tau} = +0.62$. The analysis also leads to a 3σ allowed region of $\sin^2 \theta_{13} \approx 0.05$ due to a correlation of the $\sin^2 \theta_{13}$ with the $\text{Re}[\tilde{\epsilon}_S]_{e\tau}$, as can be seen in the $\sin^2 \theta_{13} \times \text{Re}[\tilde{\epsilon}_S]_{e\tau}$ panel. The range of the parameters can be obtained by $\Delta\chi^2 = 1$ in Fig. 3.9. The values of the real and imaginary parts found for scalar interactions $[\tilde{\epsilon}_S]_{e\tau}$ are (shown graphically in the right panel of figure (3.8) by the yellow box) and are equal to

$$\text{Re}[\tilde{\epsilon}_S]_{e\tau} = +0.03_{-0.21}^{+0.40}, \quad \text{Im}[\tilde{\epsilon}_S]_{e\tau} = +0.62_{-0.41}^{+0.23}. \quad (3.117)$$

- In the tensor interaction case, the standard neutrino oscillation is disfavored with a 1.41σ statistical significance, see figure 3.9. As in the scalar case, the preference was guided by the $\text{Im}[\tilde{\epsilon}_T]_{e\tau}$ that is negatively correlated with Δm_{31}^2 also leading to a larger value of $\Delta m_{31}^2 = 2.75 \times 10^{-3} \text{ eV}^2$. Now the imaginary part is negative $\text{Im}[\tilde{\epsilon}_T]_{e\tau} = -0.12$. This comes from the fact that the interference term in the production see Table. (3.1), is negative for tensor interactions and positive for scalar interactions. At 3σ in the tensor case the Δm_{31}^2 can reach values of $3.6 \times 10^{-3} \text{ eV}^2$ and $\sin^2 \theta_{13} = 0.027$ upper limit at 3σ . In the tensor case, the θ_{13} is also correlated with $\text{Im}[\tilde{\epsilon}_T]_{e\tau}$ as can be seen in the $\theta_{13} \times \text{Im}[\tilde{\epsilon}_T]_{e\tau}$ panel of figure (3.9). The values of the real and imaginary parts of the NSI parameter are (shown graphically in the right panel of figure (3.8) by the green box):

$$\text{Re}[\tilde{\epsilon}_T]_{e\tau} = -0.03_{-0.06}^{+0.06}, \quad \text{Im}[\tilde{\epsilon}_T]_{e\tau} = -0.12_{-0.10}^{+0.08}. \quad (3.118)$$

For the mixing parameters and the squared mass difference, we show in left and central panel of figure (3.8) the range of $\sin^2 \theta_{13}$, $\tan^2 \theta_{12}$, Δm_{31}^2 and Δm_{21}^2 . Visually, we can notice that $\sin^2 \theta_{13}$ and Δm_{31}^2 changed compared with the usual neutrino oscillation scenario.

3.4.2 The $[\tilde{\epsilon}_X]_{e\mu}$

From the analysis of our formulas discussed in section 3.2.1, the $[\tilde{\epsilon}_X]_{e\mu}$ parameter was expected to have significant effects on the solar scale for solar experiments and KamLand. This happens because parameters always appear together with the Δm_{21}^2 mass squared difference. However, our analysis of MBR experiments also plays an important role. It comes from the fact that the CP violation term of solar scalar can be sensitive at the MBR experiments.

Here, we first present the results of MBR experiments, followed by KamLand+Solar experiments, and in the end, the global analysis. Our analysis will be based on the χ^2 curve. For MBR, it will depend on:

$$\chi_{\text{MBR}}^2 = \chi^2(\theta_{13}, \Delta m_{31}^2, \theta_{12}, \text{Re}[\tilde{\epsilon}_X]_{e\mu}, \text{Im}[\tilde{\epsilon}_X]_{e\mu}), \quad (3.119)$$

in fact, it also depends on Δm_{21}^2 ; however, we fixed it at the best-fit point of solar and KamLand experiments ($7.8 \times 10^{-5} \text{eV}^2$). We show the 1D and 2D contours of the χ^2 function in figure 3.10. In contrast with figure 3.9, in this analysis, the standard neutrino oscillation parameters are weakly affected by the new interactions. However, the fit is better than Standard Oscillation by 2σ . The improvement in the fit comes mainly from the non-zero CP violation effect from the solar scale. We check that the improvement comes from the normalization of the flux and on the improvement in the fit for the first point of Daya Bay, the result is shown in figure 3.11.

Before combining all in a global analysis, we also perform the Solar+KamLand analysis. The χ^2 function for those experiments, depends on θ_{13} , θ_{12} , Δm_{21}^2 and $[\tilde{\epsilon}_X]_{e\mu}$, we show the 1D and 2D contours at figure 3.12. In the first line, we show the χ^2 functions in the same way as in the previous section. In green, we show the tensor, in yellow the scalar interactions, and in blue the standard neutrino oscillation. There are no important differences for the scalar interactions compared with the standard neutrino oscillation. However, we found a 1.3σ improvement in the fit for the tensor case compared to the standard neutrino oscillation model. This result is compatible with the MBR experiment, as we will see. Also, in figure 3.12 we show the 2D contour. From the 2D contours, we can infer correlations between parameters. For each pair of variables, we minimize the complementary parameter space. In the bullet points below, we discuss the scalar and tensor interactions separated:

- If the $[\tilde{\epsilon}_S]_{e\mu}$ interaction is present, we found no improvement in the fit compared to the standard neutrino oscillation. We found only a tiny distortion in the θ_{13} that can be considered negligible. The limits on the parameters are:

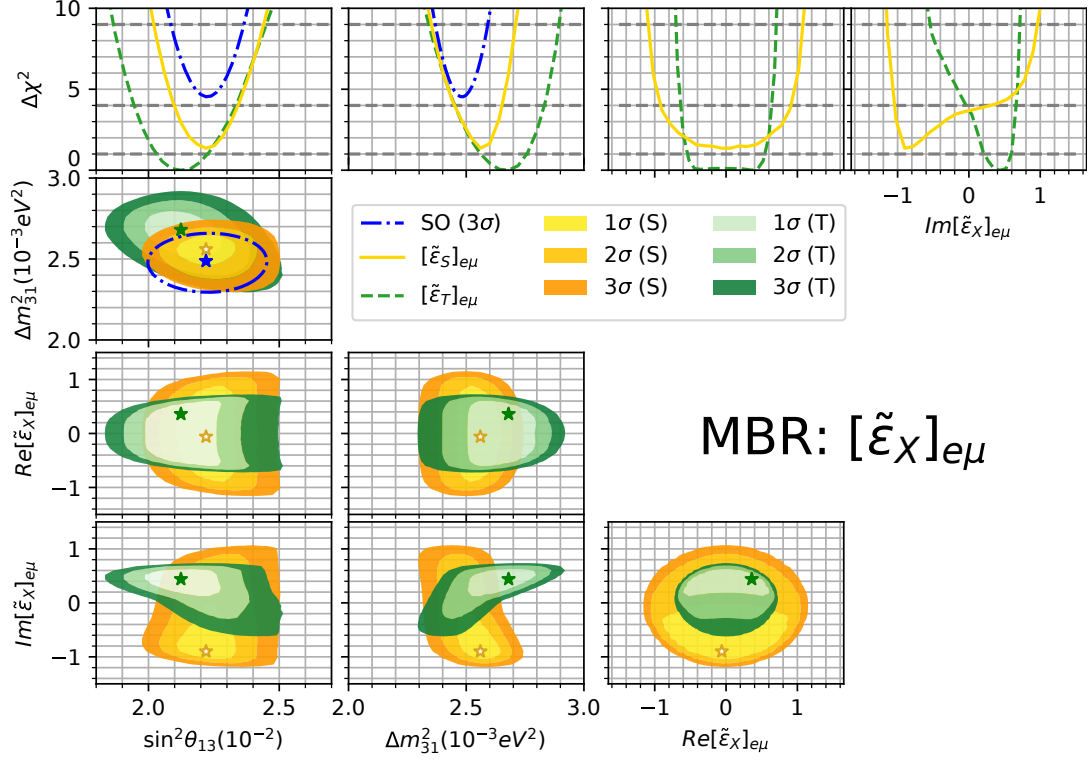


Figure 3.10: The same as in figure 3.9 but for $[\tilde{\epsilon}_X]_{e\mu}$.

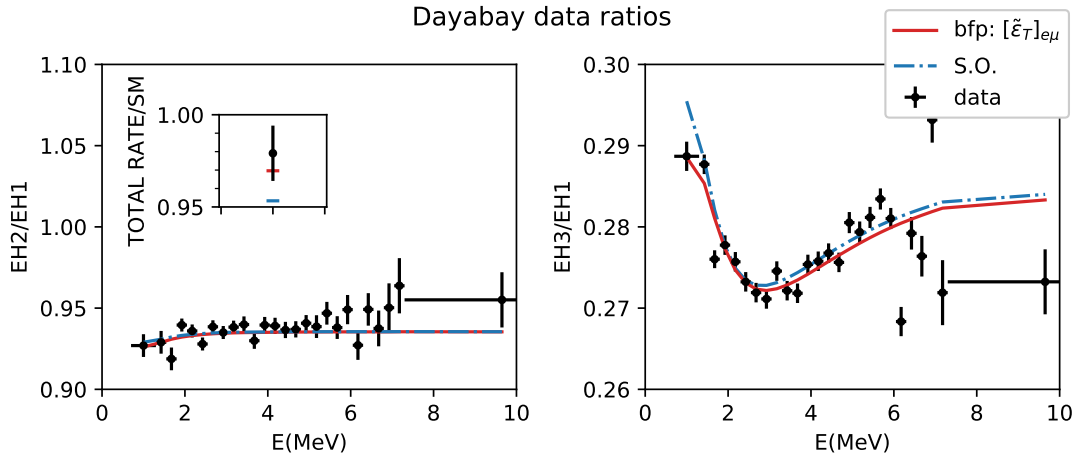


Figure 3.11: Events of Daya Bay experiment, in black we show the data points, in blue the standard oscillation and in red the tensor $e\mu$ interaction. In the left panel, we show the EH2/EH1 ratio and the EH3/EH1 ratios in the right panel. The small panel inside the left panel shows the total rate results compared with the standard model. Here, the x-axis is the neutrino energy $E = E_\nu$. We use the data as presented in [3]

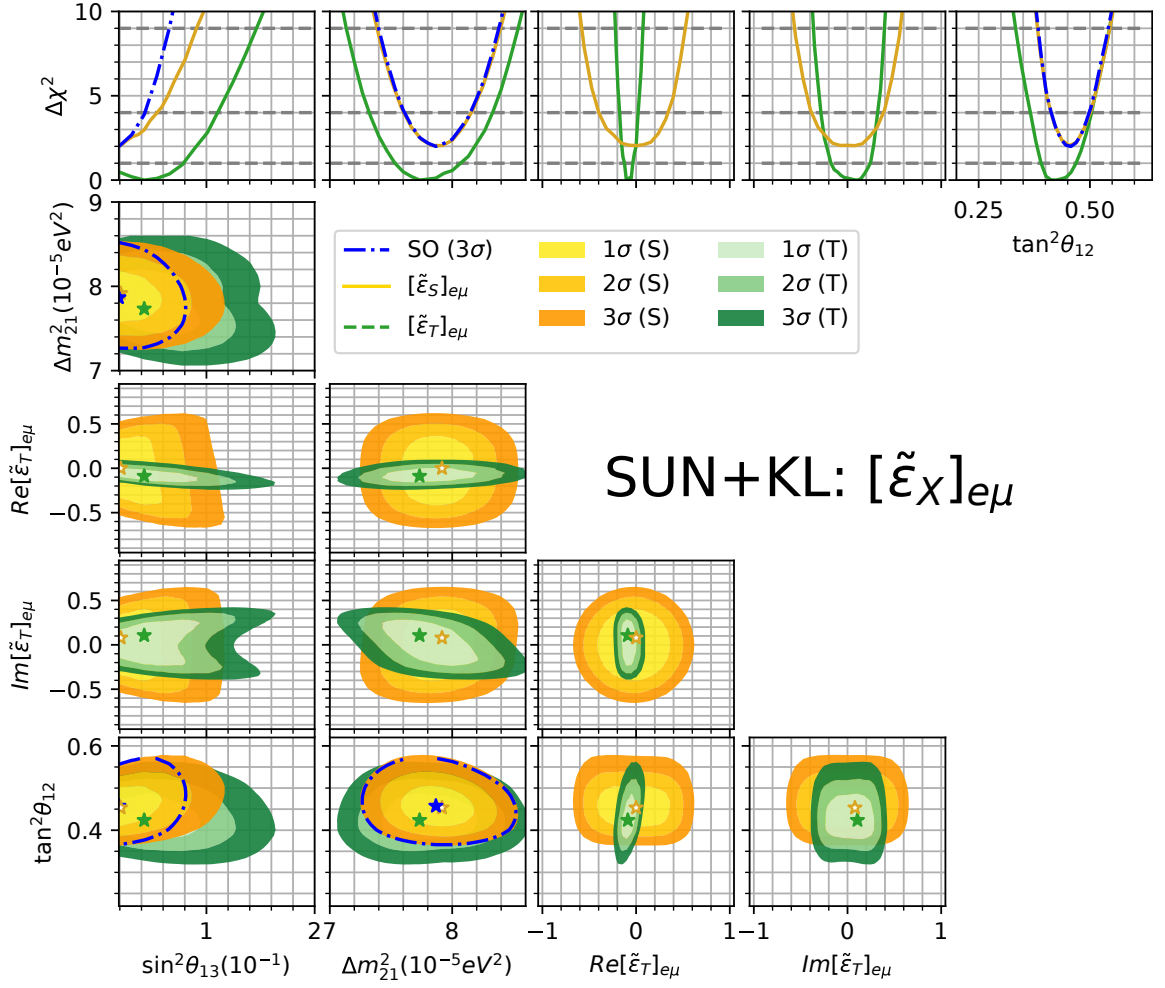


Figure 3.12: The same as in fig 3.9 but for solar neutrinos and $[\tilde{\epsilon}_X]_{e\mu}$ interactions

$$\text{Re}[\tilde{\epsilon}_S]_{e\mu} = 0.00_{-0.30}^{+0.27}, \quad \text{Im}[\tilde{\epsilon}_S]_{e\mu} = +0.01_{-0.29}^{+0.29}. \quad (3.120)$$

- In the case $[\tilde{\epsilon}_T]_{e\mu}$ interaction is present, we found a 1.3σ improvement in the fit compared to the standard neutrino oscillation. The improvement comes from a non-zero $\text{Re}[\tilde{\epsilon}_T]_{e\mu}$ and the limits on the NSI parameters are:

$$\text{Re}[\tilde{\epsilon}_T]_{e\mu} = -0.09_{-0.03}^{+0.05}, \quad \text{Im}[\tilde{\epsilon}_T]_{e\mu} = +0.10_{-0.09}^{+0.14}. \quad (3.121)$$

We found that MBR points to a non-zero CP-violation NSI and Solar+Kamland go in the same direction. We perform a global analysis, using the global χ^2 defined in sec. 3.3. We show the result in figure 3.13. As was expected, the fit improvement remains, now with 1.7σ for non-zero $\text{Im}[\tilde{\epsilon}_T]_{e\mu}$. We summarize the results of figure 3.13 bellow:

- If $[\tilde{\epsilon}_S]_{e\mu}$ interactions are present, there are large changes in the statistical analysis compared to the Standard Model. The $[\tilde{\epsilon}_S]_{e\mu}$ parameter is strongly constrained by

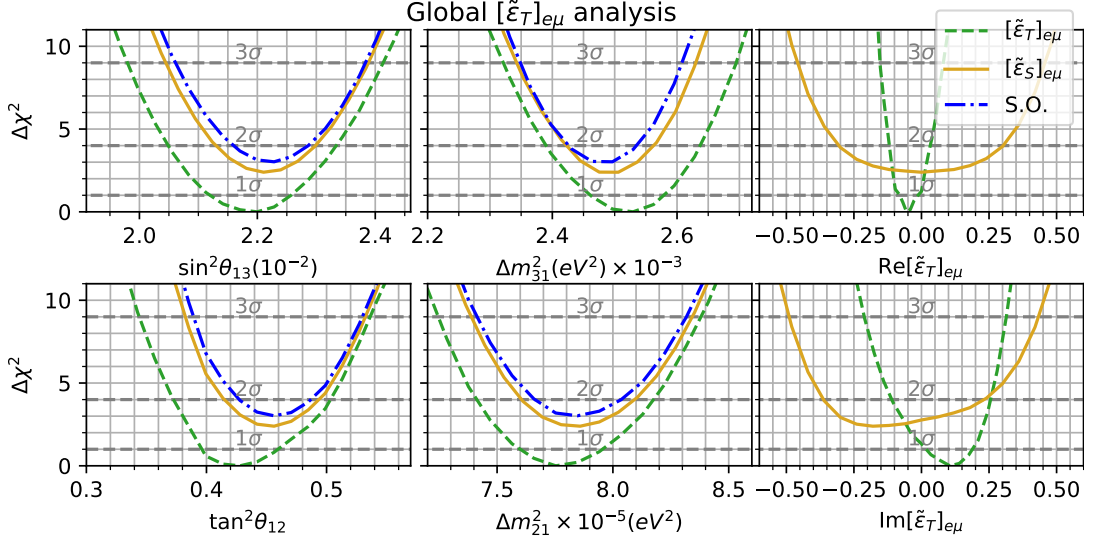


Figure 3.13: The same as the first line of figure 3.9 but for the global analysis of the $[\tilde{\epsilon}_T]_{e\mu}$ parameter.

solar data. In the global analysis, the limits on the NSI parameters are:

$$\text{Re}[\tilde{\epsilon}_S]_{e\mu} = 0.00 \pm 0.25, \quad \text{Im}[\tilde{\epsilon}_S]_{e\mu} = -0.16^{+0.31}_{-0.09}. \quad (3.122)$$

Those are the first limits ever made on these parameters.

- If tensor $[\tilde{\epsilon}_T]_{e\mu}$ interactions are present, for the KamLand+Solar analysis, there is an improvement of 1.3σ in the fit compared with the Standard Model. In the MBR analysis, the significance is 2.1σ guided by a CP violation term from the solar scale. In the global analysis case, the improvement has a 1.7σ significance compared to the standard neutrino oscillation scenario. The tensor $[\tilde{\epsilon}_T]_{e\mu}$ interaction presence can improve the fit of each experiment individually and when they are combined. The global analysis results are presented in the green lines of figure 3.13 and the values of the NSI parameters are:

$$\text{Re}[\tilde{\epsilon}_T]_{e\mu} = -0.05^{+0.04}_{-0.03}, \quad \text{Im}[\tilde{\epsilon}_T]_{e\mu} = -0.13^{+0.09}_{-0.07}. \quad (3.123)$$

3.4.3 CP-violation

From Eqs. (3.125), (3.124), we conclude that for CP violating term, the KamLand [52] can have effects of $\text{Im}[\tilde{\epsilon}_X]_{e\mu}$ and the medium baseline reactors to the $\text{Im}[\tilde{\epsilon}_X]_{e\beta}$ ($\beta = \mu, \tau$). We can compute the equivalent of the Jaroskog invariant in the context of

BSM physics. From Eq. (3.125) and Eq. (3.124) we found that

$$J_{e\mu}^{\text{CP}} = \text{Im}\{[\tilde{\epsilon}_X]_{e\mu}\}c_{13}^3s_{2\theta_{12}}, \quad (3.124)$$

$$J_{e\tau}^{\text{CP}} = \text{Im}\{[\tilde{\epsilon}_X]_{e\tau}\}s_{2\theta_{13}}. \quad (3.125)$$

In the standard neutrino oscillation, when the initial and final neutrino states are equal, there is no effect of CP violation. Then, if there is any evidence of $J_{e\alpha}^{\text{CP}} \neq 0$ ($\alpha = \mu, \tau$) it will be signaling new physics.

The CP violation phase appears in the expressions of both reactors and solar experiments. However, the CP violation effect by itself appears only at reactors, see Eqs. (3.124) and (3.125). We quantify the effects of the CP violation terms, and the $\Delta\chi^2$ functions are presented in figure 3.14. In the left panel, we include the $\Delta\chi^2$ for the $e\mu$ interactions and the right panel for the $e\tau$. In the green curve, we show the tensor interactions in which we notice that the CP constrained is stronger than the scalar, dashed-dotted yellow. We found two scenarios, $[\tilde{\epsilon}_T]_{e\mu}$ and $[\tilde{\epsilon}_S]_{e\tau}$, in which the preference for non-zero CP violation is higher than 1σ . For the tensor, $[\tilde{\epsilon}_T]_{e\tau}$ interactions, the constraint is the restrictive. On the other hand, for the $[\tilde{\epsilon}_S]_{e\mu}$, the bounds are relaxed.

We check that the first data point of the energy spectrum of Daya Bay was responsible for the improvement in the analysis. The significance of the effect is low, only 1σ , and can be only a statistical fluctuation. We consider that more experimental data is needed to support a non-statistical fluctuation interpretation. One experiment that could test such effect which much more statistics, can be the future designed JUNO experiment [73].

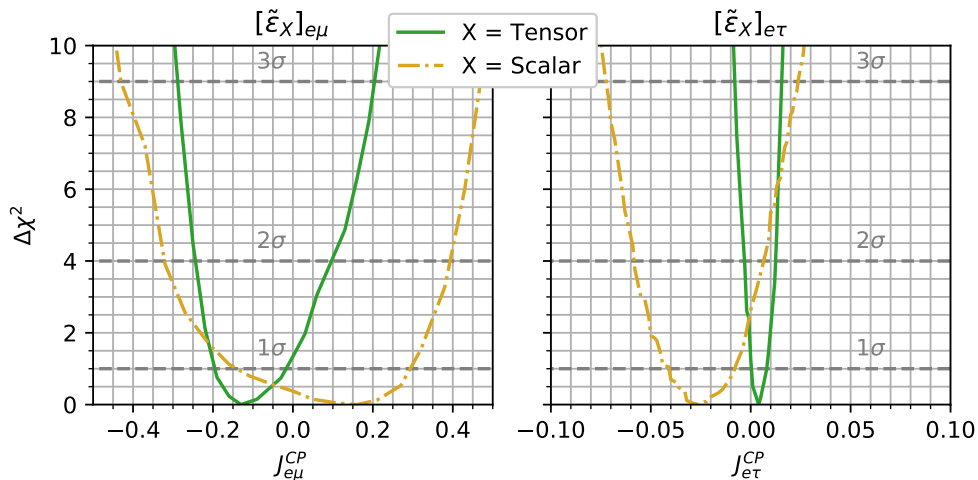


Figure 3.14: In this figure we show the $\Delta\chi^2$ as function of the CP-violation parameters, in the left (right) panel we show the $J_{e\tau}$ ($J_{e\mu}$) parameters of Eqs. (3.124) and (3.125).

3.4.4 JUNO

The JUNO experiment is a proposed experiment [73] that aims to solve the mass hierarchy problem with a significance of $3\sigma - 4\sigma$. The JUNO experiment will use reactor neutrinos in a baseline of around 56 km to measure the standard oscillation parameters with a precision of more than 1%. We assume an exposure that corresponds to a 1.4×10^5 events in the simulation. As JUNO is a reactor oscillation experiment, the underlying physics is the same as the reactors used here.

Our results found no implications for NSI in the normal and inverted ordering. The parameter limits are shown in figure 3.15, where we can see that JUNO has a strong sensitivity to Δm_{31}^2 , it can help to break the degeneracy between Δm_{31}^2 and $\text{Im}[\tilde{\epsilon}_X]_{e\tau}$ that appeared on sec. 3.4. For $\text{Im}[\tilde{\epsilon}_X]_{e\mu}$ JUNO can check the preference for non-zero CP-violation coming from Daya Bay.

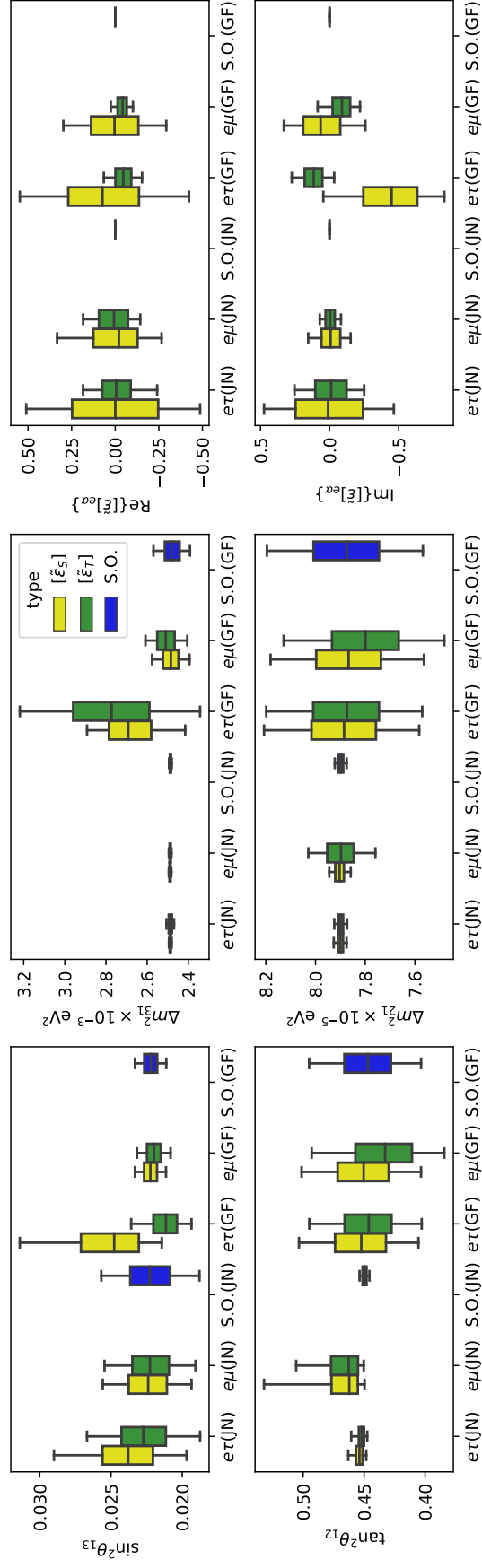


Figure 3.15: Here we show a similar analysis to 3.8, but including JUNO for comparison. Here, GF means our global analyses (without JUNO), and JN is the only JUNO analysis.

Chapter 4

Non-standard neutrino interactions: production and detection (NC)

This chapter explores the famous Large-Mixing Angle Dark (LMA-D) solution. It is one of several solutions that still allow us to explain solar neutrinos. At the time of the measurement of solar neutrino oscillation, the available data was compatible with at least four solutions of standard neutrino oscillation, the Large Mixing Angle (LMA), the Small Mixing Angle (SMA), the Vacuum solution (VAC), and the MSW low mass (LOW) solution. These were distributed around the space of parameters of neutrino oscillations, as shown in Fig. 4.1.

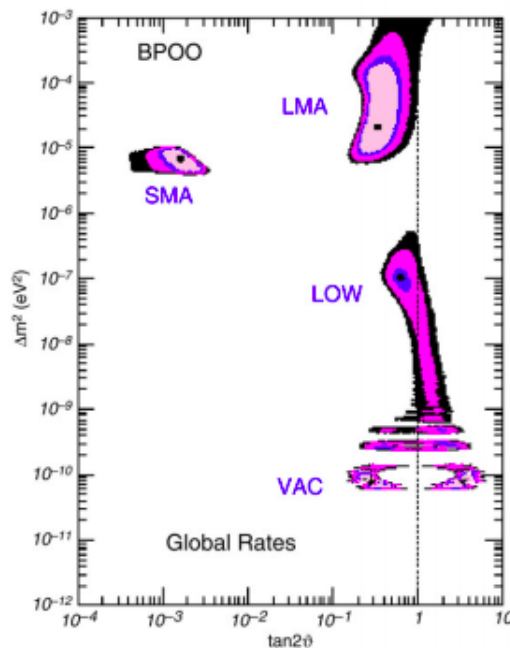


Figure 4.1: Neutrino parameter space at the beginning of the 2000's. Figure from Ref. [4].

Later, with more data and independent KamLAND findings [52], it was shown

that the correct solution was the LMA. Fig. 4.2 shows the solution for the solar neutrino and the KamLAND cases.

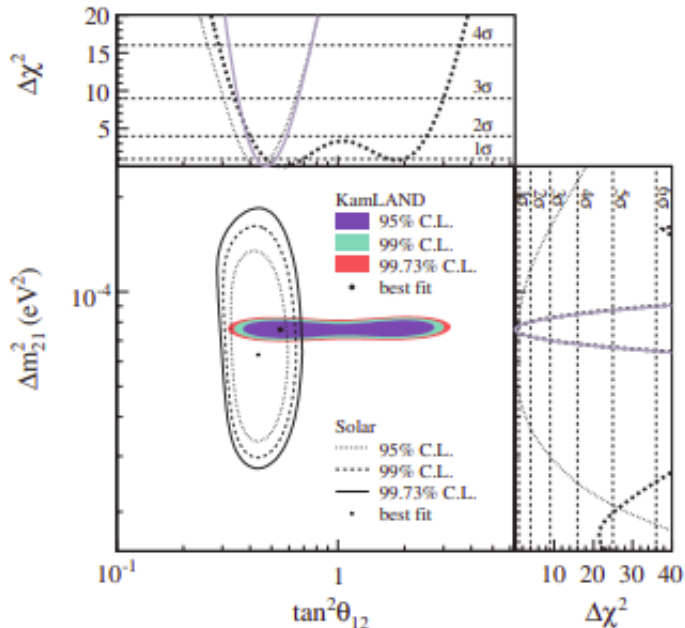


Figure 4.2: In this figure we show the contours at 95%, 99% and 99,73% form KamLAND (colored) and for Solar neutrinos (black lines), for Ref. [5].

The LMA-D solution can be calculated by using the Hamiltonian for neutrinos in the matter:

$$\hat{H} = \mathcal{M} + \mathcal{V} = \frac{1}{2E_\nu} \left[U^\dagger \begin{pmatrix} 0 & 0 & 0 \\ 0 & \Delta m_{21}^2 & 0 \\ 0 & 0 & \Delta m_{31}^2 \end{pmatrix} U \right] + \begin{pmatrix} V_{CC} & 0 & 0 \\ 0 & 0 & 0 \\ 0 & 0 & 0 \end{pmatrix} \quad (4.1)$$

where V_{CC} is the neutrino potential given by (3.74). In the vacuum, that is, if $V_{CC} = 0$, this Hamiltonian is invariant under the transformation

$$\Delta m_{31}^2 \rightarrow -\Delta m_{32}^2, \quad (4.2)$$

$$\sin \theta_{12} \rightarrow \cos \theta_{12}, \quad (4.3)$$

$$\delta \rightarrow \pi - \delta, \quad (4.4)$$

where $\sin \theta_{12} \rightarrow \cos \theta_{12}$ is equivalent to $\tan \theta_{12} \rightarrow 1/\tan \theta_{12}$ which represents $\tan \theta_{12} > 1$ and the $\tan \theta_{12} < 1$, the left and the right-side solutions of KamLAND in Fig. 4.2. Once solar neutrinos are sensitive to the MSW effect, the matter potential breaks the degeneracy of the Hamiltonian, leading to the exclusion of the LMA-D solution is exclusion by solar

neutrinos. On the other hand, if non-standard neutrino interactions are present, the Hamiltonian for neutrino propagation will not be the same as in Eq. (4.1), but

$$\mathcal{V} = V_{CC} \begin{pmatrix} 1 + \epsilon_{ee} & \epsilon_{e\mu} & \epsilon_{e\tau} \\ \epsilon_{\mu e} & \epsilon_{\mu\mu} & \epsilon_{\mu\tau} \\ \epsilon_{\tau e} & \epsilon_{\tau\mu} & \epsilon_{\tau\tau} \end{pmatrix}, \quad (4.5)$$

where $\epsilon_{e\mu} = \sum_{f=e,d,u} N_f(x)/N_e(x) \epsilon_{\alpha\beta}^f$. For neutral currents the couplings on (4.5) are the strength of the non-standard interactions

$$\mathcal{L}_{\text{NSI}} = -2\sqrt{2}G_F \epsilon_{\alpha\beta}^f (\bar{\nu}_{\alpha L} \gamma_{\mu} \nu_{\beta L}) (\bar{f} \gamma^{\mu} f). \quad (4.6)$$

If we consider $N_f(x)/N_e(x) \approx \text{constant}$, the neutrino Hamiltonian is invariant under the following transformation [74]

$$(\epsilon_{ee} - \epsilon_{\mu\mu}) \rightarrow -(\epsilon_{ee} - \epsilon_{\mu\mu}) - 2, \quad (4.7)$$

$$(\epsilon_{\tau\tau} - \epsilon_{\mu\mu}) \rightarrow -(\epsilon_{\tau\tau} - \epsilon_{\mu\mu}), \quad (4.8)$$

$$\epsilon_{\alpha\beta} \rightarrow -\epsilon_{\alpha\beta}^*, \quad (4.9)$$

$$\Delta m_{31}^2 \rightarrow -\Delta m_{32}^2, \quad (4.10)$$

$$\sin \theta_{12} \rightarrow \cos \theta_{12}, \quad (4.11)$$

$$\delta \rightarrow \pi - \delta. \quad (4.12)$$

One can notice that it leads to a new solution compatible with the presence of a matter potential. This is called the LMA-D degeneracy and was unresolved for all neutrino experiments up to the results of Ref. [75].

Once for oscillation experiments in matter electrons and protons have almost the same density, the electron neutrino component can be neglected without the loss of generality. With that, for theories where the lepton flavor coupling is independent of the quark coupling, it can be parametrized by:

$$\epsilon_{\alpha\beta}^f = \sqrt{5} \epsilon_{\alpha\beta}^{f,\eta} (\cos \eta + Y(x) \sin \eta), \quad (4.13)$$

where $Y(x) = N_n(x)/N_p(x)$ is the ratio between the number density of neutrons and protons. The η parameter controls the strength of the interaction between protons and neutrons, and the $\epsilon_{\alpha\beta}^{\eta}$ controls the magnitude of the coupling, see Ref. [6]. In the next section, we will see how it is possible to resolve this degeneracy with scattering experiments.

4.1 CE ν NS

As we have seen, if non-standard interactions (NSI) as in Eq. (4.6) does exist, it can be predicted on neutrino oscillation experiments as solar neutrino and some long-baseline accelerator experiments. On the other hand, NSI can also be seen in scattering experiments where the neutrinos are measured near the source. Scattering experiments provides a vast number of events and, consequently, a clean signal of neutrinos.

The neutrino scatters at a target in a scattering experiment, usually a nucleon. The target can also be an electron, but for this, the data is very scarce; see Ref. [6]. For collisions with nucleons, the CHARM experiment [76] provides strong bounds on NSI. However, CHARM is a high-energy experiment and does not provide bounds for small mass mediators ($M \ll 100$ GeV).

Alternatively, a low-energy experiment is required to study small-mass mediators. In this sense, there is the coherent elastic neutrino-nucleus scattering (CE ν NS). This process appears at low-energy neutrino interactions with nucleons and is the dominant process for neutrino energies $E_\nu < 40$ MeV, providing model-independent bounds on neutrino interactions. The differential cross section of a neutrino with energy E_ν on a nucleus with Z protons, N neutrons, and mass M reads [77]:

$$\frac{d\sigma}{dT} = \frac{G_F^2}{2\pi} Q^2 F^2(q^2) M \left(2 - \frac{MT}{E_\nu^2} \right). \quad (4.14)$$

Here, T is the recoil energy of the nucleus, $F(q^2)$ is the nuclear form factor depending on the squared momentum transfer, $q^2 = 2MT$, and Q^2 is the weak charge of the nucleus. In the Standard Model (SM), the weak charge value is

$$Q_{\text{SM}}^2 = (Zg_p^V + Ng_n^V)^2, \quad (4.15)$$

with the tree-level relations $g_p^V = 1/2 - 2\sin^2\theta_W$ and $g_n^V = -1/2$. For the weak mixing angle θ_W , we follow the low-energy value calculated in [78].

For our case of study, it is always possible to consider the effect of NC NSI by replacing Q_{SM}^2 with an effective weak charge. The effective weak charge will be dependent on the flavor α of the incoming neutrino [79]:

$$\begin{aligned} Q_\alpha^2 &= [Z(g_p^V + \varepsilon_{\alpha\alpha}^p) + N(g_n^V + \varepsilon_{\alpha\alpha}^n)]^2 + \sum_{\beta \neq \alpha} [Z\varepsilon_{\alpha\beta}^p + N\varepsilon_{\alpha\beta}^n]^2, \\ &= (Q_{\text{SM}} + Z\varepsilon_{\alpha\alpha}^{Y,\eta})^2 + Z^2 \sum_{\beta \neq \alpha} \left(\varepsilon_{\alpha\beta}^{Y,\eta} \right)^2. \end{aligned} \quad (4.16)$$

Here, we can fix the neutron to proton ratio and, from Eq. (4.13) define an effective $\varepsilon_{\alpha\beta}^{Y,\eta}$. For simplicity, we assume that the off-diagonal NSI coefficients are real. The first

Target	Z	Y	η_{blind}	$-Q_{\text{SM}}$	σ/Q_{SM}^2	σ_μ/σ
C ₃ F ₈	8.2	1.081	-42.8°	4.27	13.3%	∞
Si	14	1.006	-44.8°	6.72	17.6%	∞
Ar	18	1.235	-39.0°	10.71	12.0%	∞
Ge	32	1.270	-38.2°	19.6	14.2%	4.20
CsI	54	1.405	-35.4°	36.7	12.5%	3.37
Xe	54	1.431	-35.0°	37.4	12.0%	4.01

Table 4.1: The number of protons Z , the neutron-to-proton ratio $Y = N/Z$, the corresponding blind spot η_{blind} , eq. (4.17), and the value of the SM weak charge, Q_{SM} , for different target materials. We use the average N corresponding to the natural isotope abundances, and for the molecules C₃F₈ and CsI, we take the average Z and N values. The last two columns show our assumptions about the measurement uncertainties obtainable at ESS.

term in eq. (4.16) corresponds to interactions conserving flavor process (the diagonals of Eq. (4.1)) $\nu_\alpha + A \rightarrow \nu_\alpha + A$. For this term, represents the NSI amplitude interfere with the SM, whereas the second term is flavor changing neutral current (FCNC) scattering, $\nu_\alpha + A \rightarrow \nu_\beta + A$.

From Eqs. (4.16) and (4.13), it follows that an experiment with a given target nucleus will not be sensitive to NSI if $\epsilon_{\alpha\beta}^{Y,\eta} = 0$, which happens for

$$\eta_{\text{blind}} = -\arctan\left(\frac{1}{Y}\right). \quad (4.17)$$

In Table 4.1, we list some of the possible detector targets used in this work, and we show their values for Z , Y , and η_{blind} . Before [75], the LMA-dark was allowed for values of η close to the blind spot of CsI, $\eta_{\text{blind}}^{\text{CsI}} \approx -35.4^\circ$. The CsI was the target used in the first measurement of CE ν NS. In order to resolve the LMA-D degeneracy, the data from a target with an η_{blind} sufficiently smaller than this value is needed.

4.2 COHERENT

The COHERENT experiment was the first experiment to obtain the CE ν NS signal [80]. The COHERENT collaboration used a stopped neutron source to provide an electron (and muon) neutrino beam that and measure the recoil of a CsI nucleon. We will use the COHERENT data to provide limits on the weak charge and the NSI parameters of the LMA-D degeneracy.

For COHERENT(CsI), we use timing information measurement in CsI and discussed ref. [6]. The time information implies a correlation between Q_μ and Q_e mea-

measurements, which can be estimated from figure 6 of ref. [6]. In order to be conservative, we choose to use the Chicago Quenching Factor (QF) result (which has the largest uncertainty). We use the following $\chi^2_{\text{coh.}(CsI)}$ function

$$\chi^2_{\text{coh.}(CsI)}(Q_e, Q_\mu) = \begin{pmatrix} \Delta Q_e & \Delta Q_\mu \end{pmatrix} \begin{pmatrix} \sigma_e^2 & \rho\sigma_e\sigma_\mu \\ \rho\sigma_e\sigma_\mu & \sigma_\mu^2 \end{pmatrix}^{-1} \begin{pmatrix} \Delta Q_e \\ \Delta Q_\mu \end{pmatrix}. \quad (4.18)$$

Here, $\Delta Q_\alpha = Q_\alpha - Q_\alpha^{\text{bfp}}$, where we estimate $\rho = -0.687$, $\sigma_e = 965.5$, $\sigma_\mu = 436.5$, $(Q_e^{\text{bfp}})^2 = 1008.3$ and $(Q_\mu^{\text{bfp}})^2 = 1193.9$. The result of eq. (4.18) is shown in figure 4.3.

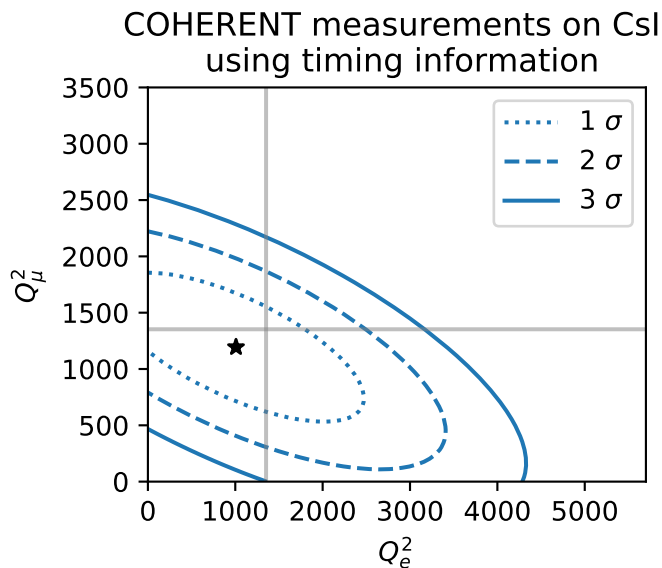


Figure 4.3: Contours on 1σ , 2σ and 3σ (two dof) on the χ^2 of eq. (4.18) for the Chicago QF from ref. [6]. The SM weak charge for CsI is shown by the gray line $Q_{SM}^2 \approx 1352.5$.

At the time of our calculations, preliminary results presented in ref. [81] were released. Here, we use the preliminary results. For comparison with the original 2017 results of COHERENT [80], the statistics have increased, and new data on the quenching factor have become available. It led to an overall improvement in precision from 33% of the 2017 analysis to around 16%.

The results of Ref. [81] are reported in terms of the correlated determination of averaged cross-sections $\langle\sigma_\mu\rangle$ and $\langle\sigma_e\rangle$, corresponding to the averaged ν_μ and ν_e flux contributions to the observed CE ν NS cross-section. In order to reproduce these results, we use that $\langle\sigma_\alpha\rangle \propto Q_\alpha^2$ ($\alpha = e, \mu$) and use assume the same χ^2 function as in Eq. (4.18). We find that with the values $\rho = -0.790$, $\delta_e = 1204.7$, $\delta_\mu = 404.6$, $(Q_e^{\text{bfp}})^2 = 1200.0$ and $(Q_\mu^{\text{bfp}})^2 = 1245.1$ it was possible to replicate their results. Using eq. (4.16), it is straightforward to transform $\chi^2_{\text{Coh}(CsI)}(Q_e^2, Q_\mu^2)$ into $\chi^2_{\text{Coh}(CsI)}(\epsilon^\eta, \eta)$.

For Argon measurements in COHERENT, we use the data released in Ref. [82].

Then, we estimate the weak charge measurement uncertainty, assuming that COHERENT measures the total rate. In that case, our χ^2 is given by:

$$\chi_{\text{coh. (Ar)}}^2 = \frac{(f_e Q_e^2 + f_\mu Q_\mu^2 - (Q^{\text{bfp}})^2)^2}{\sigma^2}, \quad (4.19)$$

where, $f_e \approx 0.3$ and $f_\mu \approx 0.7$ were taken from Ref. [80, 83]. The $\sigma = 25.0$ is the total rate error and $Q^{\text{bfp}} = -12.2$ is the best fit point measured. We estimate those values from fig. 6 of Ref. [82], using the following effective weak charge:

$$Q_e^2 \equiv [Q_{SM} + Z_{CsI}(2 + Y_{CsI})\varepsilon_{ee}^u + Z_{CsI}(1 + 2Y_{CsI})\varepsilon_{ee}^d]^2. \quad (4.20)$$

Our estimates can be seen in Fig. 4.4.

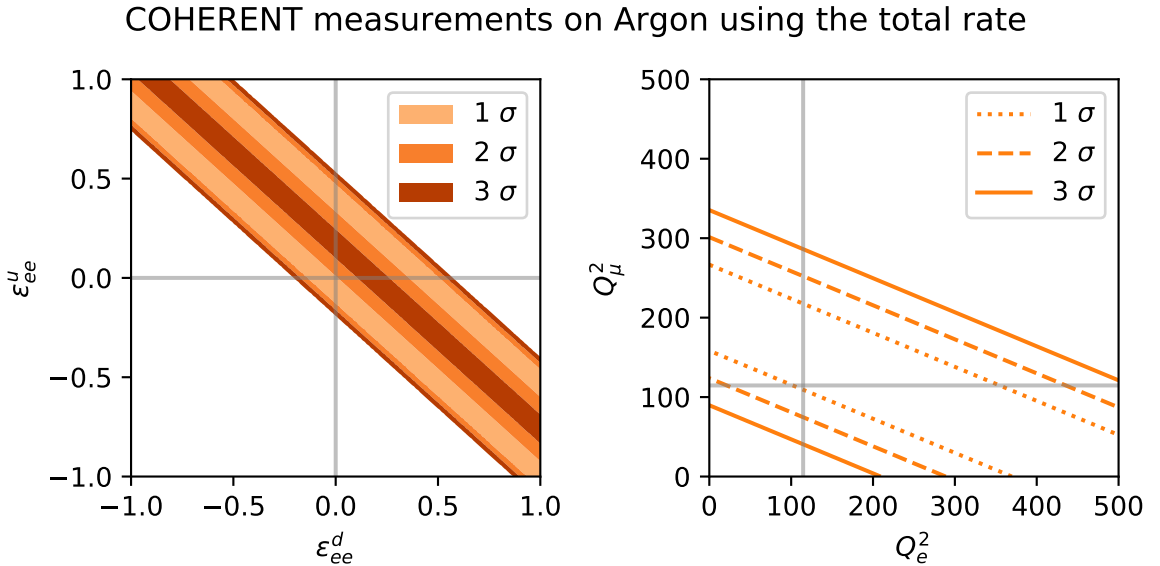


Figure 4.4: In the left: We show our prediction of Fig 6. of Ref. ?? using eq. (4.19) at 1σ , 2σ and 3σ (two dof) C.L.. In the right: using the eq. (4.19), we plot the 1σ , 2σ and 3σ (two dof) C.L. for the effective weak charge. The standard model weak charge in that case is $Q_{Ar}^2 \approx 114.64$.

We combine Argon and CsI measurements on COHERENT, assuming no correlation between the measurements. In that case, we follow flavor-independent model parametrization:

$$Q_\alpha^2 \equiv [Q_{SM} + Z_{exp}\varepsilon_{\alpha\alpha}^{\text{exp}}]^2, \quad (4.21)$$

where

$$\varepsilon_{\alpha\alpha}^{\text{exp}} = \sqrt{5}(\cos \eta + Y^{\text{exp}} \sin \eta)\varepsilon_{\alpha\alpha}^\eta. \quad (4.22)$$

Using the assumption of no correlation between Ar and CsI, we use

$$\chi_{\text{coh.}}^2 = \chi_{\text{coh. (CsI)}}^2 + \chi_{\text{coh. (Ar)}}^2, \quad (4.23)$$

and, instead of using $\chi_{\text{coh.}}^2(Q_e, Q_\mu)$, we will use $\chi_{\text{coh.}}^2(\epsilon_{ee}^\eta, \epsilon_{\mu\mu}^\eta, \eta)$. In Fig. 4.5, we show the combination of COHERENT CsI and Ar measurements for four different model scenarios: when Argon is blind to non-standard interactions (first column of the first line), when CsI is blind to the new interactions (second column of the first line), when light matter (the ratio of protons and neutrons is equal to 1) is blind to non-standard interactions, and when the interaction happens only with protons. With the dashed orange curve, we show the Ar measurement; in the plain blue line curve, we show the CsI measurement, and in purple shaded region, both together using eq. (4.23). As can be seen, when Argon is blind to NSI, NSI has constraints from CsI, and when CsI is blind NSI is, the NSI constrained by Ar.

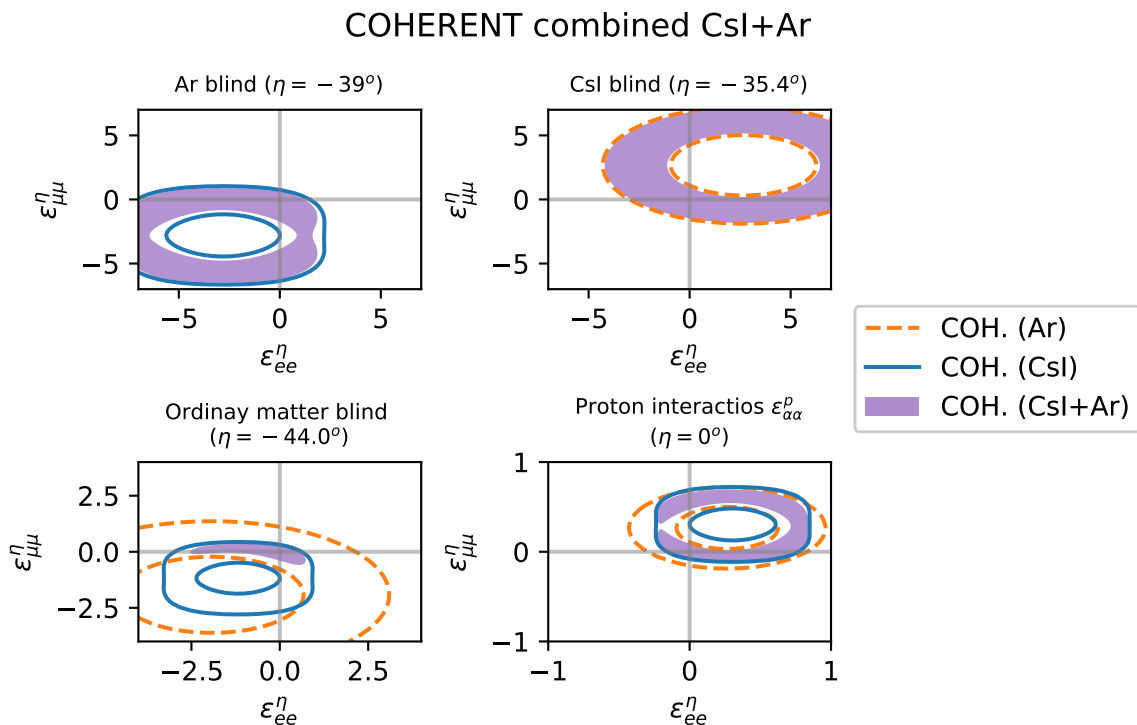


Figure 4.5: Here we show the 3σ regions for four different models depending on η . With the dashed orange curve, we show the COHERENT argon measurement. The blue straight curve shows the COHERENT CsI results, and the purple shaded region represents the combination of COHERENT CsI and Ar. From ref. [7].

4.2.1 Global oscillation limits on non-standard neutrino interactions

In order to test the LMA-dark solution discussed in the last section, we will compare it with the LMA-light solution. We then define the following $\Delta\chi^2$:

$$\Delta\chi^2(\epsilon^\eta, \eta) = \chi_D^2(\epsilon^\eta, \eta) - \chi_{L,\min}^2, \quad \chi_{L,\min}^2 = \min_{\epsilon^\eta, \eta} \chi_L^2(\epsilon^\eta, \eta). \quad (4.24)$$

Here, $\epsilon^\eta = (\epsilon_{\alpha\beta}^\eta)$ is a short-hand for all NSI coefficients, and $\chi_{D,L}^2(\epsilon^\eta, \eta)$ are the χ^2 functions describing the LMA-dark ($\theta_{12} > 45^\circ$) or LMA-light ($\theta_{12} < 45^\circ$) solutions in the parameter space. The $\Delta\chi^2$ in eq. (4.24) is the test statistics that quantify if the LMA-dark solution is disfavoured concerning LMA-light. In particular,

$$\Delta\chi_{DL}^2 \equiv \min_{\epsilon^\eta, \eta} [\Delta\chi^2(\epsilon^\eta, \eta)] = \chi_{D,\min}^2 - \chi_{L,\min}^2 \quad (4.25)$$

corresponds to the log-likelihood ratio of the two hypotheses LMA-dark versus LMA-light. Here, we will evaluate $\Delta\chi_{DL}^2$ from eq. (4.25) for one dof (free η) to quantify the exclusion of the LMA-dark degeneracy. In order to perform the minimization over the NSI parameters, we use a Monte Carlo minimization based on the differential evolution method [84]. The numerical calculations are performed with the SciPy library [85] in python that already has this algorithm implemented.

Minimizing multi-variable functions can be a difficult task depending on which type of function is minimized. Moreover, it can be tricky if the function behavior is not well known, if the function's derivative is not continuous, or if we have several local minima. In this context, Monte Carlo minimization is a commonly used approach. In this work, we use a kind of Monte Carlo minimization; the differential evolution method [84].

The differential evolution method is based on the "philosophy" of evolutionary biology. For the $\chi^2(\vec{\epsilon})$ function, where $\vec{\epsilon}$ is NSI vector space, the differential evolution algorithm works with the implementation of a set of N "individuals" (we use 15) in the NSI parameter space. Several proposals for the initial positions can be made depending on the previous knowledge of the global minimum. In our case, we choose it uniformly randomly between the boundaries¹ of NSI that comes from oscillation experiments. Thereby, given the initial positions of the population, we choose a random set of three individuals, and based on those three, we propose a new "mutant". Here, the mutations $\vec{\epsilon}_{\text{new}}$ are new values of the NSI based on the three we sorted, and we do that procedure for each one of them. Several strategies can be used to generate those mutations, e.g., binomial or exponential. For each case we tested to see which was the best option, for example:

$$\vec{\epsilon}_{\text{new}} = \vec{\epsilon}_{\text{best}} + \mu \vec{M}(\Delta\vec{\epsilon}). \quad (4.26)$$

where μ (we use 0.5) is the mutation factor, $\Delta\vec{\epsilon}$ is the difference between the position complementary sorted vectors, and \vec{M} is a function that depends on the mutation method. For the binomial case, it randomly chooses with some probability p (we use 0.7) if the

¹The boundaries we use were always the 4/3 of the NSI largest values among the η of oscillation experiments.

mutation will be implemented or not. After creating a new mutated individual in the population, we can choose if we substitute the old one with the new one based on the minimum values of the function χ^2 . Finally, we can repeat that procedure until we have some desired convergence of the population to the χ^2 minimum value with a given tolerance.

The minimization was made using the Scipy library [85] in python that already has this algorithm implemented.

Oscillation experiments. The data from oscillation experiments was included by using the results of the global analysis from ref. [86]. We reconstruct approximate functions for the $\chi_{L,\text{osc}}^2(\epsilon^\eta, \eta)$ and $\chi_{D,\text{osc}}^2(\epsilon^\eta, \eta)$ from figs. 7 and 10 of ref. [86] (2020 updated version).² We refer the reader to that reference for further details about the statistical analysis and used data.

4.2.2 Results

Here we show the results of our analysis, including the oscillation data. The inclusion of oscillation data is made by including a χ function as described in the last section. We are interested in knowing the data preference between the light side and the dark side. Hence, we assume that the oscillation and the COHERENT measurements are uncorrelated summing the χ functions:

$$\Delta\chi^2 = \Delta\chi^2(\epsilon^\eta, \eta) + \sum_{i=\{CsI, Ar\}} \chi_i^2(\epsilon^\eta, \eta), \quad (4.27)$$

where the first term is the χ^2 for oscillation as given in Eq.(4.24), and the second term sums the χ^2 of Eqs. (4.18) and (4.19). The function $\Delta\chi_{\text{osc}}^2$ minimized with respect to all ϵ^η is shown as black-dotted curve in fig. 4.6. We restrict to the range $-50^\circ \lesssim \eta \lesssim 0^\circ$ since outside this region, LMA-dark is strongly disfavoured [6]. We see that oscillation data by themselves exclude LMA-dark for values of $\eta \lesssim -37^\circ$ at more than 3σ , while for $-25^\circ < \eta < 0^\circ$, LMA-dark provides a comparable fit as LMA-light with $\Delta\chi_{DL}^2 \lesssim 2$.

²We are grateful to the authors of ref. [86] for providing us a χ^2 -table corresponding to an updated version of their fig. 7. Let us note that the figure shows marginalized regions for each $\epsilon_{\alpha\beta}^\eta$ as a function of η . Therefore, we neglect correlations between the different $\epsilon_{\alpha\beta}^\eta$. Our exclusions will be conservative; if parameter correlations can be included, exclusions of the LMA-dark degeneracy would be somewhat stronger.

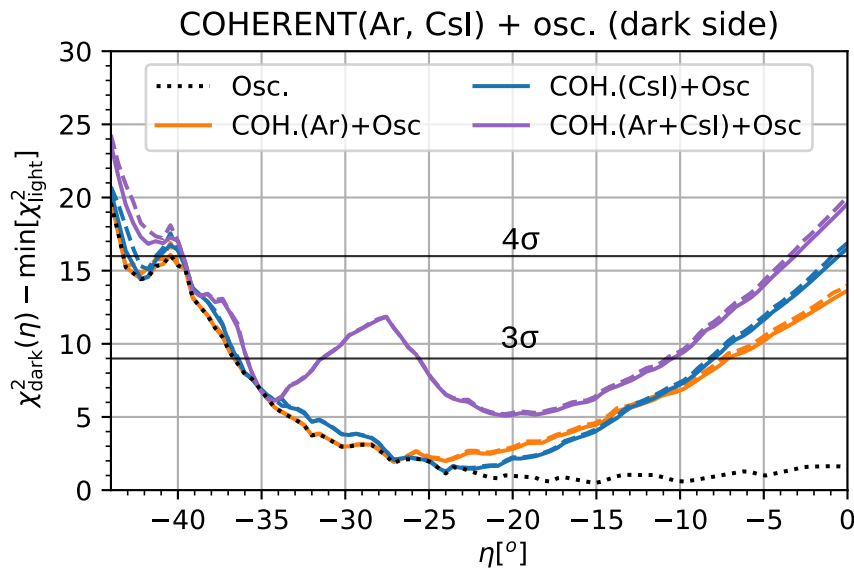


Figure 4.6: For oscillation, we show the $\Delta\chi^2$ of the LMA-D solution minimized on $\epsilon_{\alpha\beta}^\eta$ and as a function of η (dotted black). For COHERENT, we show each target separated and in a joint analysis: oscillations+COHERENT(CsI) (blue), oscillations+COHERENT(Ar) (orange), and all data sets combined (purple). For the dashed curves, the off-diagonal $\epsilon_{\alpha\beta}^\eta$ are fixed at zero, and for the solid curves, we minimize over them. From ref. [7].

4.3 ESS

Given the results of the last section, we are naturally led to investigating future $\text{CE}\nu\text{NS}$ measurements with the potential to exclude the LMA-dark with high significance. Therefore, we replicate the results from [87] and use their results to follow our discussions. This work will consider future $\text{CE}\nu\text{NS}$ measurements that use either stopped pions or nuclear reactor sources of neutrino. The main difference between those experiments is the neutrino energy and the neutrino flavor component. In a reactor, electron antineutrinos are produced, whereas in stopped pions sources, there is a combination of electron, muon, and antimuon neutrinos. In this section, we study only stopped pion source, and in the next section, we include reactors in the analysis. Below we will always assume that the best-fit point for a hypothetical future experiment is at Q_{SM}^2 , i.e., no NSI. Then we calculate the sensitivity to constrain Q_e^2 and Q_μ^2 where the measurement uncertainty (from Ref. [87]) and add the resulting χ^2 to the (4.27).

To be specific, in this section, we consider as an example for a stopped pion source the sensitivity of a possible $\text{CE}\nu\text{NS}$ measurement at the European Spallation Source (ESS) [8]. The ESS can increase neutron luminosity by a factor of 30–100 concerning previous spallation sources and an order of magnitude larger neutrino fluxes than the Spallation Neutron Source (SNS) where the COHERENT experiment is located. The sensitivity of

CE ν NS measurements using different detector technologies based on various target materials has been investigated in ref. [8], where details about the assumed experimental configurations can be found. See also [88] for some physics applications.

4.3.1 Analysis

The European Spallation Source (ESS) is a proposed low energy neutrino beam. It is similar to the COHERENT neutrino beam, and it is proposed to be the most intense spallation neutron source. Indeed, there is a proposal to measure CE ν ENS on ESS using a list of targets, see Ref. [8]. Here, we use the simulated sensitivities of Ref. [8] to estimate the limits on the effective weak charges Q_e and Q_μ .

The total rate of the signal will dominate the CE ν NS measurement at ESS. We adopt the neutrino flavour contribution ratios to the event rate: $\nu_e : \nu_\mu : \bar{\nu}_\mu = (1 : 1 : 1)$; it corresponds to the effective weak charge combination $Q_e^2/3 + 2Q_\mu^2/3$. In some cases, the detector energy resolution allows to partially distinguish between electron neutrinos and muon neutrinos due to the spectral shape of their respective fluxes [8]. We suppose that an additional independent constraint on Q_μ can be obtained to implement this effect. Hence, we use the following χ^2 definition:

$$\chi_{\text{ESS}}^2 = \frac{(Q_{\text{SM}}^2 - Q_e^2/3 - 2Q_\mu^2/3)^2}{\sigma^2} + \frac{(Q_{\text{SM}}^2 - Q_\mu^2)^2}{\sigma_\mu^2}. \quad (4.28)$$

Here, σ (σ_μ) is the uncertainty on the total rate (on Q_μ^2). The uncertainty values have been chosen to match fig. 12 of [8]. Our results are listed for the various targets in tab. 4.1. In agreement with [8], we found rate uncertainties in the range from 12% to 18%. For Ge, CsI, and Xe targets, a constraint on Q_μ^2 with $\sigma_\mu/\sigma \simeq 4$ can be obtained, whereas for the lighter targets C₃F₈, Si, and Ar, the measurement is dominated by the total rate alone. With these assumptions, we can reproduce fig. 12 of [8] with excellent accuracy.

4.3.2 Results

In fig. 4.8, we show the sensitivity to exclude the LMA-dark solution adding an ESS measurement with single target nuclei to present data. The Ar, Xe and CsI targets can lead to a slight improvement in the statistics, increasing the $\Delta\chi^2$ by about 1 unit, and the same also for Ge, for which the improvement is about three units. These nuclei have their blind spot close to $\eta \approx -35^\circ$ (c.f., tab. 4.1). Therefore, it is impossible to significantly improve around that value of η concerning the present situation. On the other hand, a measurement using C₃F₈, especially Si, can significantly improve. From tab. 4.1 we see

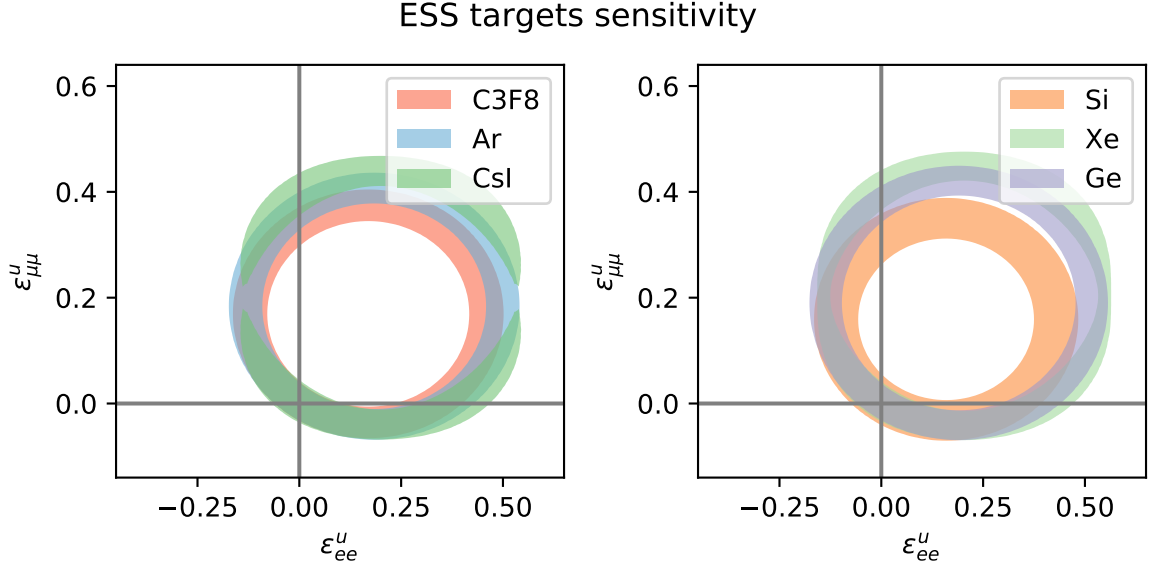


Figure 4.7: Our 90% C.L. curves for the eqs. (4.28) and (4.16) assuming different targets.

that they have a neutron-to-proton ratio as well as η_{blind} sufficiently different from CsI, such that they will be able to exclude LMA-dark with $\Delta\chi^2 \approx 16.1$ (Si) and 13.0 (C_3F_8).

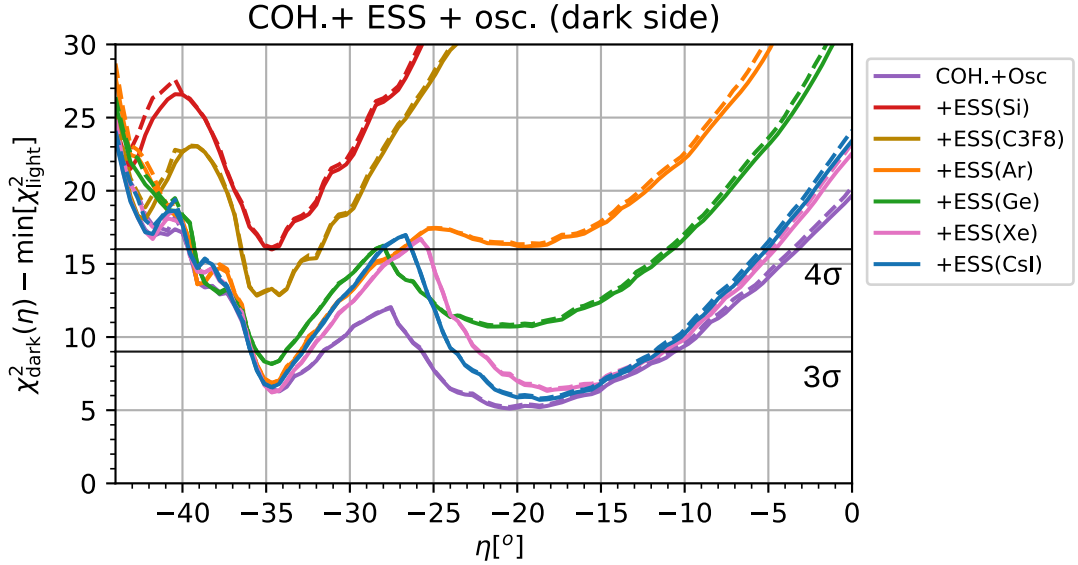


Figure 4.8: Expected sensitivity to exclude LMA-dark by a $\text{CE}\nu\text{NS}$ measurement at ESS using different target materials. For dashed curves the off-diagonal $\epsilon_{\alpha\beta}^\eta$ are fixed at zero, for solid curves we minimize with respect to them. From ref. [7].

The complementarity of Si measurement over present data is also illustrated in fig. 4.9. We see that in the relevant range of η the ellipse from the Si measurement only marginally touches the LMA-dark band at the 3σ level. From these plots, it is clear that also for the ESS measurement, we observe a similar effect of off-diagonal NSI parameters as for COHERENT: they are negligible once constraints from oscillations are included

c.f. dashed versus solid curves in fig. 4.8.

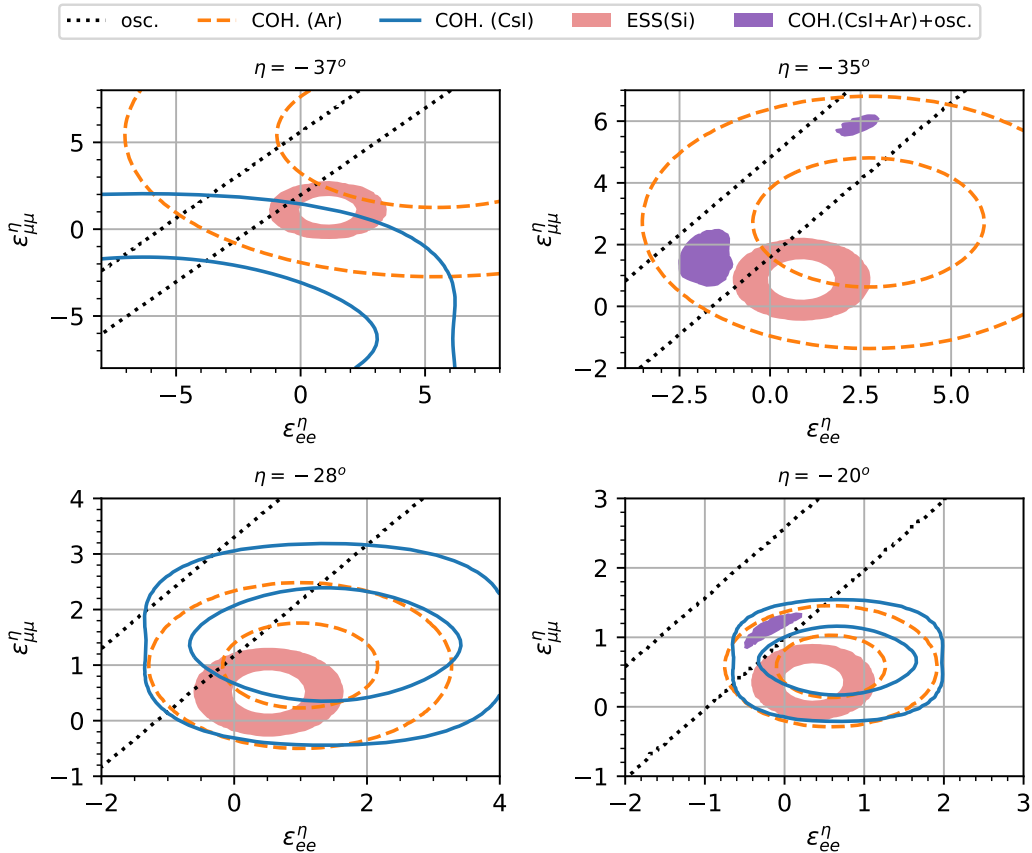


Figure 4.9: Allowed regions in the plane of ϵ_{ee}^η and $\epsilon_{\mu\mu}^\eta$ at $\Delta\chi^2 = 11.83$ corresponding to 3σ for two dof, for different fixed values of η . The contour lines correspond to the regions from oscillation data, COHERENT(CsI), and COHERENT(Ar) separately. The purple filled region is obtained by combining all three data sets. The diagonal band corresponding to oscillation data does not pass through the SM point $\epsilon_{\mu\mu}^\eta = \epsilon_{ee}^\eta = 0$ because we have assumed the LMA-dark solution with $\theta_{12} > 45^\circ$. The light-red filled region shows the sensitivity of a future measurement at ESS using Si detector, assuming the SM. Off-diagonal $\epsilon_{\alpha\beta}^\eta$ are fixed at zero. From ref. [7].

In fig. 4.10, we address the question of which accuracy for a CE ν NS measurement at a stopped pion source will be needed in order to disfavor LMA-dark significantly. We adopt the χ^2 from eq. (4.28), add it to the one from the present data, and show the difference between the χ^2 minima in the dark and light sides as a function of the relative measurement uncertainty of the weak charge. We see that for Si (C_3F_8), already for a rough measurement of $\sigma/Q_{SM}^2 \approx 1$ (0.5), LMA-dark will be disfavoured at $\Delta\chi^2 > 9$.

At small values of σ , the curves become flat. The asymptotic value for a given target material is determined by the size and location of the ring in the plane of ϵ_{ee}^η and $\epsilon_{\mu\mu}^\eta$ relative to the LMA-dark band.³ We see that Ar, Xe, and CsI targets would not

³The slight decrease at small σ for Ar, Xe, CsI results from the fact that the best-fit point in the light

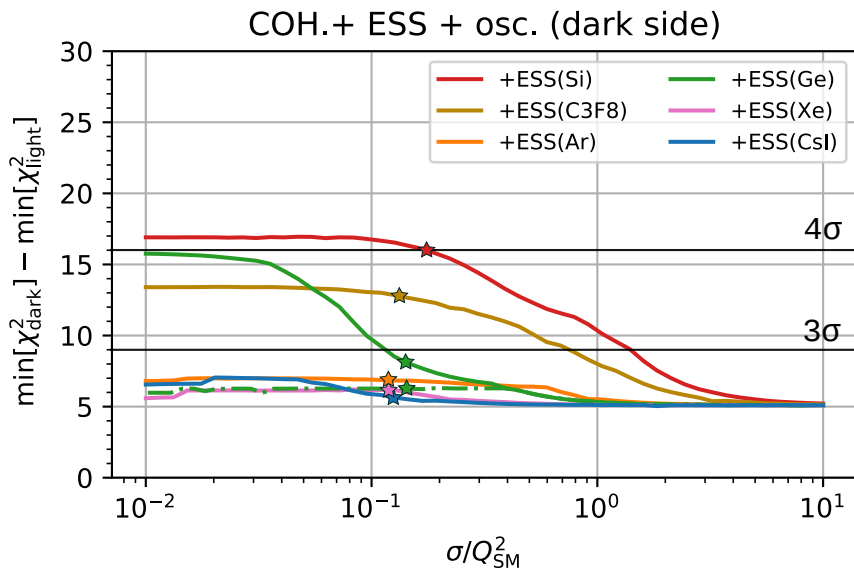


Figure 4.10: $\Delta\chi^2$ between the LMA-dark and LMA-light best-fit points as function of the relative measurement error σ/Q_{SM}^2 for a CE ν NS experiment at a stopped pion source for different target materials, assuming that the best-fit point corresponds to no NSI. In scaling σ we keep the ratio σ_μ/σ constant, using the value given in tab. 4.1. The dashed-green curve shows the result for Ge for $\sigma_\mu \rightarrow \infty$. The stars indicate the assumptions for ESS sensitivities based on [8]. From ref. [7].

reach 3σ even for ideal measurement. However, the asymptotic values for Si, Ge, C_3F_8 are roughly 17, 16, 12.5, respectively. If evaluated for one dof, this would correspond to about 4σ for Si and Ge, and 3.5σ for C_3F_8 . For Si and C_3F_8 , the asymptotic sensitivity is already achieved for σ/Q_{SM}^2 around 10%, and already our default assumptions for ESS are relatively close to them, as indicated by the stars in fig. 4.10.

Note that for Si and C_3F_8 , we assume a total rate measurement, constraining only the combination $(Q_e^2/3 + 2Q_\mu^2/3)$. For Ge, we show in fig. 4.10 the impact of a partial separation of Q_e^2 and Q_μ^2 . The solid green curve corresponds to the situation where in addition to the total rate, also Q_μ^2 can be determined with a relative precision of $\sigma_\mu/\sigma = 4.2$, as motivated by the results of [8]. In contrast, the dashed-green curve shows the result for Ge using only the total rate, i.e., setting $\sigma_\mu \rightarrow \infty$. For Ge, the separate Q_e^2/Q_μ^2 information is essential to disfavor LMA-dark at high significance. The reason for this becomes apparent in fig. 4.11, where we show a Ge measurement with a precision of factor 5 better than the ESS assumption using total rate information only (green shaded). We see that the ring passes precisely through the two islands for $\eta \approx -35^\circ$, and therefore, the degeneracy cannot be lifted for this value of η . The Ge constraint has a similar shape side from current data is not precisely at $\epsilon^\eta = 0$. By adding hypothetical ESS data assuming no NSI, the light-side best-fit point also changes slightly, decreasing $\Delta\chi^2$ between dark and light sides.

to the one from Ar due to the similar value of the neutron-to-proton ratios, c.f. tab. 4.1. However, if in addition to the total rate also separate information on Q_μ^2 is available, the ring becomes split into four islands (green-solid contours), and the degeneracy is resolved.

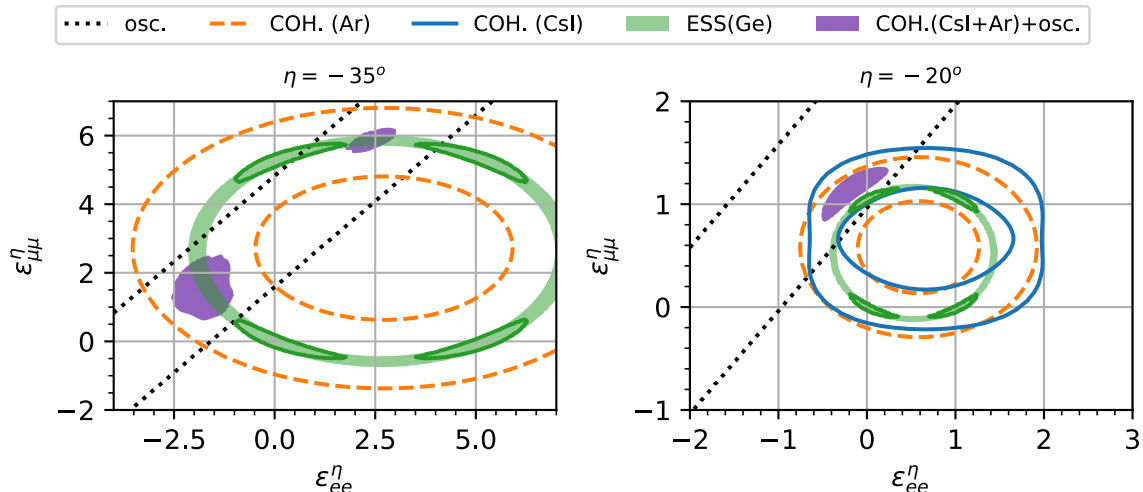


Figure 4.11: Same as fig. 4.9 but showing allowed regions at 3σ from a Ge target at a stopped pion source assuming a precision of $\sigma/Q_{SM}^2 = 0.028$, a factor 5 better than the ESS assumption from [8]. For the green-shaded region (green-solid contours) we assume $\sigma_\mu/\sigma = \infty$ (4.2). From ref. [7].

4.4 Reactors

Reactors are another source of low energy neutrinos highly used in the search for more $CE\nu NS$ data. As we mentioned in the previous chapter, antineutrinos are created in the beta decay processes in reactors. The neutrino energy spectrum is defined by the set of parent nuclei and the energy of the final nuclei. Therefore, the total rate of the flux is subject to systematic uncertainty from the flux modeling. For reactors, the systematic is around $\sim 5\%$. Hence, we assume the following χ^2 function for reactors:

$$\chi_{\text{reactor}}^2 = \frac{(N_{SM} - N_e)^2}{(N_{SM}\sigma_{sys}(\%))^2}. \quad (4.29)$$

For $CE\nu NS$, the total number of events is proportional to the weak charge: $N_{\text{events}} \propto Q_e^2$. From that, we factorize the total constants leading to the following weak-charge χ^2 :

$$\chi_{\text{reactor}}^2 = \frac{(Q_{SM}^2 - Q_e^2)^2}{(Q_{SM}^2\sigma_{sys}(\%))^2} = \frac{(1 - Q_e^2/Q_{SM}^2)^2}{\sigma_{sys}^2} \quad (4.30)$$

In that case, if there is some systematic uncertainty, it will appear in the $\sigma_{\text{sys}}(\%)$. In the next section, we will explore the present CE ν NS limits on NSI and a combined sensitivity if one of the reactor experiments measures CE ν NS.

4.4.1 CONNIE Measurements

Here, we combine the low-energy CONNIE data [89] with our results. In ref. [89] the authors put bounds on light mediators in neutrino-nucleon interactions. Here, we are interested in the universal flavor-conserving coupling result. In ref. [89], the first energy bin was used to calculate the parameter limits, with the assumption that $N_{\text{obs}}/N_{\text{expected}} = 41$ at 95%. In that case, the chi-square function will be given by a Gaussian where they assume centered on zero:

$$\chi^2 = \frac{\left[\left(1 - \frac{Q_{Z'}}{Q_W} \right)^2 \right]^2}{\left(N_{\text{obs}}^{(1\sigma)} / N_{\text{expected}} \right)^2}. \quad (4.31)$$

In our case, we do not assume the Gaussian is centered on zero, but

$$\chi^2 = \frac{\left[N_{\text{obs}} - \left(1 - \frac{Q_{Z'}}{Q_W} \right)^2 N_{\text{expected}} \right]^2}{\left(N_{\text{obs}} - N_{\text{obs}}^{(1\sigma)} \right)^2}. \quad (4.32)$$

With that in hand, we made the fig. 4.12, trying to reproduce the results of ref. [89]. We include the CONNIE analysis in the global χ^2 (4.27) assuming the following χ^2 for

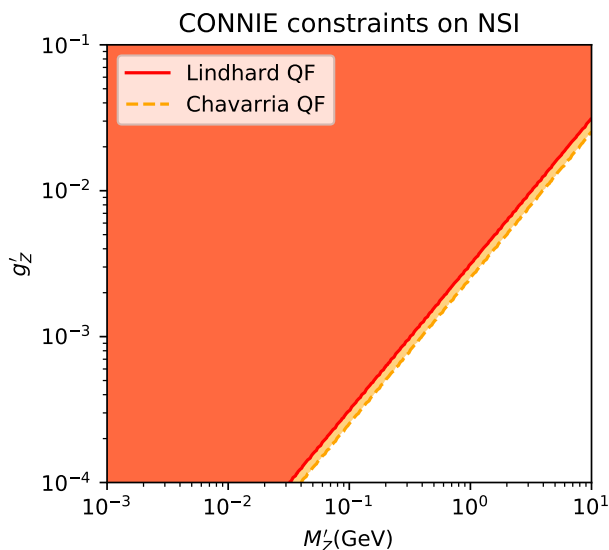


Figure 4.12: Limits on light mediators using the absence of a coherent neutrino nucleon scattering.

CONNIE:

$$\chi^2 = \frac{\left[N_{\text{obs}} - \left(\frac{Q_e}{Q_{\text{SM}}} \right)^2 N_{\text{expected}} \right]^2}{\left(N_{\text{obs}} - N_{\text{obs}}^{(1\sigma)} \right)^2}. \quad (4.33)$$

The result is shown in Fig. 4.13, where we can see that CONNIE helps in the analysis for $\eta \sim -33^\circ$. For this figure, we use the results of COHERENT CsI from [6] using timing information.

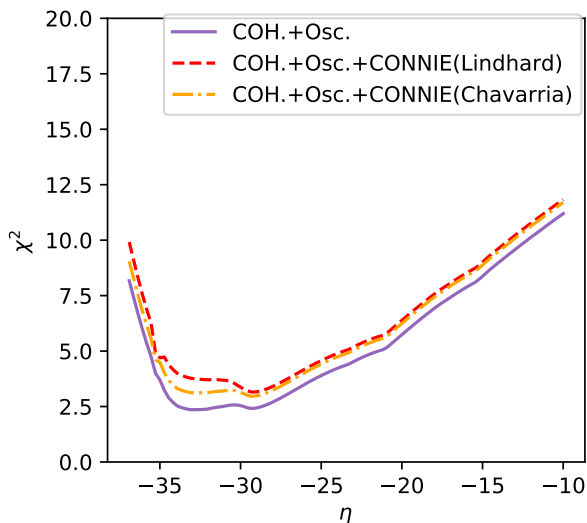


Figure 4.13: Global analysis with the limits on the LMA-D degeneracy.

4.4.2 Sensitivity

There are many ongoing or planned CE ν NS experiments at nuclear reactors; see [90] for a review. In this subsection, we address whether a reactor measurement can also serve to resolve the LMA-dark degeneracy. The most suitable difference to pion sources is the pure electron flavor of the reactor neutrino. Particularly, we will consider the ongoing CONNIE [91] and CONUS [92] experiments which use Si and Ge targets, respectively. However, both experiments have published the first results, which could not yet establish a significant measurement of CE ν NS events.

Similar to the above, we estimate the sensitivity of future reactor experiments by assuming a determination of the weak charge. We define

$$\chi_{\text{reac}}^2 = \frac{(Q_{\text{SM}}^2 - Q_e^2)^2}{\sigma_{\text{reac}}^2}, \quad (4.34)$$

where again we assume that the best-fit point is at Q_{SM}^2 and adopt a measurement uncertainty of $\sigma_{\text{reac}}/Q_{\text{SM}}^2 = 5\%$. While this appears to be a somewhat optimistic assumption, it

discusses the potential of a close-to-ultimate reactor measurement concerning the LMA-dark ambiguity.

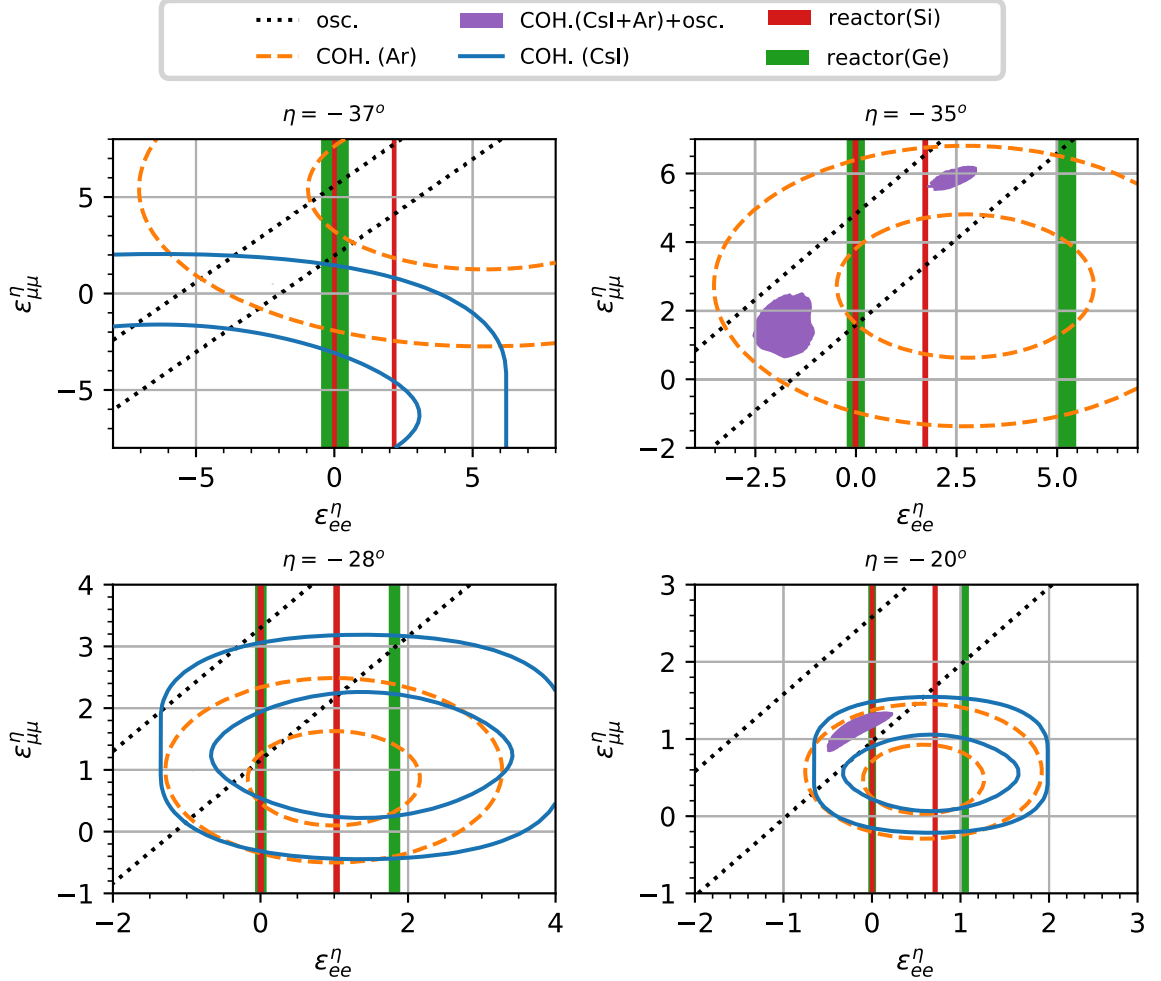


Figure 4.14: Same as fig. 4.9 with sensitivity of the reactor experiments using Ge and Si overlaid assuming a 5% measurement of the weak charge Q_{SM} . From ref. [7].

In Fig. 4.14, we show the constraints from a reactor experiment in the plane of ϵ_{ee}^η and $\epsilon_{\mu\mu}^\eta$ for four values of η . Since they are sensitive only to Q_e , the limits are vertical bands in these plots. It is clear that for values of η , for which the LMA-dark allowed region overlaps with $\epsilon_{ee}^\eta = 0$, such a measurement will not be able to exclude it. It is indeed the case for $\eta \approx -20^\circ$, as shown in the bottom-right panel of fig. 4.14.

This behavior is confirmed in fig. 4.15, where the sensitivity to exclude the LMA-dark solution is shown as a function of η . We observe that for $-27^\circ < \eta \lesssim -15^\circ$, reactor experiments can not improve concerning the present situation. Some improvement is possible for $\eta < -27^\circ$. However, reactor experiments lose their sensitivity at certain values of η in this region. The origin of this effect for Si is visible in the upper-right panel of fig. 4.14: it happens that the allowed band for non-zero ϵ_{ee}^η passes close to an island

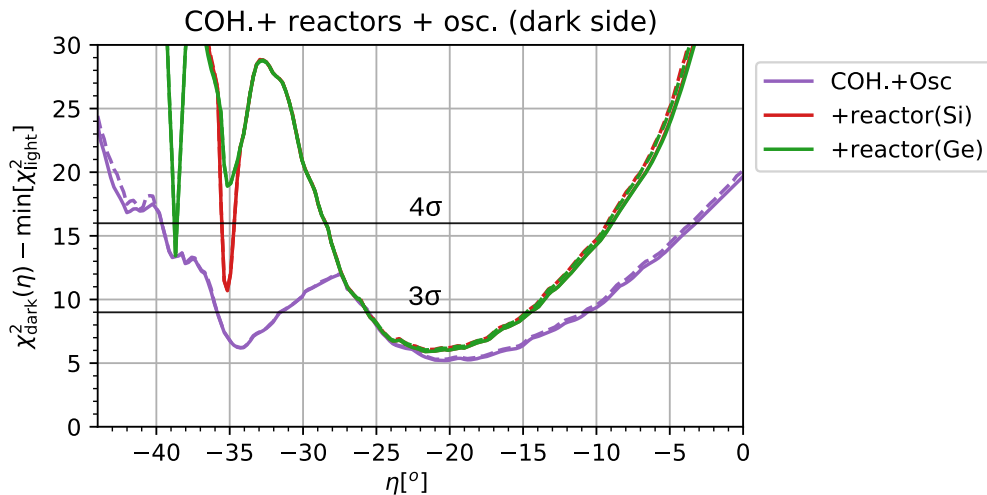


Figure 4.15: Sensitivity to exclude the LMA-dark solution by a hypothetical $\text{CE}\nu\text{NS}$ measurement at a nuclear reactor using a Si (red curves) or a Ge (green curves) target. In both cases, we assume a 5% measurement of Q_{SM} . For dashed curves, off-diagonal $\epsilon_{\alpha\beta}^{\eta}$ are fixed to zero. For solid curves, we minimize concerning them. For $\eta \gtrsim -33^{\circ}$ the Si and Ge curves overlap.

of the regions allowed by oscillations + COHERENT. The spike of the Ge experiment in fig. 4.15 has a similar origin.

In fig. 4.14, the off-diagonal NSI parameters are fixed at zero. If we had allowed them to vary freely, the region between the two vertical reactor bands would be filled for a similar reason as discussed in sec. 4.2 in the context of COHERENT. However, once the constraints from oscillation data are applied, the result is practically identical to the fixed case, c.f. fig. 4.15.

In fig. 4.16, we show some examples where the complementarity of the reactor and stopped pion source can be used to reach high significances. We combine a reactor measurement using Si with several target materials at ESS. Results for using Ge at the reactor are very similar. The ESS targets have been chosen such that by themselves; they cannot reach 3σ , c.f. sec. 4.3. We observe that the combination of a reactor with Ar (Ge) at ESS allows rejecting LMA-dark at more than 4σ (3σ). For the heavy targets, Xe and CsI, a small region remain below 3σ around $\eta \approx -20^{\circ}$.

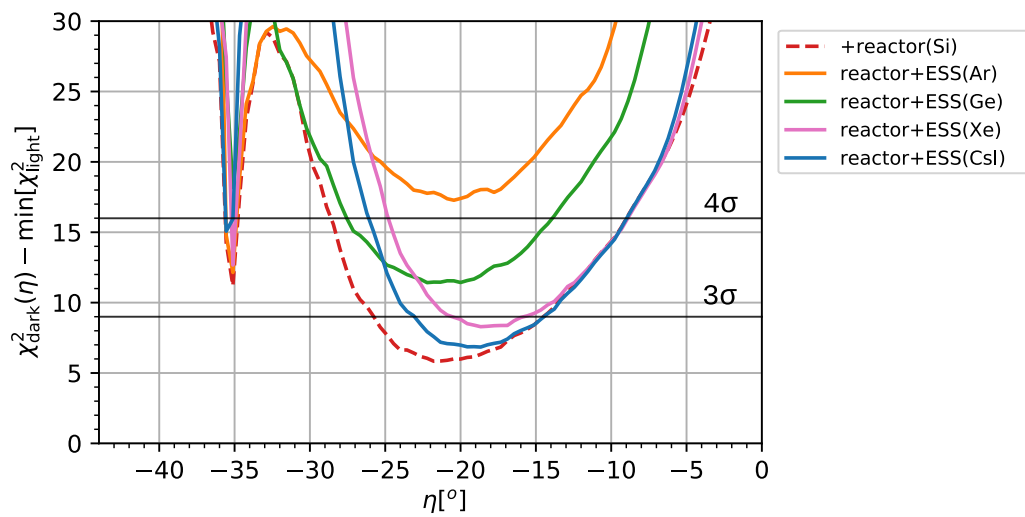


Figure 4.16: Sensitivity to exclude the LMA-dark degeneracy by a hypothetical $\text{CE}\nu\text{NS}$ measurement at a nuclear reactor combined with ESS. The red-dashed curve corresponds to Si target at a reactor. For the solid curves we combine reactor(Si) with measurements at the ESS assuming Ar, Ge, Xe, and CsI targets, see sec. 4.3 for details.

Chapter 5

Conclusions

In this thesis, we investigate the limits of neutrino data on Non-Standard Interactions (NSI) in two scenarios. In the first we study charged current NSI in reactors and in the sun, and in the second we study neutral current NSI in scattering experiments as COHERENT in the context of the Large Mixing Angle Dark (LMA-D) degeneracy.

In chapter 2, we present the formalism of neutrino oscillations based on quantum mechanics and on quantum field theory. We show that the neutrino oscillation depends on the production and detection process but for most of the real cases, the processes dependency is canceled by some approximations. We show how important it is to consider neutrino wave packets for consistency when building the theory.

In chapter 3, we study the effects of BSM physics coming from the EFT Lagrangian given in Eq. (3.3). We introduce the quantum field theory formalism to study these new interactions. In the QFT approach, the BSM physics appears in the production and detection and may cause new effects, such as CP violation. In sec. 3.2.1, we study the formula for oscillation, and we separate the analysis by scale and type of interactions. We found that some types of interaction can decouple in different scales, e.g., the $[\tilde{\epsilon}_X]_{e\tau}$ appears mostly in the atmospheric scale and $[\tilde{\epsilon}_X]_{e\mu}$ in the solar scale. However, that is not always the case. We show that when the experiment is sensitive to parameters of the atmospheric scale, it can also detect CP violation effects from the solar scale, which happened for the Daya Bay experiment. In addition, we show how to calculate the production and detection factors for each experimental setup and the implementation of experiment simulation in sec. 3.3.

We analyze medium baseline reactors as Daya Bay, Double Chooz, and RENO, where those experiments show a 2σ preference for non-zero CP violation. This preference was more substantial for the $[\tilde{\epsilon}_T]_{e\mu}$ parameter. We also studied the Kamland experiment and solar experiments, where we also found a preference for non-zero CP violation in

the $[\tilde{\epsilon}_T]_{e\mu}$ interaction case. In our global analysis, the significance for this parameter was reduced but remained at 1.7σ .

We have also shown that experiments such as JUNO have the potential to test the signals seen in this analysis.

In chapter 4, we studied how CE ν NS measurements can help to understand the LMA-D degeneracy. First, we begin presenting the degeneracy, then give an overview of the present scenario, showing the consequences of recent COHERENT measurements on Ar and CsI. Finally, we show that the combination of different targets can help resolve the degeneracy for theories where the coupling with quarks d and u can be different. In that case, the LMA-D degeneracy is excluded at 3σ .

We also studied scenarios where new measurements come in handy. For example, we follow proposals of new sources as neutrino beams (ESS) and reactors (CONNIE and CONUS). For ESS, we followed the experimental proposal and performed the analysis using several targets. We could show that at least for the lightest elements as Si, the sensitivity can reach 4σ .

For reactors, we show they can help exclude islands of the parameter space, and if combined with ESS elements as Ar or Ge, we can help exclude the LMA-D at 4σ .

Bibliography

- [1] S.-B. Kim, T. Lasserre, and Y. Wang, “Reactor neutrinos,” *Adv. High Energy Phys.*, vol. 2013, p. 453816, 2013.
- [2] H. de Kerret *et al.*, “Double Chooz θ_{13} measurement via total neutron capture detection,” *Nature Phys.*, vol. 16, no. 5, pp. 558–564, 2020.
- [3] J. M. Berryman and P. Huber, “Sterile Neutrinos and the Global Reactor Antineutrino Dataset,” *JHEP*, vol. 01, p. 167, 2021.
- [4] M. C. Gonzalez-Garcia and M. Maltoni, “Phenomenology with Massive Neutrinos,” *Phys. Rept.*, vol. 460, pp. 1–129, 2008.
- [5] S. Abe *et al.*, “Precision Measurement of Neutrino Oscillation Parameters with KamLAND,” *Phys. Rev. Lett.*, vol. 100, p. 221803, 2008.
- [6] P. Coloma, I. Esteban, M. C. Gonzalez-Garcia, and M. Maltoni, “Improved Global Fit to Non-Standard Neutrino Interactions Using Coherent Energy and Timing Data,” *JHEP*, vol. 02, p. 023, 2020. [Addendum: *JHEP* 12, 071 (2020)] (version based on 2020 data).
- [7] M. E. Chaves, D. R. Gratieri, and O. L. G. Peres, “Improvements on perturbative oscillation formulas including non-standard neutrino interactions,” *J. Phys. G*, vol. 48, no. 1, p. 015001, 2020.
- [8] D. Baxter *et al.*, “Coherent Elastic Neutrino-Nucleus Scattering at the European Spallation Source,” *JHEP*, vol. 02, p. 123, 2020.
- [9] S. Weinberg, “A model of leptons,” *Phys. Rev. Lett.*, vol. 19, pp. 1264–1266, Nov 1967.

-
- [10] F. Englert and R. Brout, “Broken Symmetry and the Mass of Gauge Vector Mesons,” *Phys. Rev. Lett.*, vol. 13, pp. 321–323, Aug. 1964.
- [11] P. W. Higgs, “Broken Symmetries and the Masses of Gauge Bosons,” *Phys. Rev. Lett.*, vol. 13, pp. 508–509, 1964.
- [12] S. L. Glashow, “Partial-symmetries of weak interactions,” *Nuclear Physics*, vol. 22, no. 4, pp. 579–588, 1961.
- [13] S. Chatrchyan *et al.*, “Observation of a New Boson at a Mass of 125 GeV with the CMS Experiment at the LHC,” *Phys. Lett. B*, vol. 716, pp. 30–61, 2012.
- [14] F. Reines and C. L. Cowan, “Detection of the free neutrino,” *Phys. Rev.*, vol. 92, pp. 830–831, Nov 1953.
- [15] S. Weinberg and O. W. Greenberg, “The quantum theory of fields, vol. 1: Foundations,” *Physics Today*, vol. 48, pp. 78–78, 1995.
- [16] P. W. Higgs, “Broken symmetries, massless particles and gauge fields,” *Phys. Lett.*, vol. 12, pp. 132–133, 1964.
- [17] P. W. Higgs, “Spontaneous Symmetry Breakdown without Massless Bosons,” *Phys. Rev.*, vol. 145, pp. 1156–1163, 1966.
- [18] G. Aad *et al.*, “Observation of a new particle in the search for the Standard Model Higgs boson with the ATLAS detector at the LHC,” *Phys. Lett. B*, vol. 716, pp. 1–29, 2012.
- [19] Y. Fukuda *et al.*, “Evidence for oscillation of atmospheric neutrinos,” *Phys. Rev. Lett.*, vol. 81, pp. 1562–1567, 1998.
- [20] B. Pontecorvo, “Mesonium and anti-mesonium,” *Sov. Phys. JETP*, vol. 6, p. 429, 1957. [*Zh. Eksp. Teor. Fiz.*33,549(1957)].
- [21] M. Gell-Mann and A. Pais, “Behavior of neutral particles under charge conjugation,” *Phys. Rev.*, vol. 97, pp. 1387–1389, Mar 1955.
- [22] A. Pais and O. Piccioni, “Note on the decay and absorption of the θ^0 ,” *Phys. Rev.*, vol. 100, pp. 1487–1489, Dec 1955.
- [23] Z. Maki, M. Nakagawa, and S. Sakata, “Remarks on the unified model of elementary particles,” *Progress of Theoretical Physics*, vol. 28, no. 5, pp. 870–880, 1962.

-
- [24] B. Pontecorvo, “Neutrino Experiments and the Problem of Conservation of Leptonic Charge,” *Sov. Phys. JETP*, vol. 26, pp. 984–988, 1968. [Zh. Eksp. Teor. Fiz.53,1717(1967)].
- [25] B. Kayser, “On the quantum mechanics of neutrino oscillation,” *Phys. Rev. D*, vol. 24, pp. 110–116, Jul 1981.
- [26] C. Giunti, C. W. Kim, and U. W. Lee, “Remarks on the weak states of neutrinos,” *Phys. Rev. D*, vol. 45, pp. 2414–2420, Apr 1992.
- [27] C. Giunti, C. W. Kim, J. Lee, and U. Lee, “Treatment of neutrino oscillations without resort to weak eigenstates,” *Physical Review D*, vol. 48, no. 9, p. 4310, 1993.
- [28] E. K. Akhmedov and J. Kopp, “Neutrino oscillations: Quantum mechanics vs. quantum field theory,” *Journal of High Energy Physics*, vol. 2010, no. 4, p. 8, 2010.
- [29] O. G. Miranda, M. A. Tortola, and J. W. F. Valle, “Are Solar Neutrino Oscillations Robust?,” *JHEP*, vol. 10, p. 008, 2006.
- [30] S. M. Bilenky, J. Hošek, and S. Petcov, “On the oscillations of neutrinos with dirac and majorana masses,” *Physics Letters B*, vol. 94, no. 4, pp. 495–498, 1980.
- [31] M. Beuthe, “Oscillations of neutrinos and mesons in quantum field theory,” *Phys. Rept.*, vol. 375, pp. 105–218, 2003.
- [32] E. Akhmedov, “Quantum mechanics aspects and subtleties of neutrino oscillations,” in *International Conference on History of the Neutrino: 1930-2018*, 1 2019.
- [33] C. Giunti, “Neutrino wave packets in quantum field theory,” *JHEP*, vol. 11, p. 017, 2002.
- [34] A. Falkowski, M. González-Alonso, and Z. Tabrizi, “Consistent QFT description of non-standard neutrino interactions,” *JHEP*, vol. 11, p. 048, 2020.
- [35] M. E. Peskin and D. V. Schroeder, “Quantum field theory,” *The Advanced Book Program, Perseus Books Reading, Massachusetts*, p. 4, 1995.
- [36] W. Grimus and P. Stockinger, “Real oscillations of virtual neutrinos,” *Phys. Rev.*, vol. D54, pp. 3414–3419, 1996.
- [37] E. K. Akhmedov and J. Kopp, “Neutrino Oscillations: Quantum Mechanics vs. Quantum Field Theory,” *JHEP*, vol. 04, p. 008, 2010. [Erratum: JHEP10,052(2013)].

-
- [38] W. Buchmuller and D. Wyler, “Effective Lagrangian Analysis of New Interactions and Flavor Conservation,” *Nucl. Phys. B*, vol. 268, pp. 621–653, 1986.
- [39] B. Grzadkowski, M. Iskrzynski, M. Misiak, and J. Rosiek, “Dimension-Six Terms in the Standard Model Lagrangian,” *JHEP*, vol. 10, p. 085, 2010.
- [40] T. D. Lee and C. N. Yang, “Question of parity conservation in weak interactions,” *Phys. Rev.*, vol. 104, pp. 254–258, Oct 1956.
- [41] A. Falkowski, M. Gonzalez-Alonso, and Z. Tabrizi, “Reactor neutrino oscillations as constraints on Effective Field Theory,” *JHEP*, vol. 05, no. 01, p. 173, 2019.
- [42] M. González-Alonso, O. Naviliat-Cuncic, and N. Severijns, “New physics searches in nuclear and neutron β decay,” *Prog. Part. Nucl. Phys.*, vol. 104, pp. 165–223, 2019.
- [43] T. Bhattacharya, V. Cirigliano, S. Cohen, R. Gupta, H.-W. Lin, and B. Yoon, “Axial, Scalar and Tensor Charges of the Nucleon from 2+1+1-flavor Lattice QCD,” *Phys. Rev. D*, vol. 94, no. 5, p. 054508, 2016.
- [44] M. González-Alonso and J. Martin Camalich, “Isospin breaking in the nucleon mass and the sensitivity of β decays to new physics,” *Phys. Rev. Lett.*, vol. 112, no. 4, p. 042501, 2014.
- [45] A. Falkowski, G. Grilli di Cortona, and Z. Tabrizi, “Future DUNE constraints on EFT,” *JHEP*, vol. 04, p. 101, 2018.
- [46] A. N. Khan and D. W. McKay, “ $\sin^2 \theta_W$ estimate and bounds on nonstandard interactions at source and detector in the solar neutrino low-energy regime,” *JHEP*, vol. 07, p. 143, 2017.
- [47] A. N. Khan, D. W. McKay, and F. Tahir, “Sensitivity of medium-baseline reactor neutrino mass-hierarchy experiments to nonstandard interactions,” *Phys. Rev. D*, vol. 88, p. 113006, 2013.
- [48] A. Y. Smirnov, “The MSW effect and solar neutrinos,” in *10th International Workshop on Neutrino Telescopes*, pp. 23–43, 5 2003.
- [49] S. Baker and R. D. Cousins, “Clarification of the use of CHI-square and likelihood functions in fits to histograms,” *Nuclear Instruments and Methods in Physics Research*, vol. 221, pp. 437–442, Apr. 1984.

-
- [50] K. P. F.R.S., “On the criterion that a given system of deviations from the probable in the case of a correlated system of variables is such that it can be reasonably supposed to have arisen from random sampling,” *The London, Edinburgh, and Dublin Philosophical Magazine and Journal of Science*, vol. 50, no. 302, pp. 157–175, 1900.
- [51] M. Maltoni and T. Schwetz, “Testing the statistical compatibility of independent data sets,” *Phys. Rev. D*, vol. 68, p. 033020, 2003.
- [52] A. Gando *et al.*, “Reactor On-Off Antineutrino Measurement with KamLAND,” *Phys. Rev. D*, vol. 88, no. 3, p. 033001, 2013.
- [53] G. Bak *et al.*, “Measurement of Reactor Antineutrino Oscillation Amplitude and Frequency at RENO,” *Phys. Rev. Lett.*, vol. 121, no. 20, p. 201801, 2018.
- [54] D. Adey *et al.*, “Measurement of the Electron Antineutrino Oscillation with 1958 Days of Operation at Daya Bay,” *Phys. Rev. Lett.*, vol. 121, no. 24, p. 241805, 2018.
- [55] M. Estienne *et al.*, “Updated Summation Model: An Improved Agreement with the Daya Bay Antineutrino Fluxes,” *Phys. Rev. Lett.*, vol. 123, no. 2, p. 022502, 2019.
- [56] P. Huber, M. Lindner, and W. Winter, “Simulation of long-baseline neutrino oscillation experiments with GLoBES (General Long Baseline Experiment Simulator),” *Comput. Phys. Commun.*, vol. 167, p. 195, 2005.
- [57] P. Huber, J. Kopp, M. Lindner, M. Rolinec, and W. Winter, “New features in the simulation of neutrino oscillation experiments with GLoBES 3.0: General Long Baseline Experiment Simulator,” *Comput. Phys. Commun.*, vol. 177, pp. 432–438, 2007.
- [58] P. Huber, “On the determination of anti-neutrino spectra from nuclear reactors,” *Phys. Rev. C*, vol. 84, p. 024617, 2011. [Erratum: *Phys.Rev.C* 85, 029901 (2012)].
- [59] T. A. Mueller *et al.*, “Improved Predictions of Reactor Antineutrino Spectra,” *Phys. Rev. C*, vol. 83, p. 054615, 2011.
- [60] F. Suekane, “KamLAND,” *Prog. Part. Nucl. Phys.*, vol. 57, pp. 106–126, 2006.
- [61] P. Vogel and J. F. Beacom, “Angular distribution of neutron inverse beta decay, $\bar{\nu}_e + p \rightarrow e^+ + n$,” *Phys. Rev. D*, vol. 60, p. 053003, 1999.
- [62] P. Huber, J. Kopp, M. Lindner, A. Merle, W. Rodejohann, M. Rolinec, T. Schwetz, and W. Winter, “Physics potential of future reactor neutrino experiments,” *Nuclear*

-
- Physics B - Proceedings Supplements*, vol. 221, p. 360, 2011. The Proceedings of the 22nd International Conference on Neutrino Physics and Astrophysics.
- [63] J. N. Bahcall and A. M. Serenelli, “How do uncertainties in the surface chemical abundances of the Sun affect the predicted solar neutrino fluxes?,” *Astrophys. J.*, vol. 626, p. 530, 2005.
- [64] J. Hosaka *et al.*, “Solar neutrino measurements in super-Kamiokande-I,” *Phys. Rev.*, vol. D73, p. 112001, 2006.
- [65] S. Fukuda *et al.*, “Determination of solar neutrino oscillation parameters using 1496 days of Super-Kamiokande I data,” *Phys. Lett.*, vol. B539, pp. 179–187, 2002.
- [66] K. Abe *et al.*, “Solar Neutrino Measurements in Super-Kamiokande-IV,” *Phys. Rev.*, vol. D94, no. 5, p. 052010, 2016.
- [67] B. Aharmim *et al.*, “Combined Analysis of all Three Phases of Solar Neutrino Data from the Sudbury Neutrino Observatory,” *Phys. Rev.*, vol. C88, p. 025501, 2013.
- [68] M. Agostini *et al.*, “Comprehensive measurement of *pp*-chain solar neutrinos,” *Nature*, vol. 562, no. 7728, pp. 505–510, 2018.
- [69] F. Kaether, W. Hampel, G. Heusser, J. Kiko, and T. Kirsten, “Reanalysis of the GALLEX solar neutrino flux and source experiments,” *Phys. Lett.*, vol. B685, pp. 47–54, 2010.
- [70] J. N. Abdurashitov *et al.*, “Measurement of the solar neutrino capture rate with gallium metal. III: Results for the 2002–2007 data-taking period,” *Phys. Rev.*, vol. C80, p. 015807, 2009.
- [71] B. T. Cleveland, T. Daily, R. Davis, Jr., J. R. Distel, K. Lande, C. K. Lee, P. S. Wildenhain, and J. Ullman, “Measurement of the solar electron neutrino flux with the Homestake chlorine detector,” *Astrophys. J.*, vol. 496, pp. 505–526, 1998.
- [72] G. L. Fogli, E. Lisi, D. Montanino, and A. Palazzo, “Three-flavor MSW solutions of the solar neutrino problem,” *Phys. Rev. D*, vol. 62, p. 013002, 2000.
- [73] F. An *et al.*, “Neutrino Physics with JUNO,” *J. Phys. G*, vol. 43, no. 3, p. 030401, 2016.

-
- [74] P. Coloma and T. Schwetz, “Generalized Mass Ordering Degeneracy in Neutrino Oscillation Experiments,” *Phys. Rev.*, vol. D94, no. 5, p. 055005, 2016. [Erratum: *Phys. Rev.*D95,no.7,079903(2017)].
- [75] M. Chaves and T. Schwetz, “Resolving the LMA-dark NSI degeneracy with coherent neutrino-nucleus scattering,” *JHEP*, vol. 05, p. 042, 2021.
- [76] J. Dorenbosch *et al.*, “Experimental Verification of the Universality of ν_e and ν_μ Coupling to the Neutral Weak Current,” *Phys. Lett. B*, vol. 180, pp. 303–307, 1986.
- [77] D. Z. Freedman, “Coherent Neutrino Nucleus Scattering as a Probe of the Weak Neutral Current,” *Phys. Rev. D*, vol. 9, pp. 1389–1392, 1974.
- [78] J. Erler and M. J. Ramsey-Musolf, “The Weak mixing angle at low energies,” *Phys. Rev. D*, vol. 72, p. 073003, 2005.
- [79] J. Barranco, O. G. Miranda, and T. I. Rashba, “Probing New Physics with Coherent Neutrino Scattering Off Nuclei,” *JHEP*, vol. 12, p. 021, 2005.
- [80] D. Akimov *et al.*, “Observation of Coherent Elastic Neutrino-Nucleus Scattering,” *Science*, vol. 357, no. 6356, pp. 1123–1126, 2017.
- [81] D. Pershey, “New CEvNS Results from the COHERENT CsI[Na] Detector,” Dec. 2020. seminar talk at Fermilab.
- [82] D. Akimov *et al.*, “First Measurement of Coherent Elastic Neutrino-Nucleus Scattering on Argon,” *Phys. Rev. Lett.*, vol. 126, no. 1, p. 012002, 2021.
- [83] P. Coloma, M. C. Gonzalez-Garcia, M. Maltoni, and T. Schwetz, “Coherent Enlightenment of the Neutrino Dark Side,” *Phys. Rev.*, vol. D96, no. 11, p. 115007, 2017.
- [84] R. Storn and K. Price, “Differential evolution - a simple and efficient heuristic for global optimization over continuous spaces,” *Journal of Global Optimization*, vol. 11, pp. 341–359, 01 1997.
- [85] P. Virtanen, R. Gommers, T. E. Oliphant, M. Haberland, T. Reddy, D. Cournapeau, E. Burovski, P. Peterson, W. Weckesser, J. Bright, S. J. van der Walt, M. Brett, J. Wilson, K. J. Millman, N. Mayorov, A. R. J. Nelson, E. Jones, R. Kern, E. Larson, C. J. Carey, Í. Polat, Y. Feng, E. W. Moore, J. VanderPlas, D. Laxalde, J. Perktold, R. Cimrman, I. Henriksen, E. A. Quintero, C. R. Harris, A. M. Archibald, A. H. Ribeiro, F. Pedregosa, P. van Mulbregt, and SciPy 1.0 Contributors, “SciPy

-
- 1.0: Fundamental Algorithms for Scientific Computing in Python,” *Nature Methods*, vol. 17, pp. 261–272, 2020.
- [86] I. Esteban, M. C. Gonzalez-Garcia, M. Maltoni, I. Martínez-Soler, and J. Salvado, “Updated Constraints on Non-Standard Interactions from Global Analysis of Oscillation Data,” *JHEP*, vol. 08, p. 180, 2018. [Addendum: *JHEP* 12, 152 (2020)] (version based on 2020 data).
- [87] P. Coloma, P. B. Denton, M. C. Gonzalez-Garcia, M. Maltoni, and T. Schwetz, “Curtauling the Dark Side in Non-Standard Neutrino Interactions,” *JHEP*, vol. 04, p. 116, 2017.
- [88] O. G. Miranda, D. K. Papoulias, O. Sanders, M. Tórtola, and J. W. F. Valle, “Future CEvNS experiments as probes of lepton unitarity and light-sterile neutrinos,” *Phys. Rev. D*, vol. 102, p. 113014, 2020.
- [89] A. Aguilar-Arevalo *et al.*, “Search for light mediators in the low-energy data of the CONNIE reactor neutrino experiment,” *JHEP*, vol. 04, p. 054, 2020.
- [90] R. Strauss, “Future uses of CEvNS,” June 2020. talk at the Neutrino20 conference.
- [91] A. Aguilar-Arevalo *et al.*, “Exploring Low-Energy Neutrino Physics with the Coherent Neutrino Nucleus Interaction Experiment,” *Phys. Rev. D*, vol. 100, no. 9, p. 092005, 2019.
- [92] H. Bonet *et al.*, “First Constraints on Elastic Neutrino Nucleus Scattering in the Fully Coherent Regime from the Conus Experiment,” 10 2020.